Development of Seismic Retrofitting Techniques for Historical Masonry Structures with Application of High Performance Materials

2011

Kshitij Charana Shrestha

Acknowledgements

The present work is carried out at the Department of Architecture and Architectural Engineering of the Kyoto University and was supervised by Prof. Koji Uetani and Assoc. Prof. Yoshikazu Araki. To Prof. Koji Uetani, I would like to thank for his care and insightful thoughts during my research. I would also like to express my sincere gratitude to Assoc. Prof. Yoshikazu Araki whose advice, suggestions, motivations and foresight were extremely valuable for the completion of my doctoral thesis.

I am grateful to the members of dissertation committee, Prof. Koji Uetani, Prof. Hitoshi Tanaka and Prof. Minehiro Nishiyama for their thorough reviews and invaluable comments.

I want to thank Dr. Takuya Nagae, senior researcher in E-Defence, for his comments and guidance throughout the research work. Discussions with Assoc. Prof. Araki and Dr. Nagae and their drive for innovative works have always been inspirational for my research work. Dr. Nagae's sense of humor always made my research work ever more refreshing.

My research group members Mr. Ippei Ibarada and Mr. Nobitoshi Yoshida were extremely important for this work to be accomplished. I gratefully acknowledge their constant help during the experimental works. I would also like to thank Assistant Prof. Noriko Takiyama for her guidance during my initial years in the doctoral work.

Thanks to all the members of Mechanics of Building Structures Laboratory for their friendliness and fun-filled moments during my stay. I would also like to thank Assistant Prof. Makoto Yamakawa for taking care of my stay in the laboratory. I would like to thank staffs of the laboratory, Ms. Matsuyama and Ms. Sachiko Kinoshita for taking care of the official works and in particular, Japanese translations.

This thesis was done with funding provided in part by Grant-in-Aid for Scientific Research (B) No. 20360253 and by Global COE Program, provided by the Japan Society for the Promotion of Science (JSPS). I gratefully acknowledge the above mentioned supports.

Finally, I thank my parents for providing me ample support and unconditional love. Very special thanks to my wife, Rosee, for her unwavering patience, understanding and love and my son Lakshya whose good company during my thesis writing was inspiring.

Summary

This study is motivated by strong needs for seismic rehabilitation of masonry structures. Several goals were set and attainment of those goals meant there were three important aspects of the work involved during this study – 1) First goal involved development of finite element model for pinning retrofitted masonry walls whose experimental works were previously reported by Takiyama et al. 2) Second goal set was to perform an extensive study on the use of polymer cement paste (PCP) as bonding agent in pinning retrofitted masonry walls in place of epoxy. 3) The third and most important part of the research presents application of superelastic materials on masonry retrofitting. The work has been presented in 6 chapters; each of them has been summarized below.

Chapter 1 gives introduction on the thesis work with arguments defining motivation driving this work with its subsequent objectives. This chapter highlights some major problems associated with present scenario of masonry retrofitting which provided impetus for this research work.

Chapter 2 presents literature survey with summary on previous works related to masonry structures. The relevant works are reviewed under six different categories – 1) Behavior of unreinforced masonry (URM) buildings, 2) Resistance mechanism of URM and reinforced masonry (RM), 3) Existing retrofitting techniques for URM, 4) Pinning retrofit as an innovative technique, 5) Numerical modeling of masonry structures and 6) Application of shape memory alloys (SMAs) in retrofitting.

Chapter 3 covers the finite element (FE) modeling of pinning retrofitted masonry walls to predict cyclic force deformation characteristics observed during experimentation. Here a simplified equivalent vertical bar model has been proposed for 2D representation of inclined inserted bars. In addition to numerical modeling,

theoretical predictions have also been made to verify the experimental observations. First section of this chapter reports FE modeling of in-plane loaded masonry walls with opening. Second section is aimed at FE modeling of out-of-plane loaded masonry walls. The developed FE model serves as an important tool for verification as well as check for design specification to the pinning retrofitted walls. To state the effectiveness and robustness of retrofitting technique and adopted numerical model, sensitivity analysis has been performed with study of masonry wall's response to changes in masonry mechanical properties. The evaluation showed almost no sensitivity to variations in masonry material constants in reinforced specimens, demonstrating the robustness of pinning retrofitting technique under cyclic loading conditions and the stability of the proposed simplified FE modeling.

Chapter 4 introduces an innovative technique of application of polymer cement pastes (PCPs) as bonding agents on pinning retrofitted masonry specimens. Epoxy resin bond that has been proposed formerly has its limitations being an organic adhesive, low fire resistance, higher cost and poor bond to wet surfaces. Use of ordinary mortar on the other hand would result in excessive workability problems that keep their usage out of context. For this purpose, chapter 3 reports an extensive study carried out to propose best possible type of PCP for masonry retrofitting among various commercially available PCPs. To limit the seepage of water from PCP to masonry and subsequently increase the workability, PCP in combination with water penetration barrier agents (impregnants) has been proposed. Best possible combination of PCP and impregnant has been met through extensive experimental works on all available combinations. Chapter 3 reports on various experimental works performed on masonry assemblages to check the applicability of use of particular PCP as bonding agents namely, workability test, pull-out test, compression test, shear test and one-point bending test. FE simulation and theoretical prediction on one-point bending test has also been reported in this chapter. The best combination of PCP and impregnant, showing strong bond with minimum strength variation at different open times and also

better resistance when tested as masonry assemblage, was attained for Styrene-butadiene rubber (SBR) PCPs with BPA (barrier penetrant) impregnant as pretreatment agent.

Chapter 5 deals with the experimental and numerical study on applicability of Cu-Al-Mn shape memory alloys (SMAs) in masonry retrofitting. Previous usage of steel reinforcing bars comes with its limitations resulting in pinching, or degradation of stiffness and strength under cyclic loading caused by inelastic elongation of reinforcing steel bars. With the recent development on cost effective and highly machinable Cu-Al-Mn SMAs, Chapter 5 reports on the proposal of masonry retrofitting that incorporates SMA bars as reinforcing elements, which with their superelastic properties can result in highly improved performance. The chapter has been divided into two sections with first one reporting on quasi-static cyclic tests and the second one on dynamic loading tests. Experimental observations have been verified using applicable numerical models. Additionally sensitivity studies have been done to check the robustness of the adopted numerical model with variation in masonry mechanical properties. From the quasi-static cyclic tests, the steel reinforced masonry (ST-RM) specimen showed pinching phenomenon and stiffness degradation in the large deformation range while the SMA-RM specimen maintained the initial stiffness without substantial degradation. Dynamic test results showed ST-RM specimens with substantial residual deformation of the wall at the end of excitation runs confirming the instability caused by residual elongation of steel reinforcing bars. This ultimately resulted in premature collapse at the exceedance of instability limit due to P-Delta effect. SMA-RM specimens exhibited stable rocking behavior without significant residual rotations even for base excitation exceeding 1.0*g*. The primary reason for maintaining this stable rocking response was attributed by the superelastic property of SMA reinforcing bars, which ensured that there was no residual strain during and after the loading history. The results effectively demonstrated the applicability and superiority of the present Cu-Al-Mn bars to retrofitting URM walls as a partial

replacement of steel bars.

Chapter 6 briefly summarizes the works reported in this thesis, highlighting the main findings and finally proposes recommendations for further studies.

List of Publications

Refereed Journal Papers (Full paper reviewed)

[1] SHRESTHA K. C., ARAKI Y., NAGAE T., OMORI T., SUTOU Y., KAINUMA R., and ISHIDA K. Applicability of Cu-Al-Mn shape memory alloy rods to retrofitting of historical masonry constructions, *Earthquakes and Structures, An International Journal*, In press, 2011.

[2] SHRESTHA K. C., PAREEK S., and ARAKI Y. Use of polymer-cement pastes as bonding agents for pinning retrofitting of masonry construction, *Proceedings of JCI*, 33(1):1661-1666, 2011.

[3] SHRESTHA K.C., NAGAE T., and ARAKI Y. Finite element study on pinning retrofitting technique of masonry walls with opening subjected to in-plane shear load, *Proceedings of 7th International Conference Analytical Models and New Concepts in Concrete and Masonry Structures*, Krakow, 2011.

[4] SHRESTHA K. C., NAGAE T., and ARAKI Y. Finite element modeling of out-of-plane response of masonry walls retrofitted by inserting inclined stainless steel bars, *Journal of Disaster Research*, 6(1):36-43, 2011.

International Conference Proceedings (Abstract reviewed)

[5] SHRESTHA K. C., NAGAE T., and ARAKI Y. Finite element modeling of out-of-plane behavior of masonry walls retrofitted by inserting steel pins, *Proceedings of the 12th Japan-Korea-Taiwan Joint Seminar on Earthquake Engineering for Building Structures*, pp. 43-51, Kaohsiung, Taiwan, November, 2010.

[6] SHRESTHA K. C., IBARADA I., NAGAE T., OMORI T., SUTOU Y., and ARAKI Y. Shaking table tests on half-scaled masonry walls retrofitted by Cu-Al-Mn SMA rods subjected to out-of-plane flexure, *Proceedings of the 5th World Conference on Structural Control and Monitoring*, Paper No. 243, Tokyo, Japan, July, 2010.

Domestic Conference Proceedings

[7] SHRESTHA K. C., PAREEK S., and ARAKI Y. Bending tests on pinning-retrofitted masonry beams with use of polymer cement pastes as binding agents, *Proceedings of Architectural Institute of Japan*, 2011 (Submitted for publication).

[8] SHRESTHA K. C., NAGAE T., ARAKI Y., TAKIYAMA N., and IBARADA I. Numerical modeling of in-plane shear behavior of un-reinforced masonry walls under monotonic loading (Part 2), *Proceedings of Architectural Institute of Japan*, C-2, pp. 893-894, 2010.

[9] SHRESTHA K. C., NAGAE T., ARAKI Y., TAKIYAMA N., and IBARADA I. Numerical modeling of in-plane shear behavior of un-reinforced masonry walls under monotonic loading, *Proceedings of Architectural Institute of Japan*, C-2, pp. 969-970, 2009.

[10] TAKIYAMA N., YOSHIDA N., NAGAE T., MAEDA H., SHRESTHA K. C., IBARADA I., and ARAKI Y. In-plane shear flexural characteristics of masonry walls reinforced by inserting stainless pins under cyclic loading: Part II, *Proceedings of Architectural Institute of Japan*, C-2, pp. 965-966, 2009.

[11] YOSHIDA N., NAGAE T., MAEDA H., FUKUMOTO S., TAKIYAMA N., SHRESTHA K. C., IBARADA I., and ARAKI Y. Cyclic in-plane shear-flexural experiments of masonry walls with opening reinforced by inserting stainless pins: Part I, *Proceedings of Architectural Institute of Japan*, C-2, pp. 963-964, 2009.

[12] IBARADA I., YOSHIDA N., NAGAE T., MAEDA H., FUKUMOTO S., TAKIYAMA N., SHRESTHA K. C., and ARAKI Y. Cyclic in-plane shear-flexural experiments of masonry walls with opening reinforced by inserting stainless pins: Part II, *Proceedings of Architectural Institute of Japan*, C-2, pp. 967-968, 2009.

Table of Contents

Table of Contents (Continued)

Table of Contents (Continued)

Table of Contents (Continued)

Table of Contents (Continued)

List of Tables

List of Figures

List of Figures (Continued)

List of Figures (Continued)

List of Figures (Continued)

List of Figures (Continued)

List of Figures (Continued)

List of Figures (Continued)

List of Figures (Continued)

List of Figures (Continued)

List of Figures (Continued)

List of Figures (Continued)

1

INTRODUCTION

1.1 GENERAL

The historical remains of Egypt and Greece prove the fact that masonry is one of the oldest construction materials employed by mankind. The very first masonry was a crude stack of selected natural stones often with earthen mortar packed between them. This type of masonry, though was poor in tension, was durable and could resist large compressive forces. Unreinforced masonry (URM) constructions, because of their constructability and substantial durability, became widespread all over the world. But historical masonry constructions show considerable states of degradation due to action of earthquakes and with the advent of time, undergo constant structural decay and damage [1]. Vulnerability of historical masonry constructions under earthquake excitations has been seen in the very recent Italy [2] and New Zealand [3] earthquakes. Thereby, there is strong need for improving the performance of historical masonry structures.

1.2 MOTIVATION FOR THE STUDY AND ITS OBJECTIVES

The real motivation for the study is based on present scenario of URM constructions as highlighted by the above mentioned fact. Hence, one important aspect of the study is to strengthen and preserve historical URM constructions. The other motivation is highlighted by the problems associated with the existing retrofitting techniques that have been practiced namely, attachment of reinforcing members, surface treatments, grouting, post-tensioning and reinforced core technique, most of which usually either change the appearance of URM constructions significantly or would require removal of roof and changes to existing foundation. These shortcomings make these retrofitting techniques problematic especially in historical masonry constructions. The second important aspect of the study is aimed at analytical and theoretical verifications [4,5] to the experimental works [6] done for the proposed pinning retrofit technique which can preserve the original appearance of historical URM constructions and more importantly enhances strength capability and ductility of original structure.

Experimental works and proposals for the pinning retrofitting of masonry walls [6] put forth epoxy resin as bonding agents between masonry and reinforcing bars. However presence of epoxy resin, which is an organic material and is relatively expensive, has low fire resistance and is less durable, has limited extensive practice of pinning retrofit technique. Next goal of this thesis is proposal of polymer cement paste as bonding agent [7,8] for pinning retrofit which is inorganic, less expensive, has better fire resistance and better durability.

Next important motivation for the study comes with the use of smart materials shape memory alloys (SMAs) in masonry retrofitting. Previous usage of steel reinforcing bars comes with its limitations resulting in pinching, or degradation of stiffness and strength under cyclic loading caused by inelastic elongation of reinforcing steel bars. With the recent development on cost effective and highly machinable Cu-Al-Mn

SMAs [9], this study [10,11] proposes masonry retrofitting that incorporates SMA bars as reinforcing elements which with their superelastic properties can result in highly improved performance.

1.3 ORGANIZATION OF THESIS

A review of the literatures in the areas related to this study is summarized in Chapter 2. The review, based on its subsequent objective, has been divided into six different sections -- behavior of URM buildings, resistance mechanism of unreinforced and reinforced masonry, existing retrofitting technique for URM, pinning retrofit as an innovative technique, numerical modeling of masonry structures and finally application of shape memory alloys in retrofitting.

Chapter 3 covers the finite element (FE) modeling of pinning retrofitted masonry walls. First section of this chapter reports FE modeling of in-plane loaded masonry walls with opening. Here a simplified equivalent vertical bar model has been proposed for 2D representation of inclined inserted bars. In addition to numerical modeling, theoretical predictions have also been made to verify the experimental observations. Second section of this chapter is aimed at FE modeling of out-of-plane loaded masonry walls. To state the effectiveness and robustness of retrofitting technique and adopted numerical model, sensitivity analysis has been performed with study of masonry wall's response to changes in masonry mechanical properties.

Chapter 4 introduces an innovative technique of application of polymer cement pastes (PCPs) as bonding agents on pinning retrofitted masonry specimens. Comparison on various types of PCPs in combination with water penetration barrier agents (impregnants) has been shown. This chapter first reports on various experimental works performed on masonry assemblages to check the applicability of use of particular PCP as bonding agents namely, workability test, pull-out test,

compression test, shear test and finally one-point bending test. FE simulation and theoretical prediction on one-point bending test has also been reported in this chapter.

Chapter 5 deals with the experimental and numerical study on applicability of CuAlMn shape memory alloys (SMAs) in masonry retrofitting. Reinforced-core technique is adopted for retrofitting purpose. The chapter has been divided into two sections with first one reporting on quasi-static cyclic tests and the second one on dynamic loading. Experimental observations have been verified using applicable numerical models. Additionally sensitivity studies have been done to check the robustness of the adopted numerical model with variation in masonry mechanical properties.

Chapter 6 briefly summarizes the works reported in this thesis, highlighting the main findings and finally proposes recommendations for further studies.

REFERENCES

[1] TOULIATOS P. G. Seismic behaviour of traditionally-built constructions. Repair and Strengthening. In Petrini V. and Save M., editors, *Protection of the architectural heritage against earthquakes*, pages 57-69, New York, 1996. Springer.

[2] MODENA C., CASARIN F., PORTO F. da and MUNARI M. L'Aquila 6th April 2009 Earthquake: Emergency and post-emergency activities on cultural heritage buildings. In Garevski M. and Ansal A., editors, *Earthquake Engineering in Europe*, pages 495-521, New York, 2010. Springer.

[3] BIGGS D. T., ASCE Distinguished Member an Eyewitness to New Zealand Earthquake - Engineer Details Earthquake Experience and Aftermath, http://www.asce.org/PPLContent.aspx?id=12884904967.

[4] SHRESTHA K. C., NAGAE T. and ARAKI Y. Finite element modeling of cyclic out-of-plane response of masonry walls retrofitted by inserting inclined stainless

steel bars. *Journal of Disaster Research*, 6(1):36-43, 2011.

[5] SHRESTHA K.C., NAGAE T. and ARAKI Y., Finite element study on pinning retrofitting technique of masonry walls with opening subjected to in-plane shear load. *Proceedings of 7th International Conference Analytical Models and New Concepts in Concrete and Masonry Structures*, Krakow, 2011.

[6] TAKIYAMA N. Experimental study on seismic retrofitting of historical masonry structures with emphasis on preservation of original appearance. *PhD Thesis*, Kyoto University, 2009. (In Japanese)

[7] SHRESTHA K. C., PAREEK S., and ARAKI Y., Use of polymer-cement pastes as bonding agents for pinning retrofitting of masonry construction*, Proceedings of JCI*, Vol. 33, 2011.

[8] SHRESTHA K. C., PAREEK S., ARAKI Y., Bending tests on pinning-retrofitted masonry beams with use of polymer cement pastes as binding agents, *Proceedings of Architectural Institute of Japan*, 2011.

[9] ARAKI Y., ENDO T., OMORI T., SUTOU Y., KOETAKA Y., KAINUMA R. and ISHIDA K. Potential of superelastic Cu-Al-Mn alloy bars for seismic applications. *Earthquake Engineering and Structural Dynamics*, 40(1): 107-115, 2011.

[10] SHRESTHA K. C., ARAKI Y., NAGAE T., OMORI T., SUTOU Y., KAINUMA R. and ISHIDA K. Applicability of Cu-Al-Mn shape memory alloy rods to retrofitting of historical masonry constructions, *Earthquakes and Structures, An International Journal*, 2011. (In press)

[11] SHRESTHA K. C., IBARADA I., NAGAE T., OMORI T., SUTOU Y. and ARAKI Y. Shaking table tests on half-scaled masonry walls retrofitted by Cu-Al-Mn SMA rods subjected to out-of-plane flexure, *Proceedings of the 5th World Conference on Structural Control and Monitoring*, Paper No. 243, Tokyo, 2010.

2

LITERATURE SURVEY

2.1 GENERAL

There has been extensive research conducted on reinforced and prestressed concrete structures, however much less has been reported for masonry structures. The present thesis relates the latter with significance on the upgrading of masonry structures to improve the in-plane and out-of-plane wall strength to resist the lateral force resulting from possible earthquake excitations. This chapter basically summarizes the previous works related to the objectives of this study. The relevant works are reviewed under the following categories:

1. Behavior of URM buildings
2. Resistance mechanism of unreinforced and reinforced masonry
3. Existing retrofitting techniques for URM
4. Pinning retrofit as an innovative technique
5. Numerical modeling of masonry structures

6. Application of shape memory alloys (SMAs) in retrofitting

2.2 BEHAVIOR OF URM BUILDINGS

URM buildings typically consist of foundations, URM walls and piers oriented in orthogonal directions and timber floors, acting as diaphragms, connected to walls by wall diaphragm ties. URM walls are typically stiff structural elements and can be categorized into in-plane and out-of-plane walls depending on the direction of earthquake motion relative to the plane of the walls. Walls oriented parallel to the motion of earthquakes are called in-plane walls, and walls perpendicular to in-plane walls are defined as out-of-plane walls. URM buildings are characterized by a limited number of storeys typically up to three or four. As a generalization they have regular plan shapes and the external walls form part of the horizontal force resisting system.

URM has been shown to perform poorly in earthquakes. There are a number of common details and aspects of URM construction which have been identified as deficient. The common mechanisms of failure are mainly subdivided in to two:

***In-plane*:** Masonry wall subjected to in-plane horizontal loads may fail in one of three ways: by sliding horizontally, in flexure, or in shear [1]. The mode of failure is influenced by many factors such as wall aspect ratios, axial compression stress levels, wall boundary conditions and the strength properties of the materials used in wall construction. These types of failure are shown diagrammatically in Figure 2.1.

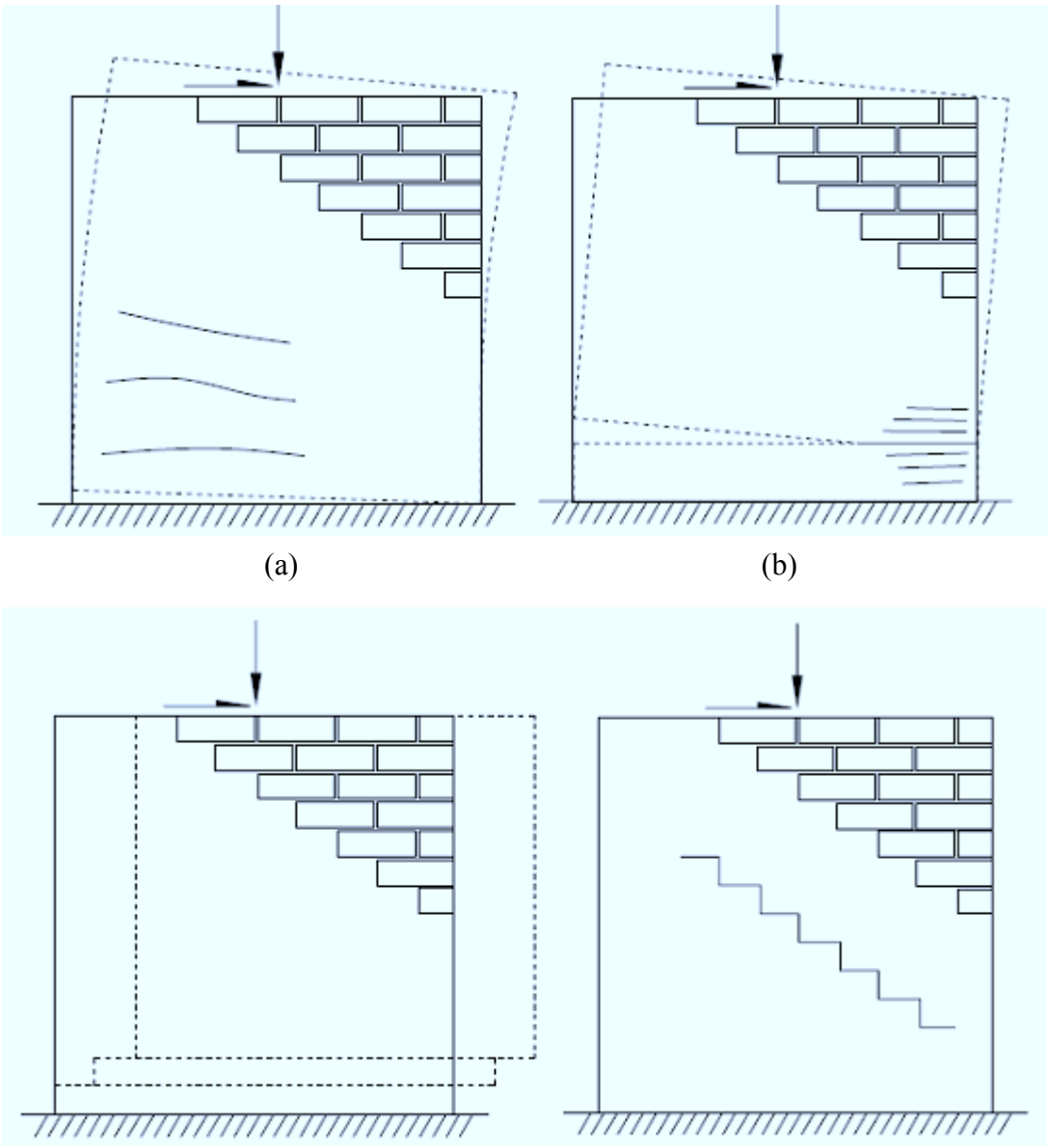

(a) (b)

(c) (d)

Figure 2.1: Failure patterns for in-plane loaded masonry walls: (a) Flexure, (b) Rocking, (c) Sliding, (d) Diagonal shear.

***Out-of-plane*:** These mechanisms occur with out-of-plane kinematics of one or more wall of the masonry building causing the loss of own original configuration at the expense of large seismic excitations. The arising of out-of-plane failure mechanism mainly result due to the ill connection between the walls of the façade and the orthogonal ones.

Based on the failure mechanism of masonry walls, common failure modes of URM buildings can be summarized as follows [2]:

- Story shear mechanisms for upper storeys
- Story shear mechanisms for lower storeys
- Whole wall overturning
- Partial wall overturning
- Gable wall overturning
- Vertical instability of wall

***Story shear mechanisms for upper storeys*:** This failure mechanism as shown in Fig. 2.2 is normally resulted due to variations in the resistance system at the upper floors i.e. variations in the wall thickness and/or presence of poorer quality masonry. This failure mechanism is also caused by presence of heavy roofs.

***Story shear mechanisms for lower storeys*:** This failure mechanism is shown in Fig. 2.3 with diagonal shear cracks of in-plane walls at the lower storeys. This is mainly caused by small resistance area in one or two directions i.e. for high percentage of openings or small thickness of the walls at lower storey.

***Whole wall overturning*:** This is mainly caused by lack of connections between orthogonal walls and/or of ties or ring beams as shown in Fig. 2.4. This is also resulted by large distance between walls and thrusting roof at the top with lack of connection between wall and roof.

***Partial wall overturning*:** This failure mechanism as shown in Fig. 2.5 is caused by following reasons- large distance between walls, thrusting roof and lack of connection between wall and roof and high percentage of opening creating potential regions for cracks.

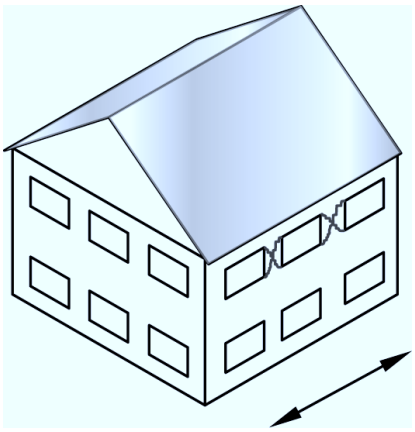

Fig. 2.2 Storey shear mechanism (Upper storey).

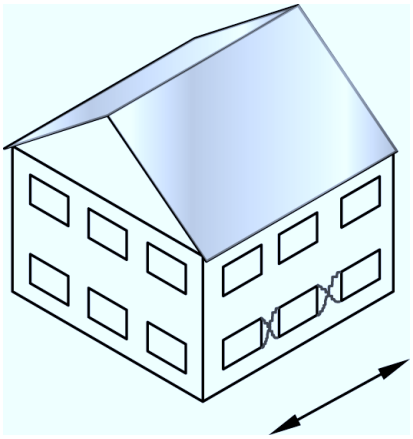

Fig. 2.3 Storey shear mechanism (Lower storey).

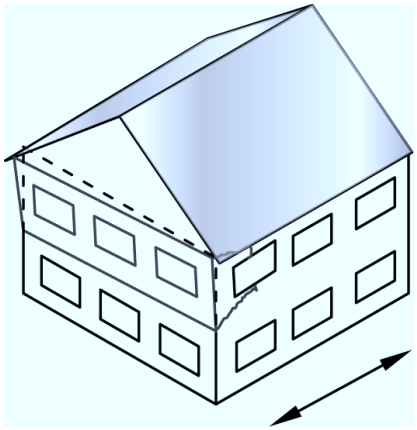

Fig. 2.4 Whole wall overturning.

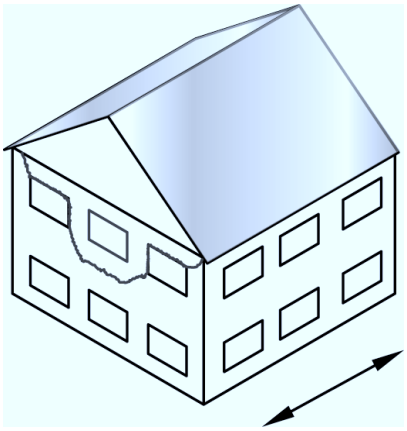

Fig. 2.5 Partial wall overturning.

***Gable wall overturning*:** Overturning of gable wall as shown in Fig. 2.6 is mainly caused by presence of heavy roofs with pushing transversal elements on to gable walls. Another reason could be good connections between orthogonal walls, but lack of connections and/or of ties or ring beams in the top.

***Vertical instability of wall*:** This mechanism is mainly caused by presence of ring beams in breach on masonry to double wall as shown in Fig. 2.7. Also contributing factors could be poor quality of masonry and presence of intermediate floors with poor embedment to the walls.

Zuccaro and Rauci [2] reported that out-of-plane mechanisms (complete and partial

wall overturnings, gable wall overturnings, vertical instability) are much more frequently correlated to the high level of global damage of the structure than the in-plane collapse mechanisms with storey shears. Hence better vulnerability assessments proper cares are needed for out-of-plane strengthening of masonry walls.

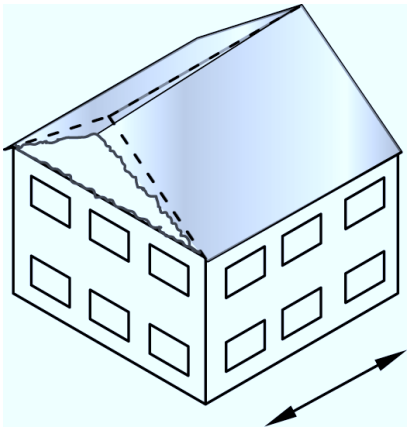

Fig. 2.6 Gable wall overturning.

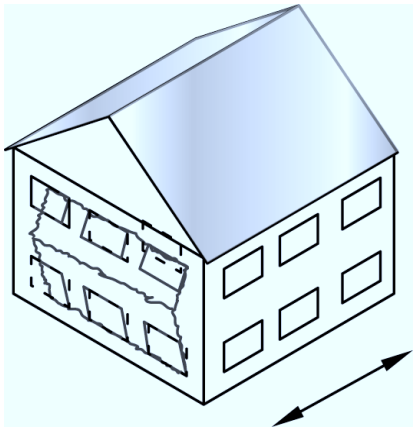

Fig. 2.7 Vertical instability of wall.

2.3 RESISTANCE MECHANISM OF UNREINFORCED AND REINFORCED MASONRY

As described in the preceding section masonry structure are typically “box like” with shear wall panels potentially subjected to simultaneous gravity and horizontal loads, resulting in overturning moments during seismic excitation. The resistance mechanism to the applied loads is predominantly contributed by the in-plane walls. Masonry walls have comparatively smaller out-of-plane resistance hence walls in out-of-plane direction play less significant role in resisting the seismic excitation. The following subsections briefly describe the two forms of resistance mechanism (flexural and shear) for both unreinforced and reinforced masonry walls.

2.3.1 Flexural resistance

2.3.1.1 Unreinforced masonry

As reported by Tomazevic [1] structural wall damage attributed to predominant

flexural behavior is rarely observed, where more of a shear type behavior is commonly seen when masonry buildings are subjected to earthquake loads. The flexural strength of a vertically reinforced masonry wall is usually computed using simple flexural theory, with assumptions plane sections remain plain after bending. The nominal flexural strength of a masonry wall can be approximated by assuming a rectangular compression stress block as shown in Fig. 2.8 below with a stress level of f_k'/γ_m, and with a depth of *a,* where γ_m is the partial safety factor for masonry. The maximum strain, ε_m allowed can be assumed to be 0.0035 at the extreme compression fiber of an unconfined section. Based on above assumption, equilibrium of sectional forces in the most stressed section of a plain masonry wall at ultimate state can be as shown in Fig. 2.9. From Fig. 2.9, the flexural capacity of unreinforced masonry wall can be evaluated as shown below,

$$F_w = N = \sigma_0 lt = f\, at \tag{2.1}$$

$$\text{which yields,} \quad a = \frac{\sigma_0}{f} l$$

where F_w is the resultant of compressive forces in the wall, l is the length of the wall and t it's thickness.

The eccentricity of vertical load N at ultimate state is given by,

$$e_u = \frac{l}{2}\left(1 - \frac{\sigma_0}{f}\right) \tag{2.2}$$

The corresponding bending moment resistance giving the flexural wall capacity of the wall's section is given by,

$$M_{Ru}^{URM} = N\, e_u = \frac{\sigma_0 t l^2}{2}\left(1 - \frac{\sigma_0}{f}\right) \tag{2.3}$$

The design flexural capacity is given by,

$$M_{Rd}^{URM} = \frac{\sigma_d t l^2}{2}\left(1 - \frac{\gamma_m \sigma_d}{f_k}\right) \tag{2.4}$$

where σ_d is the design value of the compressive stress.

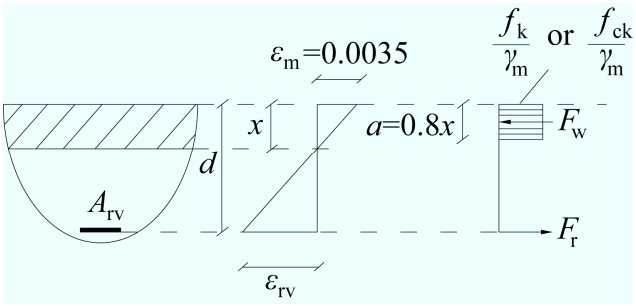

Figure 2.8: Simplified equivalent rectangular stress block [1].

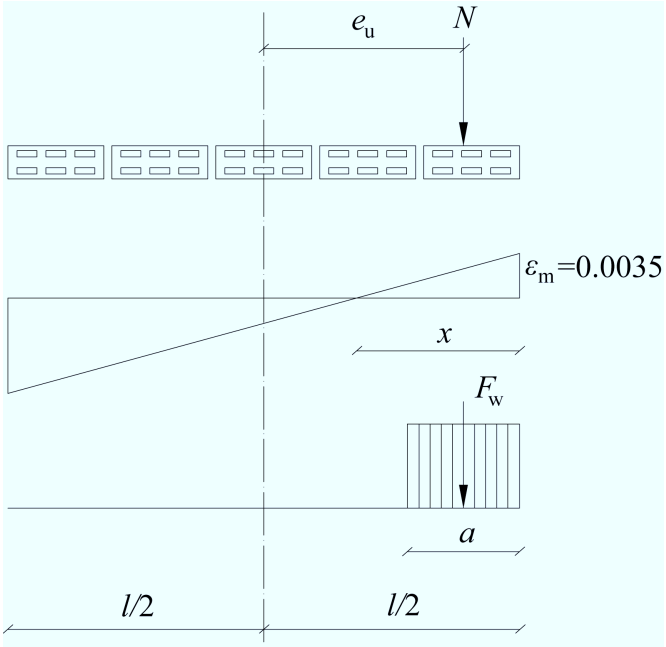

Figure 2.9: Equilibrium of sectional forces at flexural failure of URM [1].

2.3.1.2 Reinforced masonry

In case of reinforced masonry, with symmetrical vertical reinforcement at the ends, sectional forces developed in masonry and reinforcing steel at ultimate state are shown in Fig. 2.10. Using Fig. 2.10 and similar computation as followed for URM case, the equation for the flexural capacity of reinforced masonry wall can be written as,

$$M_{Ru}^{RM} = N e_u = \frac{\sigma_0 t l^2}{2}\left(1-\frac{\sigma_0}{f}\right)+(l-2l')A_{rv}f_y \qquad (2.5)$$

where Arv is the area of vertical reinforcement symmetrically placed at both ends, fy is reinforcement bar's yield stress, l' is the distance of reinforcement from the vertical

edge of the wall.

The design flexural capacity for the reinforced masonry is given by,

$$M_{\mathrm{Rd}}^{\mathrm{RM}} = \frac{\sigma_{\mathrm{d}} t l^2}{2}\left(1 - \frac{\gamma_{\mathrm{m}}\sigma_{\mathrm{d}}}{f_{\mathrm{k}}}\right) + (l - 2l')A_{\mathrm{rv}}\frac{f_{\mathrm{y}}}{\gamma_{\mathrm{s}}} \tag{2.6}$$

where γ_s is the partial safety factor for steel reinforcement bar.

2.3.2 Shear resistance

2.3.2.1 Unreinforced masonry

Unreinforced masonry walls behave as a brittle structural elements with limited energy dissipation when undergoing shear failure, especially when subjected to high compressive stresses [1,3]. A single diagonal crack causes severe deterioration in strength and subsequently results in brittle collapse. For low axial compression stresses, shear strength can be expressed by Mohr-Coulomb shear friction theory as shown below,

$$\tau_{\mathrm{w}} = \tau_0 + \mu_{\mathrm{f}}\, f_{\mathrm{n}} \tag{2.7}$$

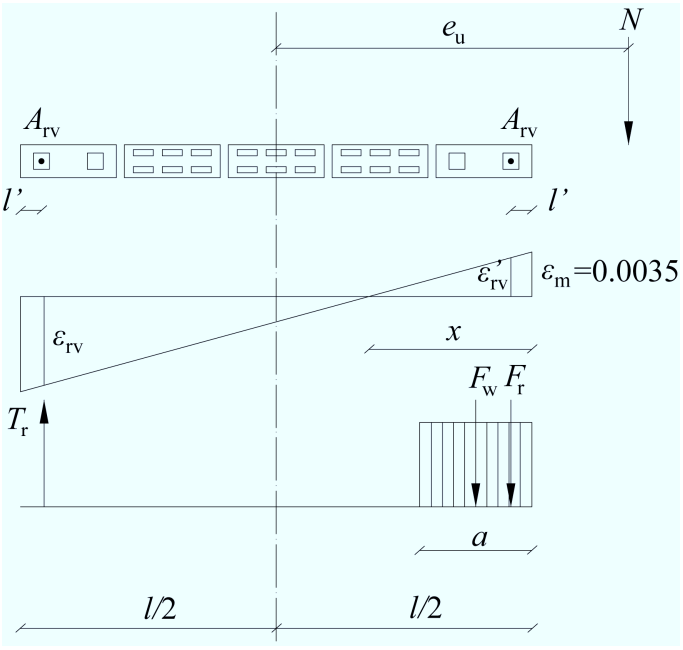

Figure 2.10: Equilibrium of sectional forces at flexural failure of reinforced masonry [1].

where τ_w and f_n are the average shear and normal (compressive) stresses, τ_0 is the shear stress under zero compressive stress and μ_f is the coefficient of internal friction.

2.3.2.2 Reinforced masonry

Reinforced masonry walls are provided with steel reinforcement, both horizontally and vertically, with an aim to improve ductility and lateral resistance. The horizontal reinforcement prevents separation of the wall's cracked portions at shear failure, thereby improving the shear resistance and energy dissipation capacity of the wall. Basic failure mechanisms of reinforcement action at shear failure for vertically and horizontally reinforced masonry walls are shown in Fig. 2.11. Tomazevic [1] reported that shear resistance for the reinforced masonry walls is contributed by several mechanisms -- tension of horizontal reinforcement, dowel action of vertical reinforcement and axial compressive force that enhances aggregate interlocking between the parts of the walls separated by diagonal cracks.

As mentioned above, different mechanisms contribute to shear resistance of reinforced masonry wall, which makes predicting the effective theoretical model complex. In practical calculation, the nominal shear strength, V_n, of the reinforced masonry walls is evaluated as the sum of contributions from masonry, reinforcement and applied axial compression load as shown below,

$$V_n = V_m + V_s + V_p \tag{2.8}$$

where V_m is contribution of masonry to shear strength, V_s of shear reinforcement and V_p of applied axial compressive load.

In the case where masonry walls are provided with vertical reinforcement, part of the shear resistance capacity can be attributed to dowel action of the vertical reinforcement. Shear forces can be transferred along a well-defined plane (e.g. a diagonal crack) by the shear, flexural and kinking actions which are activated locally in reinforcing bars due to their relative displacement along a crack as shown in Fig. 2.12.

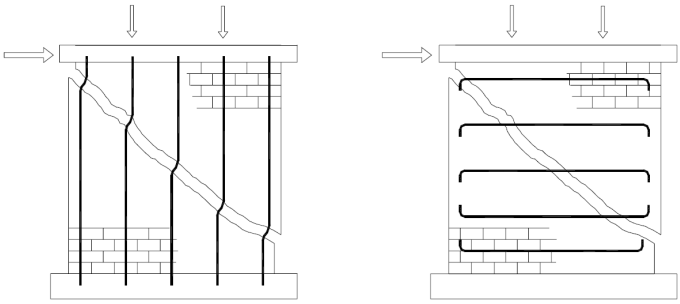

(a) (b)

Figure 2.11: Reinforcement mechanism for reinforced masonry wall: (a) Vertical reinforcement, (b) Horizontal reinforcement.

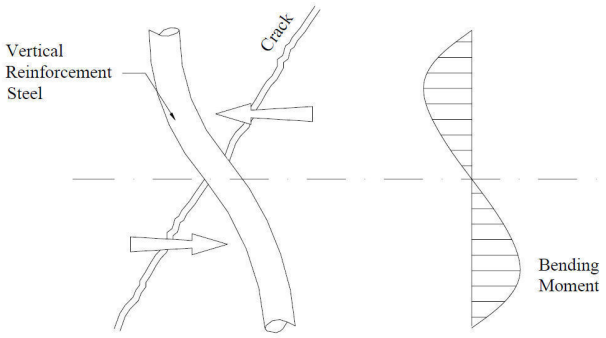

Figure 2.12: Dowel action for vertical reinforcing bar.

2.4 EXISTING RETROFITTING TECHNIQUES FOR URM

Recognizing the shortcomings of URM walls, there has been a surge in interest in developing techniques for improving their seismic. Main techniques devised in the studies can be classified in the following types: (1) attachment of reinforcing members, (2) surface treatment, (3) grout injection, (4) post-tensioning, and (5) reinforced core technique.

Attachment of reinforcing members

Here vertical, horizontal as well as diagonal bracing in the form of steel plates or tubes are used as external reinforcements for existing URM walls. Rai and Goel [4]

proposed a strengthening scheme using steel vertical elements and energy dissipation devices to enhance the seismic performance of rocking piers. Taghdi et al. [5] proposed vertical and diagonal bracing system as shown in Fig. 2.13(a) which increased the resistance of retrofitting wall by a factor of 4.5.

Additionally, a slightly different technique, where new tie columns are attached to the existing URM buildings, is also practiced as shown in Fig. 2.13(b). Here tie columns are used to work as confined masonry structures which confine the walls at all corner and wall intersection as well as the vertical borders of doors and window openings [6-10]. This confinement prevents disintegration and improves ductility and energy dissipation of URM buildings. For very squat masonry walls [6] with geometrical aspect ratio of 0.33, the confinement increased the cracking load by a factor of 1.27 and ultimate load by 1.2. Tomazevic and Klemenc [7] reported for walls with higher aspect ratio, the confinement increased the lateral resistance by a factor of 1.5. Both the above mentioned studies confirmed that the confinement improved the lateral deformations and energy dissipation by more than 50%.

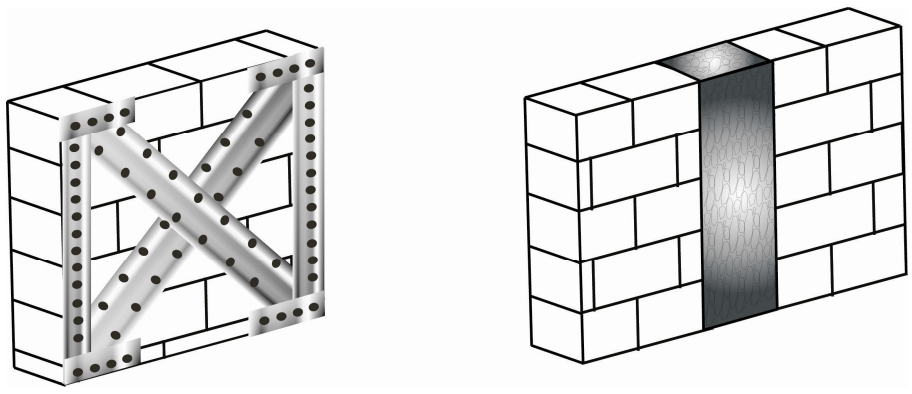

(a) (b)

Figure 2.13: Attachment of reinforcing members: (a) Vertical, horizontal and diagonal steel bracing system, (b) Attachment of tie columns.

Surface treatment

Surface treatment is a widely practiced retrofitting technique for URM walls. Representative examples of surface treatment involve adhesion of fiber reinforced plastic (FRP) overlays [11-15] as shown in Fig. 2.14(c) or ferrocement of closely spaced multiple layers of hardware mesh of fine rods embedded in a high strength cement mortar layer or spraying concrete layers over a mesh of steel reinforcing bars (shotcrete) [15,16] as shown in Fig. 2.14(d).

Mosallam [14] reported effectiveness of both the E-Glass/epoxy and carbon/epoxy FRP composite strengthening systems in upgrading the out-of-plane flexural structural performance of unreinforced brick walls. The strength gains for the composite systems in terms of ultimate capacity were increased by factor of 8-12 and ultimate mid-height deflections were increased by factor 3.2-3.6 [14].

Abrams et al. [15] reported tests on shotcrete masonry piers rehabilitated with 102 mm of reinforced concrete with medium vertical compressive stress (0.29 MPa). The ultimate load for the retrofitted specimen increased by a factor of 3 as compared to corresponding URM pier. High energy dissipation was observed due to successive elongation and yielding of reinforcement in tension. Although these techniques give higher seismic resistance to URM walls, they may change the appearance of URM constructions significantly and may cease their aesthetic value. This is problematic especially when retrofitting historical masonry constructions.

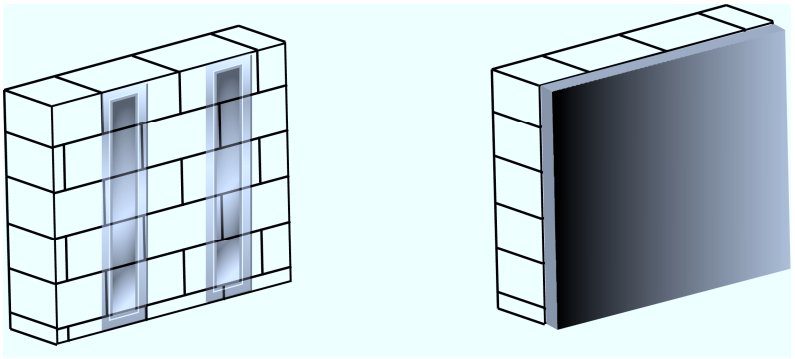

(a) (b)

Figure 2.14: Surface treatment: (a) Surface overlays, (b) Shotcrete.

Grout Injection

Grout injection [17] involves injecting grout into empty collar joints, voids and cracks present in the masonry. This strengthening technique does not alter the aesthetic and architectural features of existing buildings. For injection, epoxy resin is used for relatively small cracks (less than 2 mm wide) and cement-based grout is considered more appropriate for filling of larger cracks, voids, and empty collar joints in multi-wythe masonry walls. This retrofitting technique is effective in improving strength characteristics with restoring up to about 0.8 of unretrofitted masonry compressive strength [18], 0.8-1.1 of in-plane stiffness and 0.8-1.4 of in-plane lateral resistance [19]. Nevertheless, the increase of strength obtained by injecting grout into voids of URM walls is uncertain, and no real increase in ductility can be obtained.

Post-tensioning

Post-tensioning [16,20-23] technique on URMs can be used either vertically, to increase the vertical load on elements to counteract the tensile stresses resulting from lateral loads, or horizontally to provide confinement and reinforcing for shear behavior. This technique usually involves tendons in the form of alloy steel thread bars placed inside steel tube (duct) either within holes drilled along the mid-plane of the wall or along groves symmetrically cut on both surfaces of the wall. Holes are either cement grouted or no grout is injected between the duct and the tendons.

Post-tensioning enhances cracking loads, improves cracking behavior, and results in increased flexural resistance of masonry walls [20]. Both grouted as well as non-grouted specimens have similar lateral resistance, but the non-grouted post-tension tendons showed low energy dissipation due to lack of yielding of reinforcement.

Questions remain concerning the effect of creep and loss of prestress on this retrofit solution, particularly in older structures with relatively thick joints and low strength or

no cement mortars. Additionally, anchorage of post-tensioning is more complicated than in RC as masonry has a relatively low compressive strength. For this purpose, post-tensioning is anchored in the existing RC elements or in a new precise RC special beam or specially stiffened steel plates.

Reinforced core technique

The reinforced core technique also termed as center core technique [15,24-26] as shown in Fig. 2.15 involves preparation of a reinforced, grouted core in the center of an existing URM wall. For this purpose, a continuous vertical hole is drilled from the top of the wall up to its basement wall. The diameter of the center core may vary from 50-125 mm depending on its purpose. Core-drilling process with the present technology can drill precisely though the entire height of two or three story masonry wall. Here the drilling is a dry process with all the debris removed using vacuum and filter system to keep the dust to minimum. Once the reinforcement bars are placed in the center of the hole, a filler material is pumped from the top of the wall to the bottom. The filler material used for binding purpose may involve epoxy or cement or polyester.

The reinforced core technique largely enhances up to double the resistance of URM walls shown both in static tests [15] as well as dynamic tests [26]. This technique is often suitable for retrofitting historical masonry constructions because the technique does not change the appearance of URM walls and enhances both strength and ductility. Additionally the function of the building will not be impaired since the drilling and reinforcing operation can be done externally from the roof. However the technique requires removal of roof and changes to existing foundation, which is troublesome from the viewpoints of construction cost and time.

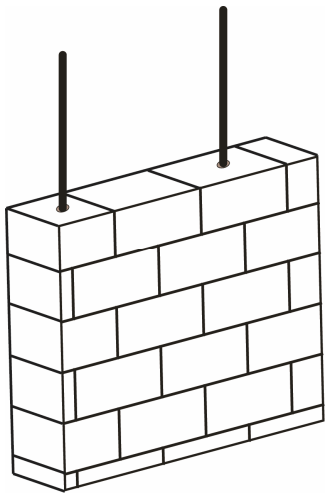

Figure 2.15: Reinforced-core technique.

2.5 PINNING RETROFIT AS AN INNOVATIVE TECHNIQUE

Difficulties associated with the preservation of historical masonry constructions, durability of strengthening materials, and also restriction on the parts of a construction to be damaged make the choice of retrofitting technique more challenging as shown clearly in Table 2.1.To overcome the above difficulties, a fairly effective retrofitting technique, where inclined stainless steel bars are inserted into the URM walls, has been applied to several historical brick buildings in Japan [28]. Fig. 2.16 shows an example of procedure involved in pinning retrofitting technique. As shown in Figs. 2.16 (a) to (f), in the retrofitting process, first, points are marked for drilling. Then holes are drilled diagonally followed by air washing of drilled holes. Then epoxy resin is injected for the bonding of reinforcing bars to the masonry elements. And finally steel bars are inserted. The preservation of appearance is attained by inserting steel bars from the mortar joints. The strength of this technique is ease of construction, wherein removal of roof and changes to foundation are unnecessary. This contributes in lower construction cost and shorter construction period. Since the stainless steel bars are inserted from the mortar joints, the retrofit technique maintains the original appearance of the URM wall.

Table 2.1: Summary on efficiency, advantage and disadvantage of conventional masonry retrofitting techniques [27].

Technique	Efficiency		Advantage	Disadvantage
	In-plane	Out-of-plane		
1. Ferrocement	$F_r \rightarrow 1.5F_{ur}$ $D_r \rightarrow 1.7D_{ur}$	Improves stability	Low cost Easy to perform Limited added mass	Space reduction Architectural impact Requires architectural finishing Limited efficiency Limited energy dissipation
2. Shotcrete	$F_r \rightarrow 3F_{ur}$ $D_r \rightarrow D_{ur}$	Improves stability	High increment in F_{ur} Improvement in energy dissipation	Space reduction Heavy mass Violation of performance level Disturbance to occupants Architectural impact Requires architectural finishing
3. Grout injection	$F_r \rightarrow 0.8\text{-}1.4F_{ur}$	Restore initial stiffness	No added mass No effect on building function No space reduction No architectural impact	Epoxy creates zones with varying stiffness and strength High cost of epoxy No significant increment in F_r using cement-based grout
4. External reinforcement	$F_r \rightarrow 4.5\text{-}10F_{ur}$ $D_r > 1.5D_{ur}$	Improves stability	High increment in F_{ur} Prevent disintegration Improvement in ductility and energy dissipation	Corrosion of external reinforcement Heavy additional mass Violation of performance level Requires architectural finishing Disturbance to occupants
5. Confined masonry	$F_r \rightarrow 1.25\text{-}1.5F_{ur}$ $D_r \rightarrow D_{ur}$	Prevent disintegration	Prevent disintegration Improvement in ductility and energy dissipation	Not easy to perform Limited effect on F_{ur} Requires architectural finishing Disturbance to occupants
6. Post-tensioning	Improves F_{ur}	Improves F_{ur}	No added mass No effect on building function	High losses Archorage problem Corrosion potential
7. Center-core	$F_r \rightarrow 2F_{ur}$ $D_r \rightarrow 1.3\text{-}1.7D_{ur}$	Improves F_{ur}	No space reduction No architectural impact No effect on building function	Creation of zones with varying stiffness and strength

F_r, F_{ur} – lateral resistance for retrofitted and unretrofitted specimens respectively and D_r, D_{ur} their respective lateral displacement.

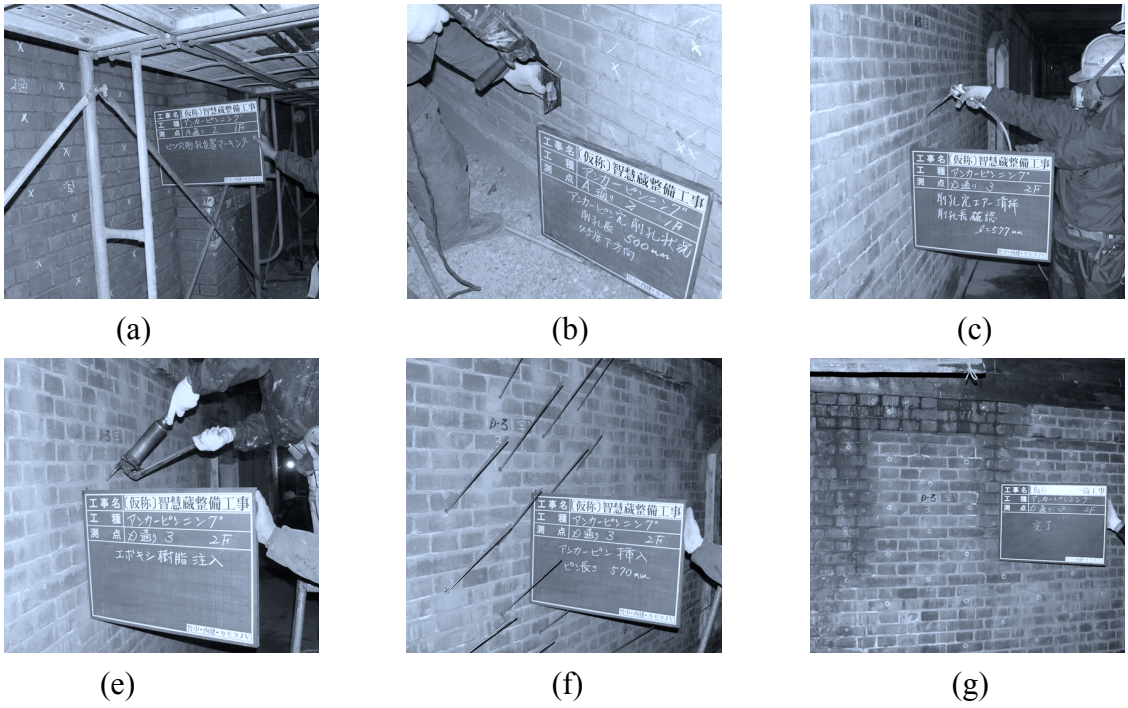

Figure 2.16: Pinning retrofitting process: (a) Marking of points for drilling, (b) Drilling at marked points, (c) Air washing of drilled holes, (d) Insertion of epoxy resin, (e)Insertion of pin, (f) Retrofitted wall after pin insertion.

Takiyama et al. [28] reported experimental results on quasi-static cyclic tests done for in-plane as well as out-of-plane loaded pinning retrofitted masonry walls. Tests showed substantial strength enhancement after initial cracking for the retrofitted specimen with its value increased by a factor of 4-6 as compared to corresponding URM specimen. High energy dissipation and enhanced ductile behavior was also observed due to successive elongation and yielding of reinforcement in tension.

2.6 NUMERICAL MODELING OF MASONRY STRUCTURES

Masonry being a composite material consists of an assemblage of bricks and mortar joints, each with different properties. Mortar joints act as plane of weakness due to their low tensile and shear strength. A detailed analysis of masonry, hereby denoted as micro-modeling, must then include a representation of each of units, mortar and

unit/mortar interface. In relatively larger and practice-oriented analysis, to catch the global structural behavior, the knowledge of the interaction between units and mortar is, generally, negligible. This case can be better handled with coarser approach called macro-modeling. Depending on the level of accuracy aimed, the following modeling strategies are available as presented in Fig. 2.17:

- Detailed micro-modeling
- Simplified micro-modeling
- Macro-modeling

Detailed micro-modeling involves brick units and mortar represented by continuum elements and unit/mortar interface represented by discontinuous interface elements. This detailed approach is suited for small structural elements with particular interest in strongly heterogeneous states of stress and strain to closely represent masonry from the knowledge of the properties of each constituent and the interface. Since both brick units and mortar joints are represented by continuum elements, Young's modulus, Poisson's ratio and optionally, inelastic properties for the both are taken into account.

Simplified micro-modeling involves strategy where expanded brick units are represented by continuum elements and the behavior of mortar joints and unit/mortar interface are lumped in discontinuous interface elements. Here each joint, consisting of mortar the two unit/mortar interfaces, is lumped into an average interface while the brick units is expanded in order to keep the geometry unchanged. Hence masonry is considered as a set of continuum elements representing brick units bonded by potential fracture/slip lines at the joints. Since mechanical properties and Poisson's effect of the mortar is not included, accuracy is lost with this modeling strategy. This approach has been applied by several researchers in studying the in-plane behavior of masonry wall panels.

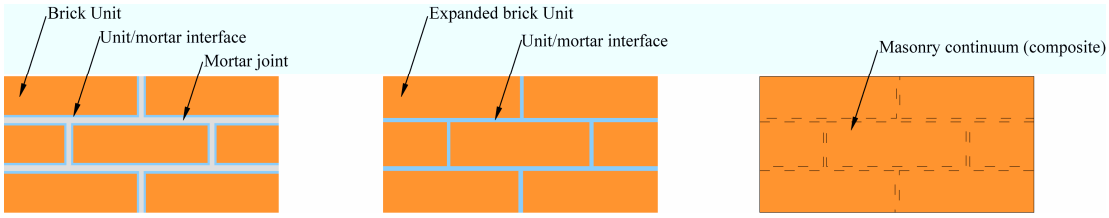

Figure 2.17: Modeling strategies for masonry: (a) Detailed micro-modeling, (b) Simplified micro-modeling, (c) Macro modeling [29].

In macro-modeling strategy, brick units, mortar joints and unit/mortar interfaces are smeared out in the continuum elements without making any distinction between individual brick units and mortar joints and treating whole masonry as a homogeneous anisotropic continuum. Here, the material is regarded as an anisotropic composite and a relation is established between average masonry strains and average masonry stresses. A complete macro model must reproduce an orthotropic material with different tensile and compressive strengths along the material axes as well as different inelastic behavior for each material axis.

The choice of the modeling strategy largely depends on the application field and accuracy aimed at. Micro-modeling is best suited for understanding the local behavior of masonry structures like a portion of an individual masonry wall panel with openings which are likely to determine the behavior of entire wall. Macro-model on the other hand would be more applicable when the structure is composed of solid walls with sufficiently large dimensions so that the stresses across or along a macro-length will be essentially uniform.

In the modeling of historical masonry structures reported by Giordano et al. [30], different modeling approaches were compared through a case study. The approaches were: (a) smeared cracking approach implemented in ABAQUS; and (b) discrete element modeling using finite element code UDEC. In smeared cracking approach, the ABAQUS concrete model was used to represent masonry. The model was a fixed multi-crack model based on a simple yield surface with isotropic hardening and

associated flow when the state of stress is predominantly compressive and used damaged elasticity to account for the cracking. In discrete element modeling, the units were meshed internally with constant strain linear elastic triangles and assumed to be isotropic linear elastic while the contacts between the units were assumed to follow an elasto-plastic law with a Coulomb slip criterion with neither cohesion nor tensile strength. The comparison of the results obtained through the different numerical models and the experimental curve is shown in Fig. 2.18 In spite of the specific limitations of each model, both the methods were able to capture the global behavior of the tested masonry wall quite accurately.

Below are reviews on few selected research citing done for continuum and discontinuum finite element modeling of masonry walls. Additionally literatures on distinct element models are also shown with their applicability in the filed of masonry structures.

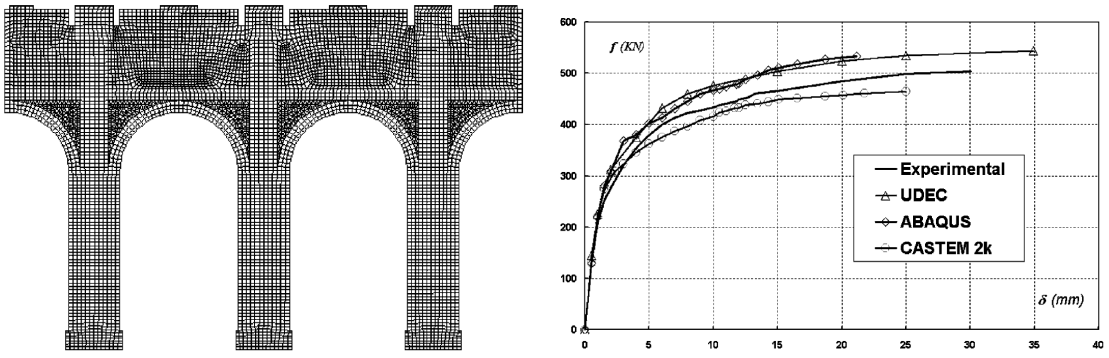

(a) (b)

Figure 2.18: Comparison of different modeling approaches: (a) FE model, (b) Experimental versus numerical curves [30].

Continuum finite element modeling

The difficulty of achieving a suitable representation of historical construction components (e.g. piers and buttresses) through a discretization in terms of structural elements has led to the use of two- and three-dimensional continuum finite elements. In this approach, masonry is simulated as a homogeneous continuum. This higher level of refinement, involving a considerable number of degrees of freedom, implies an increase in computational effort that advises the use of the continuum finite element approach for the analysis of partial or detailed models. However, quite large continuum finite element meshes are practicable with the actual computational resources. Fig. 2.19 illustrates an example for the entire façade of St. Peter's Basilica in Rome [31].

Frunzio et al. [32] reported a 3D FEM analysis for a stone masonry arch bridge as shown in Fig. 2.20. The Druker-Prager criterion was assumed as failure criterion for all the materials. The stone masonry was considered as a material obtained after a homogenization procedure, regarding the assemblage of stone blocks and mortar as a composite medium. The numerical analysis gave a 3-dimensional map of the stress and strain distribution which would be useful for restoration purpose of the masonry arch.

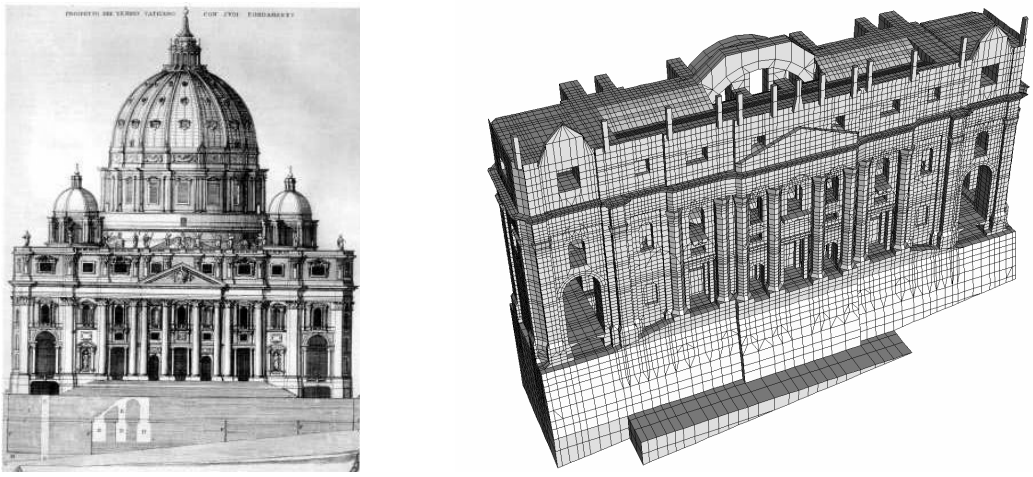

(a) (b)

Figure 2.19: Continuum finite element modeling: (a) St. Peter's Basilica in Rome, (b) Model of the entire Façade [31].

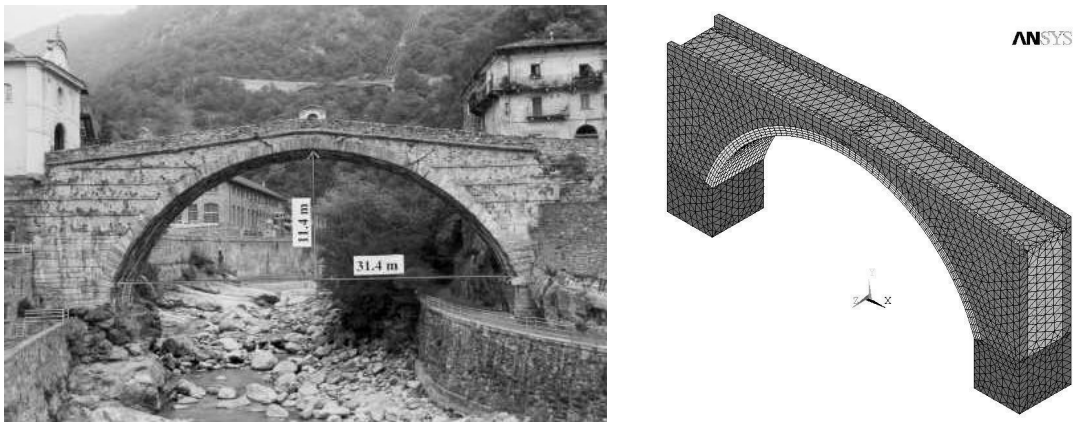

(a) (b)

Figure 2.20: 3D FEM analysis for stone masonry arch bridge: (a) Roman arch bridge of Pont St Martin, (b) FE mesh [32].

Lourenco and Rots [33] proposed an anisotropic composite continuum model for plane stress structures formulated in a modern computational plasticity format. The softening model featured a Rankine-type criterion for tension and a Hill-type criterion for compression. Good agreements were found in comparison between numerical and experimental data for masonry shear walls as shown in Fig. 2.21.

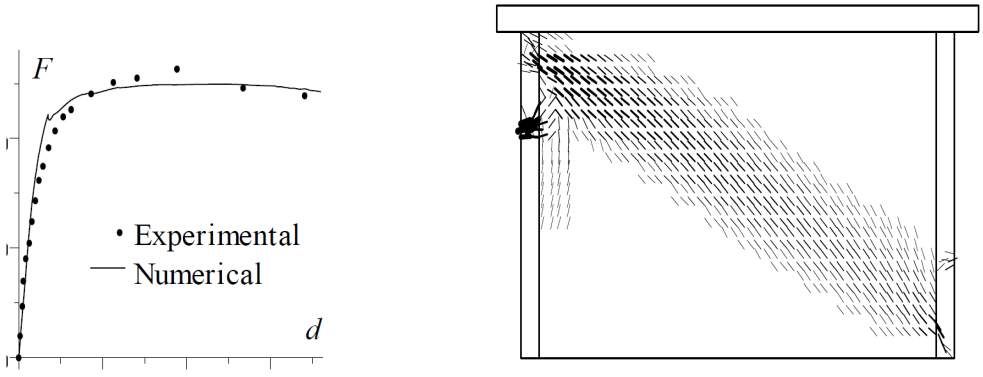

(a) (b)

Figure 2.21: Analysis of masonry shear wall with continuum finite element modeling: (a) load-displacement diagram, (b) Predicted cracking pattern at ultimate load [33].

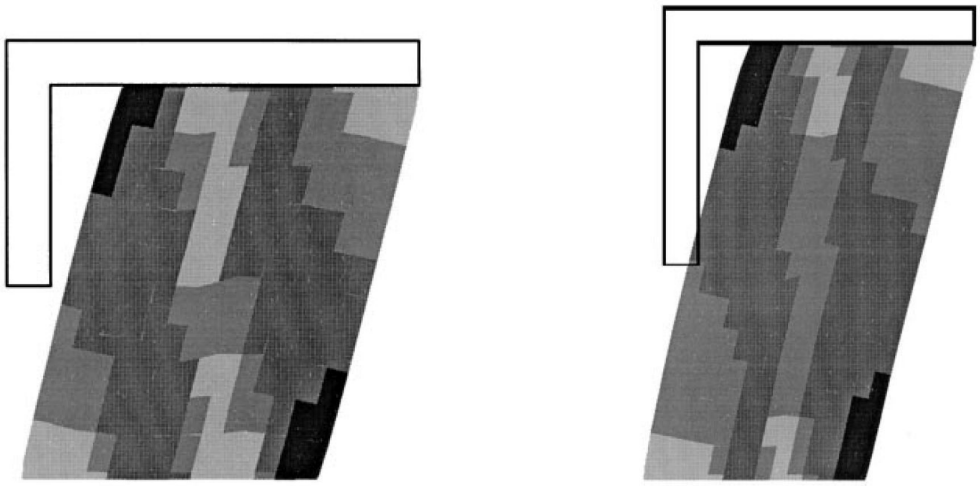

(a) (b)

Figure 2.22: Continuum model for shear wall: (a) Low wall, (b) High wall [34].

Gambarotta and Lagomarsino [34] formulated a homogenized continuum model for brick masonry as shown in Fig. 2.22. The model was implemented for the analysis of shear walls as well as large-scale masonry wall with openings involving damage model constitutive equations for the brick layer. The capabilities and validity of the proposed continuum finite element model were checked with comparisons from experimental results of slender and squat shear walls.

Discontinuum finite element modeling

Due to the higher computational effort required, discontinuum finite element models are especially adequate for the analysis of small masonry structures submitted to heterogeneous states of stress and strain. Discontinuities are generally introduced using interface elements, for which the constitutive model establishes a direct relation between the stress vector and the relative displacement vector along the interface. Here, generally the units are assumed to behave elastically, whereas the overall non- linear behavior is concentrated in the interface elements. Thus, for an accurate simulation of the masonry behavior, it is essential to develop a constitutive model for the interface elements able to capture all the failure mechanisms of masonry.

To illustrate the behavior of unreinforced masonry wall, Lourenco and Rots [29] have implemented a combined cracking-shearing-crushing interface model in well-known finite element code DIANA v9.4.2 [35]. The model is of interest to areas such as adhesives, joints in masonry walls. In DIANA v9.4.2 environment, the interface model was defined by a convex composite yield criterion, which consists of a tension cut-off, the Coulomb friction model and an elliptical cap. The developed model was verified against experimental result and substantial agreement was found between the numerical and experimental load-displacement response as shown in Fig. 2.23.

Pinto et al. [36] also proposed a discontinuum finite element model to study the pillar-arch stone structure of the S. Vicente de Fora Monastery in Lisbon, as shown in Fig. 2.24. Here, both the stone block and the masonry wall were considered as isotropic linear elastic, and joints were represented by interface elements with elasto-plastic Coulomb friction law with small dilatancy.

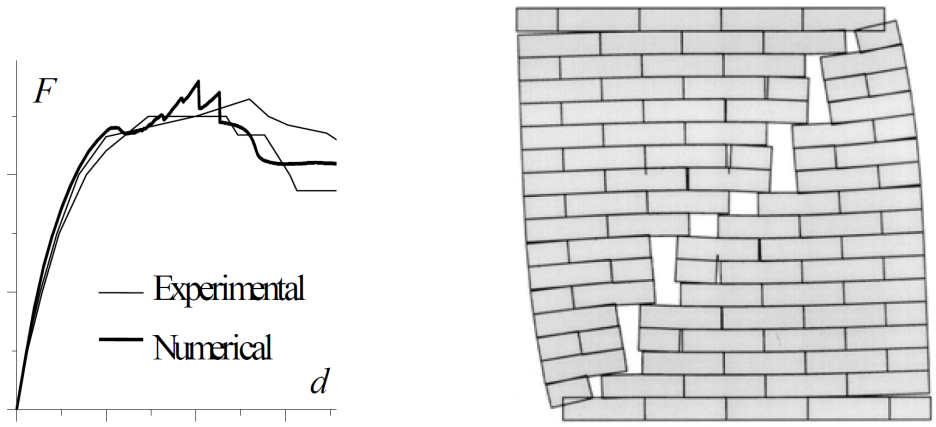

(a) (b)

Figure 2.23: Analysis of masonry shear wall with discontinuum finite element modeling: (a) load-displacement diagram, (b) Deformed mesh at ultimate load [29].

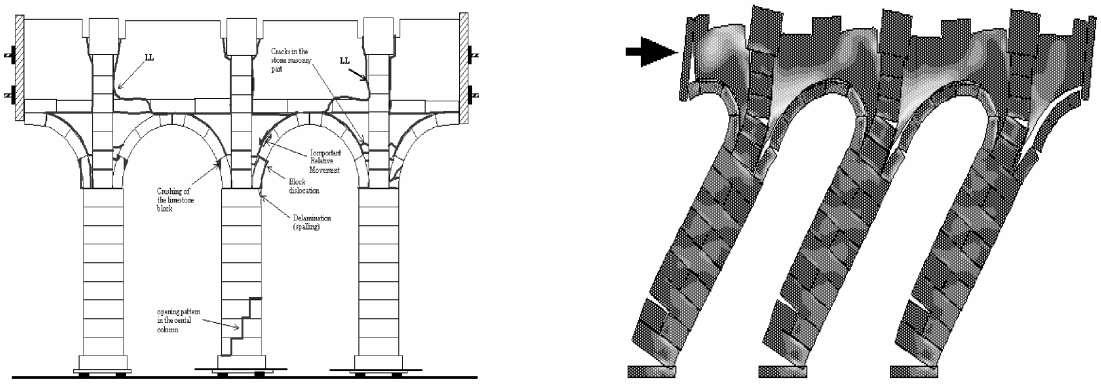

(a) (b)

Figure 2.24: Discontinuum FE modeling for S. Vicente de For a Monastery in Lisbon: (a) Damage from experimental test, (b) Deformation pattern from FE results [36].

Gambarotta and Lagomarsino [37] proposed constitutive models which take in to account the mechanical behavior of each component of masonry and its interfaces, i.e. decohesion and slipping in the mortar joints and failure in bricks. The finite element model was applied to the lateral analysis of rectangular shear walls as shown in Fig. 2.25 and the results gave response similar to the experimental observations carried out on two walls of difference shape but made up with same masonry pattern and units.

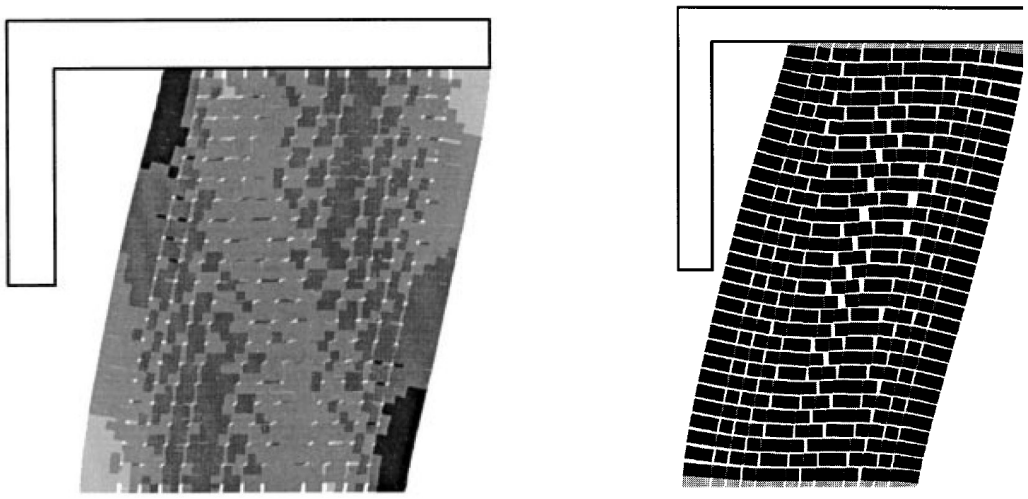

(a) (b)

Figure 2.25: Discontinuum model for shear wall: (a) Low wall, (b) High wall [37].

Distinct element modeling

The distinct, or discrete, element model has been basically used for the study of jointed rock, modeled as an assemblage of rigid blocks. Discrete element modeling approach's application in masonry has also been seen [38-40] with masonry blocks connected by means of contact points in replacement of interface elements in case of discontinuum modeling. This modeling approach is mainly adopted with an intention to simulate the large displacement range as shown in Figs. 2.26 and 2.27.

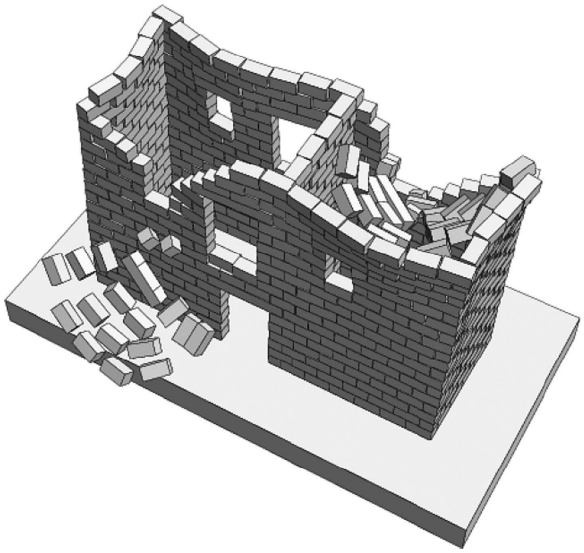

Figure 2.26: Collapse of a two-story house under seismic loading with discrete element model [38,39].

Figure 2.27: Collapse behavior sequence of wall with discrete element model [40].

2.7 APPLICATION OF SHAPE MEMORY ALLOYS (SMAs) IN RETROFITTING

Only handful numbers of researches are reported on application of SMAs in civil engineering. Here summary of literature review on application of SMAs in masonry retrofitting has been presented. The first known example of SMAs applied to retrofit project of historical masonry construction is done by Indirli et al. [41] on S. Giorgio Church Bell Tower. Seismic upgrade of the bell tower became necessary after being struck by a 4.8 Richter magnitude earthquake. The retrofit design of the 17 meters tall masonry tower was carried out under the framework of the ISTECH project. The retrofit was carried out linking top and bottom of the tower by means of hybrid tendons. In total four tendons were placed exposed in the corners of the tower as shown in Fig. 2.28. Tendons consisted of conventional steel bars in series with each shape memory alloy device. The shape memory alloy device was designed to take tension forces by means of 60 parallel superelastic NiTi wires of 1 mm diameter and 30 mm length. The tendon's prestressing was chosen to reach the superelastic plateau of the SMA. Later in the year of 2000, after a 4.5 Richter magnitude earthquake with the same epicenter, subsequent investigations of the retrofitted tower showed no evidence of damage.

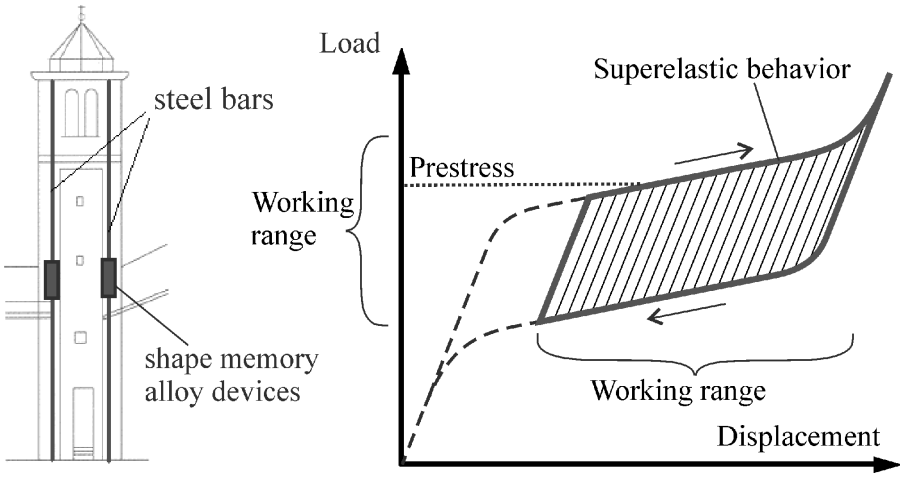

Figure 2.28: Bell tower with tendons and principle load-displacement behavior of incorporated SMA devices [41].

SMA wires were applied to several retrofitting projects of existing historical masonry constructions [37-39]. Paret et al. [42] reported innovative approaches in the seismic evaluation and strengthening of a monumental 100 year old multi story brick masonry synagougue in San Francisco. The retrofit solution consisted of a system of tension ties of super-elastic nitinol wires in the attic that interconnect the four perimeter walls, center-cored reinforcement of the masonry walls and fiber-wrap of a few critical piers.

Christis et al. [43] reported results on the application of SMA prestressing devices on an aqueduct which was built in 1747 to provide water to the city of Larnaca and to its port. Preliminary tests were done on the aqueduct with 60 cm long 3.5 mm diameter CuAlBe SMA wires arranged and connected to steel strands. The wires were fixed at the base and top of piers using bolts to support wires on a rigid base that would transfer the force onto the aqueduct.

El-Borgi et al. [44] also used copper SMAs in retrofitting of historical monuments of Mediterranean in earthquake-prone areas. Ref. [44] reported on finite element simulation, as a preliminary to an experimental study where a cantilever masonry wall, representing a part of a historical monument, was subjected to monotonic and quasi-static cyclic loadings.

REFERENCES

[1] TOMAŽEVIČ M. *Earthquake-resistant design of masonry buildings*, London: Imperial College Press, 1999.

[2] ZUCCARO G. and M. RAUCI G. Collapse Mechanisms Of Masonry Structures, *Proceedings of AIP Conference*, AIP, pp. 1168-1176, 2008.

[3] MAGENES G. and CALVI G.M. In-plane seismic response of brick masonry walls, *Earthquake Engineering & Structural Dynamics*, 26(11): 1091-1112, 1997.

[4] RAI D.C. and GOEL S.C. Seismic Strengthening of Rocking-Critical Masonry Piers, *Journal of Structural Engineering*, 133(10): 1445-1452, 2007.

[5] TAGHDI M., BRUNEAU M., and SAATCIOGLU M. Seismic retrofitting of low-rise masonry and concrete walls using steel strips, *Journal of Structural Engineering*, 126(9): 1017-1025, 2000.

[6] ZEZHEN N., QI D., JIANYOU C., and RUNTAO Y. A study of aseismic strenthening for multi-story brick buildings by additional R/C columns, Proceedings of *8th WCEE*, pp. 591-598, 1984.

[7] TOMAŽEVIČ M. and KLEMENC I. Seismic behaviour of confined masonry walls, *Earthquake Engineering & Structural Dynamics*, 26(10): 1059-1071, 1997.

[8] GAMS M. and TOMAŽEVIČ M. Experimental study of seismic behaviour of confined AAC masonry buildings, *Proceedings of 14ECEE*, Ohrid, 2010.

[9] SIGMUND V., MATOŠEVIĆ D. and BOŠNJAK M. Experimental tests of confined masonry walls, *Proceedings of 14ECEE*, Ohrid, 2010.

[10] SEKI M. Experimental Study on Confined Masonry Squat Walls, *Proceedings of 14ECEE*, Ohrid, 2010.

[11] ELGAWADY M.A., LESTUZZI P., and BADOUX M. Seismic performance of URM walls retrofitted using FRP, *NZSEE Conference*, 2005, pp. 1-8.

[12] WILLIS C.R., SERACINO R., and GRIFFITH M.C. Out-of-plane strength of brick masonry retrofitted with horizontal NSM CFRP strips, *Engineering Structures*, 32(2): 547-555, 2010.

[13] KORANY Y. and DRYSDALE R. Rehabilitation of Masonry Walls Using Unobtrusive FRP Techniques for Enhanced Out-of-Plane Seismic Resistance, *Journal of Composites for Construction*, 10(3): 213-222, 2006.

[14] MOSALLAM A.S. Out-of-plane flexural behavior of unreinforced red brick walls strengthened with FRP composites, *Composites Part B: Engineering*, 38(5,6): 559-574, 2007.

[15] ABRAMS D., SMITH T., LYNCH J., and FRANKLIN S. Effectiveness of Rehabilitation on Seismic Behavior of Masonry Piers, *Journal of Structural Engineering*, 133(1): 32-43, 2007.

[16] KARANTONI F.V. and FARDIS M.N. Effectiveness of Seismic Strengthening Techniques for Masonry Buildings, *Journal of Structural Engineering*, 118(7): 1884-1902, 1992.

[17] PERRET S., KHAYAT K.H., GAGNON E., and RHAZI J. Repair of 130-Year Old Masonry Bridge using High-Performance Cement Grout, *Journal of Bridge Engineering*, 7(1): 31-38, 2002.

[18] SCHULLER M., ATKINSON R., and BORGSMILLER J. Injection grouting for repair and retrofit of unreinforced masonry, *Proceedings of 10th IB2MAC*, Canada, 1994.

[19] CALVI G. and MAGENES G. Experimental results on unreinforced masonry shear walls damaged and repaired, *Proceedings of 10th IB2MAC*, Canada, 1994.

[20] MOJSILOVIC N. and MARTI P. Load Tests on Post-Tensioned Masonry Walls, *TMS Journal*, 65-70, 2000.

[21] OUSALEM H., MIYAUCHI Y., MASATO Y. and KIBAYASHI M. Experimental Investigation of Post-Tensioned Brick Masonry Bearing Walls, *Proceedings of 14ECEE*, Ohrid, 2010.

[22] LAURSEN P.T. Seismic performance of prestressed concrete masonry walls incorporating energy dissipators, *Proceedings of 14WCEE*, Beijing, 2008.

[23] FOTI D. and MONACO P. Post-tensioned masonry: state of the art, *Progress in Structural Engineering and Materials*, 2(3): 311-318, 2000.

[24] PLECNIK B.J., COUSINS T., and CONNER E.O. Strengthening of unreinforced masonry buildings, *Journal of Structural Engineering*, 112(5):1070-1087, 1986.

[25] LIN Y.C., CHANG J.S., and HONG C.Y. Out-of-plane Seismic Damage and Related Evaluation - Illustrated with A Masonry Historic Building in Taiwan, *Proceedings of 14ECEE*, Ohrid, 2010.

[26] BUTTON M.R. and MAYES R.L. Out-of-plane seismic response of reinforced masonry walls, *Journal of Structural Engineering*, 118(9):2495-2513, 1992.

[27] ELGAWADY M., LESTUZZI P., and BADOUX M. A review of conventional seismic retrofitting techniques for URM, *Proceedings of 13th Brick Block Masonry Conference*, 2004.

[28] TAKIYAMA N., NAGAE T., MAEDA H., KITAMURA M., YOSHIDA N., and ARAKI Y. Cyclic out-of-plane flexural behavior of masonry walls rehabilitated by inserting stainless pins, *Proceedings of 14WCEE*, Beijing, 2008.

[29] LOURÉNÇO P.B. and ROTS J.G. Multisurface interface model for analysis of masonry structures, *Journal of Engineering Mechanics*, 123(7): 660-668, 1997.

[30] GIORDANO A., MELE E. and LUCA A.D. Modelling of historical masonry structures: comparison of different approaches through a case study, *Engineering Structures*, 24(8): 1057-1069, 2002.

[31] MACCHI G. Diagnosis of the facade of St . Peter ' s Basilica in Rome, *Historical Constructions*, P.B. Lourenco and P. Roca, eds., Guimarães, Universidade do Minho, 2001, pp. 309-318.

[32] FRUNZIO G., MONACO M., and GESUALDO A. 3D F.E.M. analysis of a Roman arch bridge, *Historical Constructions*, P.B. Lourenço and P. Roca, eds., Guimarães, 2001, pp. 591-598.

[33] LOURÉNÇO P.B., DE BORST R., and ROTS J.G. A plane stress softening plasticity model for orthotropic materials, *International Journal for Numerical Methods in Engineering*, 40(21): 4033-4057, 1997.

[34] GAMBAROTTA L. and LAGOMARSINO S. Damage Models for the Seismic Response of Brick Masonry Shear Walls. Part II: the Continuum Model and Its Applications, *Earthquake Engineering & Structural Dynamics*, 26(4), Apr. 1997, pp. 441-462.

[35] DIANA9.3, *DIANA User's Manual Release 9.3*, TNO DIANA BV, Delft, 2008.

[36] PINTO A., MOLINA J., PEGON P., and RENDA V. Protection of the cultural heritage at the ELSA Laboratory, *Historical Constructions*, P.B. Lourenço and P. Roca, eds., Guimarães, 2001, pp. 973-982.

[37] GAMBAROTTA L. and LAGOMARSINO S. Damage Models for the Seismic Response of Brick Masonry Shear Walls. Part I: the Mortar Joint Model and Its Applications, *Earthquake Engineering & Structural Dynamics*, 26(4): 423-439, 1997.

[38] LEMOS J.V. Discrete Element Modeling of Masonry Structures, *International Journal of Architectural Heritage*, 1(2): 190-213, 2007.

[39] ALEXANDRIS A., PROTOPAPA E., and PSYCHARIS I. Collapse mechanisms of masonry buildings derived by the distinct element method, *Proceedings of 13WCEE*, 2004.

[40] FURUKAWA A., KIYONO J., and TOKI K. Proposal of a Numerical Simulation Method for Elastic , Failure and Collapse Behaviors of Structures and its Application to Seismic Response Analysis of Masonry Walls, *Journal of Disaster Research*, 6(1): 51-69, 2011.

[41] INDIRLI M., CASTELLANO M., CLEMENTE P., and MARTELLI A. Demo-application of shape memory alloy devices: The rehabilitation of the S. Giorgio Church Bell-Tower, *Proceedings of SPIE*, 2001.

[42] PARET T., FREEMAN S., SEARER G., HACHEM M., and GILMARTIN U. Using traditional and innovative approaches in the seismic evaluation and strengthening of a historic unreinforced masonry synagogue, *Engineering Structures*, 30(8): 2114-2126, 2008.

[43] CHRISTIS Z.C., ANDREAS S., THEMOS D., and KARIM H. Application of shape memory alloy prestressing devices on an ancient aqueduct, *Smart Structures and Systems, An International Journal*, 4(2): 261-278, 2008.

[44] EL-BORGI S., NEIFAR M., JABEUR M.B., CHERIF D., and SMAOUI H. Use of copper shape memory alloys in retrofitting historical monuments, *Smart Structures and Systems, An International Journal*, 4(2): 247-259, 2008.

3

FINITE ELEMENT MODELING OF PINNING RETROFITTED MASONRY WALLS

3.1 GENERAL

Recognizing the shortcomings of unreinforced masonry (URM) walls, there has been a surge of interest in recent years to develop techniques for improving their seismic behavior. Past research works [1-5] done for improving the seismic performance of unreinforced masonry (URM) walls involve: (1) attachment of reinforcing members, (2) surface treatment, (3) grout injection, (4) post-tensioning, and (5) reinforced core technique. As reported previously in Chapter 2, the first two techniques usually change the appearance of URM constructions significantly and may cease their aesthetic value, which is problematic especially in retrofitting historical masonry constructions. Although the rest of the techniques do not cause significant changes to the appearance of URM constructions, they have shortcomings. Grout

injection does not improve ductility. The other two techniques require removal of roof and changes to existing foundation, which are troublesome from the viewpoints of construction cost and time. Difficulties associated with the preservation of historical masonry constructions, durability of strengthening materials, and also restriction on the parts of a construction to be damaged make the choice of retrofitting technique more challenging.

To overcome the above difficulties, a fairly effective retrofitting technique, where inclined stainless steel bars are inserted into the URM walls, has been proposed by Takiyama et al. [6-7]. The details on this pinning technique have been given in detail in Chapter 2. The strength of this technique is ease of construction, wherein removal of roof and changes to foundation are unnecessary. This contributes in lower construction cost and shorter construction period. Since the stainless steel bars are inserted from the mortar joints, the retrofit technique maintains the original appearance of the URM wall. Nonetheless, to the authors' knowledge, no numerical modeling has been performed for the masonry walls retrofitted by this technique. This chapter reports on the finite element (FE) study on pinning retrofitting technique practiced on walls when subjected to in-plane [8] and out-of-plane [9] loading. The chapter first describes the various material tests performed on masonry assemblages to acquire the masonry mechanical properties followed by the respective FE results for in-plane and out-of-plane loaded masonry walls separately.

3.2 MICRO-EXPERIMENTS FOR DETERMINATION OF MASONRY MECHANICAL PROPERTIES

Micro-experiments on masonry assemblages have been performed for the determination of the material mechanical characteristics required as input data for proper numerical modeling. The following subsections describe briefly on the tests

done and their corresponding results.

3.2.1 Triplet shear test for interface between masonry and mortar

Fig. 3.1 shows the set-up for the triplet shear test on masonry assemblage [10]. The test is performed for the determination of the following parameters: cohesion c, angle of friction φ_o, residual friction angle φ_r. The tests gave cohesion value, c = 0.24 MPa, tangent of friction angle, $\tan\varphi_o$ = 1.1 and residual friction angle, $\tan\varphi_r$ = 1.1.

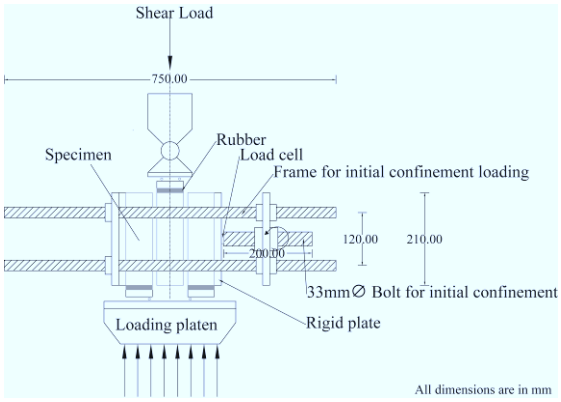

(a)

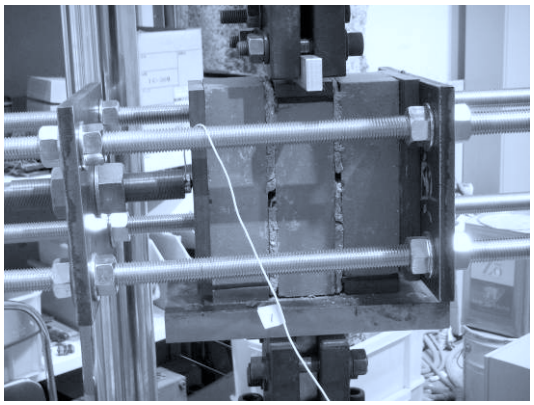

(b)

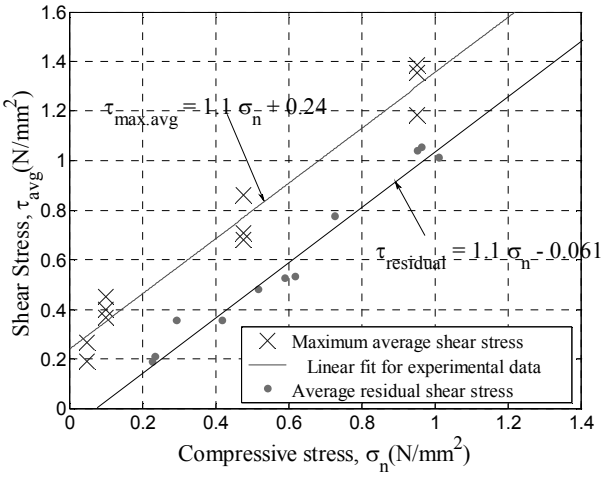

(c)

Figure 3.1: Triplet shear test: (a) Test specimen and set-up, (b) Experimental observation, (c) Shear stress versus normal stress plot.

3.2.2 Compressive test on brick unit and masonry prism

Fig. 3.2 shows the set-up for the compressive test on masonry assemblage [10]. The tests were performed for the determination of Young's Modulus of Elasticity of brick units and masonry assemblages. For the calculation of Young's Modulus of elasticity, secant modulus was computed taking stress and strain increments between 1/20th and 1/3rd of the maximum compressive strength recorded.

Elastic modulus of brick unit, E_u and masonry prism, E_m can be determined directly using the strain measurement results as shown in Tables 3.1 and 3.2. The elastic modulus of mortar is determined assuming that the total vertical displacement of the prism is equal to the sum of the vertical displacements of the joints and the brick units. The Young's modulus for mortar can be computed using Eq. (3.1) as given below,

$$E_{mort} = \frac{E_m E_u}{\alpha(E_u - E_m) + E_u}$$
$$\alpha = h_u / h_{mort} \tag{3.1}$$

where h_u and h_{mort} represent thickness of brick unit and mortar joint respectively. The average value for Young's modulus of mortar, E_{mort} was computed to be 291 MPa using Eqn. 3.1.

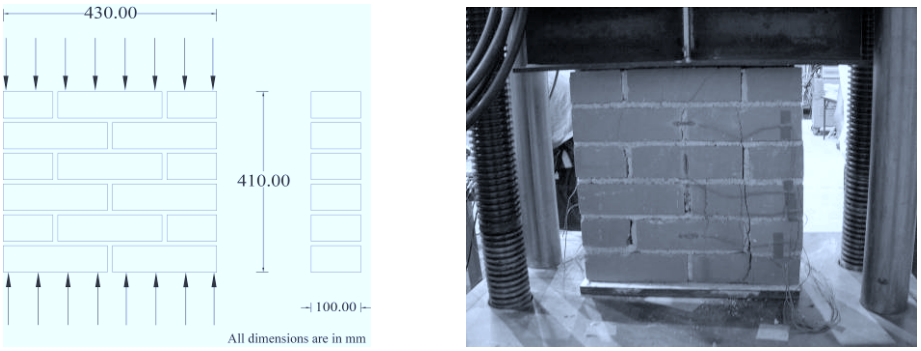

Figure 3.2: Compression test: (a) Test specimen and set-up, (b) Experimental observation.

Table 3.1: Results for compressive tests done on brick units.

Specimen	Maximum compressive strength (MPa)	Secant Young's modulus (E_u) (MPa)
1	10.413	32068.377
2	9.169	39064.230
3	10.541	90500.940
4	10.419	76673.714

Table 3.2: Results for compressive tests done on masonry assemblage (prism).

Specimen	Maximum compressive strength (MPa)	Secant Young's modulus (E_m) (MPa)
1	10.413	1921.120
2	9.169	1983.753
3	9.843	1473.358
4	11.703	2299.798
5	10.541	1991.021
6	10.419	2254.207

These values of elastic modulus computed were in turn used for the computation of normal and shear stiffness of the unit/mortar interface joint using Eq. (3.2) as given below,

$$D_{11} = \frac{E_u E_{mort}}{h_{mort}(E_u - E_{mort})}$$
$$D_{22} = \frac{G_u G_{mort}}{h_{mort}(G_u - G_{mort})} \quad (3.2)$$

where G_u and G_{mort} are their respective shear moduli. The values for normal and shear stiffness of unit/mortar interface computed using Eq. (3.2) were D_{11} = 30 N/mm^2/mm and D_{22} = 13 N/mm^2/mm.

3.2.3 Modulus of rupture test

Modulus of rupture test [11] was done on masonry prism as shown in Fig. 3.3 to get the tensile strength of mortar joint. The value of tensile strength, f_t is determined using Eqn. 3.3 as shown below,

$$f_t = \frac{3PL}{2bt^2} \tag{3.3}$$

where the dimensions are shown in Fig. 3.3.

3.2.4 Pull-out bond tests of epoxy resin

The pull-out tests were performed to get the measure of bond strength of epoxy resin. The bond strength observed was extremely high with fracture of pin observed for bond length exceeding 30 mm as shown in Fig. 3.4. Based on these observations, a valid assumption of perfect bond model could be adopted during FE modeling.

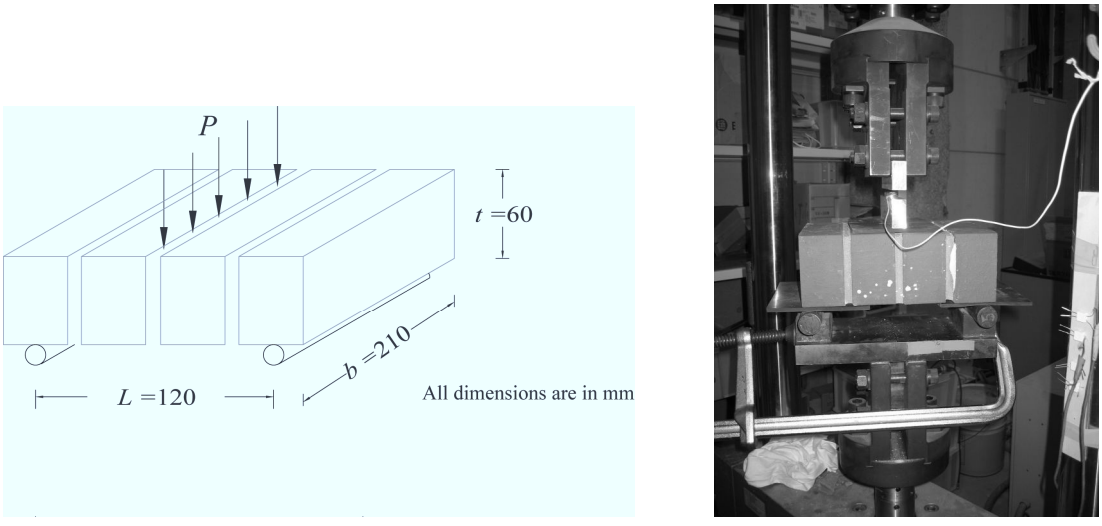

Figure 3.3: Modulus of rupture test: (a) Specimen and test set-up, (b) Experimental observation.

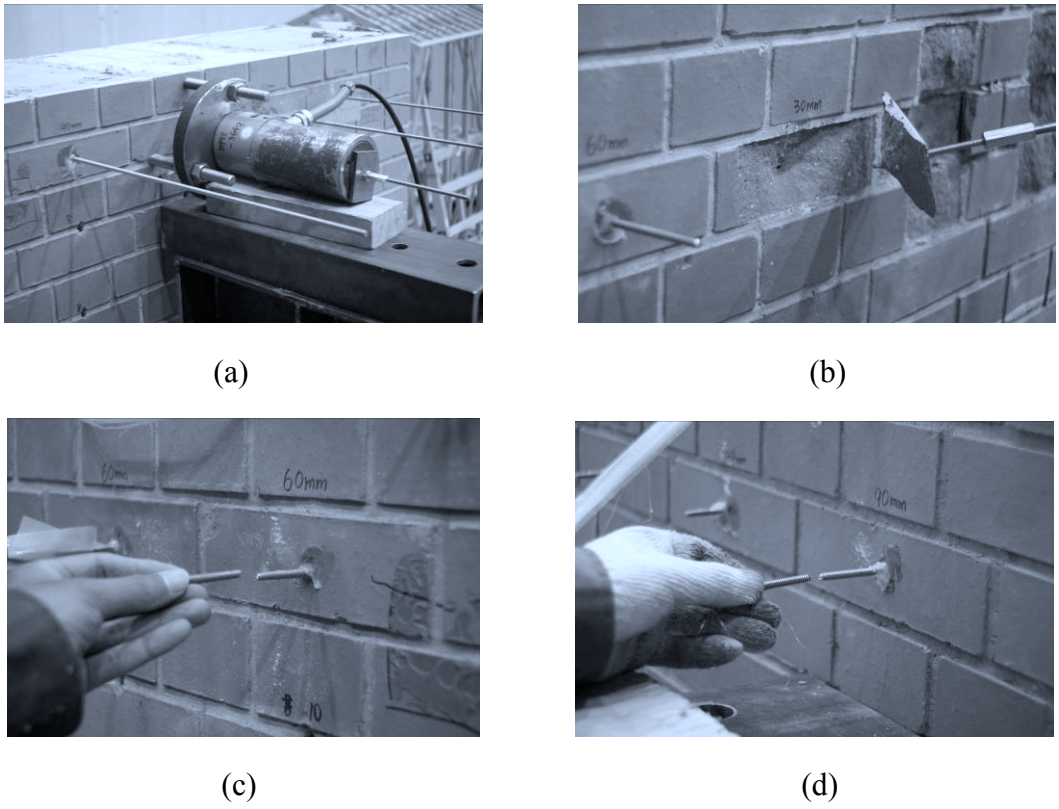

(a) (b)

(c) (d)

Figure 3.4: Pull-out test: (a) Test set-up, (b) Brick failure for 30 mm bond length, (c) Pin fracture at 60 mm bond length, (d) Pin fracture at 90 mm bond length.

3.3 FINITE ELEMENT MODELING OF IN-PLANE SHEAR LOADED MASONRY WALL WITH OPENING

3.3.1 Masonry wall specimen with opening

Figs. 3.5 and 3.6 show the geometry of the URM and RM specimens respectively. Pinning retrofitting technique involves insertion of inclined stainless steel bars into the brick walls diagonally from the mortar joints in the plane perpendicular to the wall as shown in Fig. 3.6. Note that the locations of the reinforcing bars inserted from one side of the wall were slightly displaced from those of the reinforcing bars inserted from the other side of the wall as shown in Fig. 3.6. The circles in the figures indicate the front location from where steel bars are inserted diagonally. Additionally, for RM specimens,

reinforcing bars are also inserted in the horizontal direction just above and below the opening on both faces of walls, purely to provide shear resistance and resist diagonal shear cracking of wall. Effectiveness of bed joints structural repointing to enhance the shear resistance of masonry walls have been investigated by numerous previous studies [12-15]. In the present retrofitting technique, the process of insertion involves first removal of mortar along the bed mortar joint level using grinder to make a straight groove 10 mm thick and 10-15 mm deep. This is followed by application of first layer of epoxy resin in the incision formed. Afterwards reinforcing bar is inserted and finally a second layer of epoxy resin is applied to cover the bar sufficiently. It should be noted that the proposed technique does not show particularly any difficulty in application.

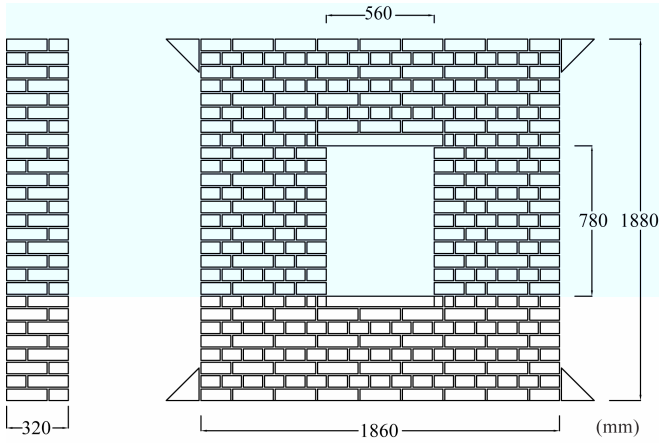

Figure 3.5: Unreinforced masonry (URM) Specimen.

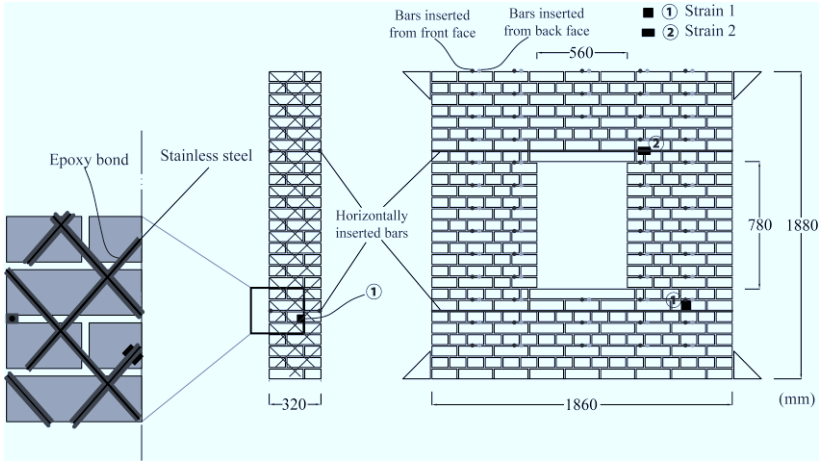

Figure 3.6: Reinforced masonry (RM) Specimen.

3.3.2 Masonry wall FE model

General strategy

Masonry walls, subjected to in-plane shear loading, predominantly undergo tensile and shear failure in mortar joints with very minimal compressive masonry failure. The in-plane response is often governed by cracking at mortar joints and rocking resistance due to gravity. Masonry walls can therefore be represented by simplified interface elements [16] – an approach that does not distinguish failure of the brick-mortar interface from that of the mortar layer itself. Here, a 2D FE model was generated and analyzed using the DIANA9.3 FE program [17], with modeling assuming that brick units are fully elastic and that all material nonlinearity is concentrated on the unit/mortar interface. For reinforced masonry walls, reinforcing bars are represented by truss elements. For 2D representation of inclined inserted bars, authors have introduced the concept of simplified equivalent vertical bar model where inclined inserted bars in a 3D model is replaced by an equivalent vertical bar in a 2D plane. The proposed 2D FE model [8] is validated by comparisons with the experimental results [7]. Rocking resistance due to gravity is considered by including geometric nonlinearity in the analysis.

Brick unit model

A masonry brick unit was modeled using rectangular continuum elements connected to vertical and horizontal interface elements. An FE model with meshing for a brick unit is shown in Fig. 3.7. As stated, brick units were modeled to be perfectly elastic during the whole loading history and modeled with four-node quadrilateral continuum elements. Material properties used include Young's modulus, E_{brick} = 20 GPa, Poisson's ratio, υ_{brick} = 0.15, and density, ρ_{brick} =2000 kg/m^3. These material constants were obtained through compressive tests in masonry prisms and brick units. Additionally, for the potential cracks in the bricks, brick crack interface was also modeled with its

location as shown in Fig. 3.7. A simple discrete cracking model, where a gap arises if tensile traction normal to the interface exceeds tensile strength of 2 MPa, was assumed [16]. It should be noted that we limited the location of brick crack interfaces along the line of mortar joints so as to limit number of elements in FE model. Assignment of zero-thickness interface element meant the length of reinforcing bar between the two corresponding nodes to be zero which is undesirable. For this reason, here brick/mortar interface and brick/crack interface has an actual thickness of 10 mm representing the thickness of mortar joint. As a result, there exists small error in the FE geometry but this has very negligible effect on the final response of specimen.

Mortar joint model

An entire mortar joint is represented by a brick unit/mortar interface model implemented in DIANA9.3 [17] as linear interface elements between two lines (2+2 nodes). The constitutive model was a Coulomb friction criterion with tension cut-off. A gap arises if tensile traction normal to the interface exceeds tensile strength of 0.2 MPa. A slip occurs if traction parallel to the interface exceeds shear strength of 0.24 MPa. We obtained tensile strength through bending tests on masonry assemblages [11] and shear strength through shear tests done on masonry triplets [10]. After the gap forms, tensile traction immediately drops to zero, representing brittle cracking.

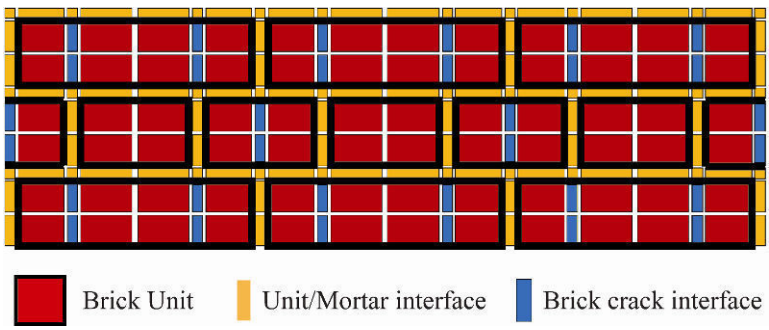

Figure 3.7: Masonry unit, unit/mortar interface and brick crack interface discretization (shrinked mesh).

The model follows classical elastic-plastic formulation:

$$\dot{\boldsymbol{t}} = \boldsymbol{D}^{\mathrm{e}} \Delta \dot{\boldsymbol{u}}^{\mathrm{e}} \tag{3.4}$$

$t = \{t_{\mathrm{n}}\ t_{\mathrm{t}}\}^{\mathrm{T}}$, with t_{n} and t_{t} normal and shear stress at the interface and D^{e} the diagonal matrix with elastic constants D_{11} and D_{22}. Total relative displacement rate $\Delta \dot{u}$ is assumed to decompose into reversible part $\Delta \dot{u}^{\mathrm{e}}$ and irreversible part $\Delta \dot{u}^{\mathrm{P}}$:

$$\Delta \dot{\boldsymbol{u}} = \Delta \dot{\boldsymbol{u}}^{\mathrm{e}} + \Delta \dot{\boldsymbol{u}}^{\mathrm{P}} \tag{3.5}$$

$\Delta u = \{\Delta u_{\mathrm{n}}\ \Delta u_{\mathrm{t}}\}$, with Δu_{n} and Δu_{t} relative normal and shear displacement across a crack. The following Coulomb friction yield surface models the fracture:

$$\boldsymbol{f} = \sqrt{\boldsymbol{t}_{\mathrm{t}}^2} + \boldsymbol{t}_{\mathrm{n}} \tan \boldsymbol{\varphi}(\boldsymbol{\kappa}) - \bar{\boldsymbol{c}}(\boldsymbol{\kappa}) = 0 \tag{3.6}$$

$\tan \boldsymbol{\varphi}(\boldsymbol{\kappa})$ is the friction coefficient as a function of internal parameter $\boldsymbol{\kappa}$ and $\bar{\boldsymbol{c}}(\boldsymbol{\kappa})$ cohesion as a function of internal parameter $\boldsymbol{\kappa}$. Internal parameter $\boldsymbol{\kappa}$ evolution is assumed given by the irreversible relative displacement component in tangential direction as $\dot{\boldsymbol{\kappa}} = \left| \Delta \dot{\boldsymbol{u}}_{\mathrm{t}}^{\mathrm{P}} \right|$ using the following plastic potential surface:

$$\boldsymbol{g} = \sqrt{\boldsymbol{t}_{\mathrm{t}}^2} + \boldsymbol{t}_{\mathrm{n}} \tan \boldsymbol{\psi} \tag{3.7}$$

The direction of irreversible displacement is given by plastic potential function $\boldsymbol{g}$. Uplift is determined by dilatancy angle $\boldsymbol{\psi}$, with $\Delta \dot{\boldsymbol{u}}^{\mathrm{P}} = \dot{\lambda} \partial \boldsymbol{g} / \partial \boldsymbol{t}$, where λ is the plastic multiplier. Tests on shear triplets [10] determined shear parameters to be c = 0.24 MPa and $\tan\varphi$ = 1.1. The dilatancy angle is $\tan\psi$ = 0.6 [12]. Using Eqn. 3.2, normal stiffness D_{11}=30 N/mm^3 and shear stiffness D_{22}= 13 N/mm^3 are used for the unit/mortar interface.

Additionally, two special mortar joints are also included in the modeling. Strong mortar joint just above and below the horizontally inserted reinforcing bar to represent

the epoxy resin and weak mortar joint at the interface between the top beam and wall specimen as shown in Fig. 3.8. Discrete crack model is used, where a gap arises if tensile traction normal to the interface exceeds tensile strength of 4 MPa for strong mortar joint and 0.05 MPa for weak mortar joint.

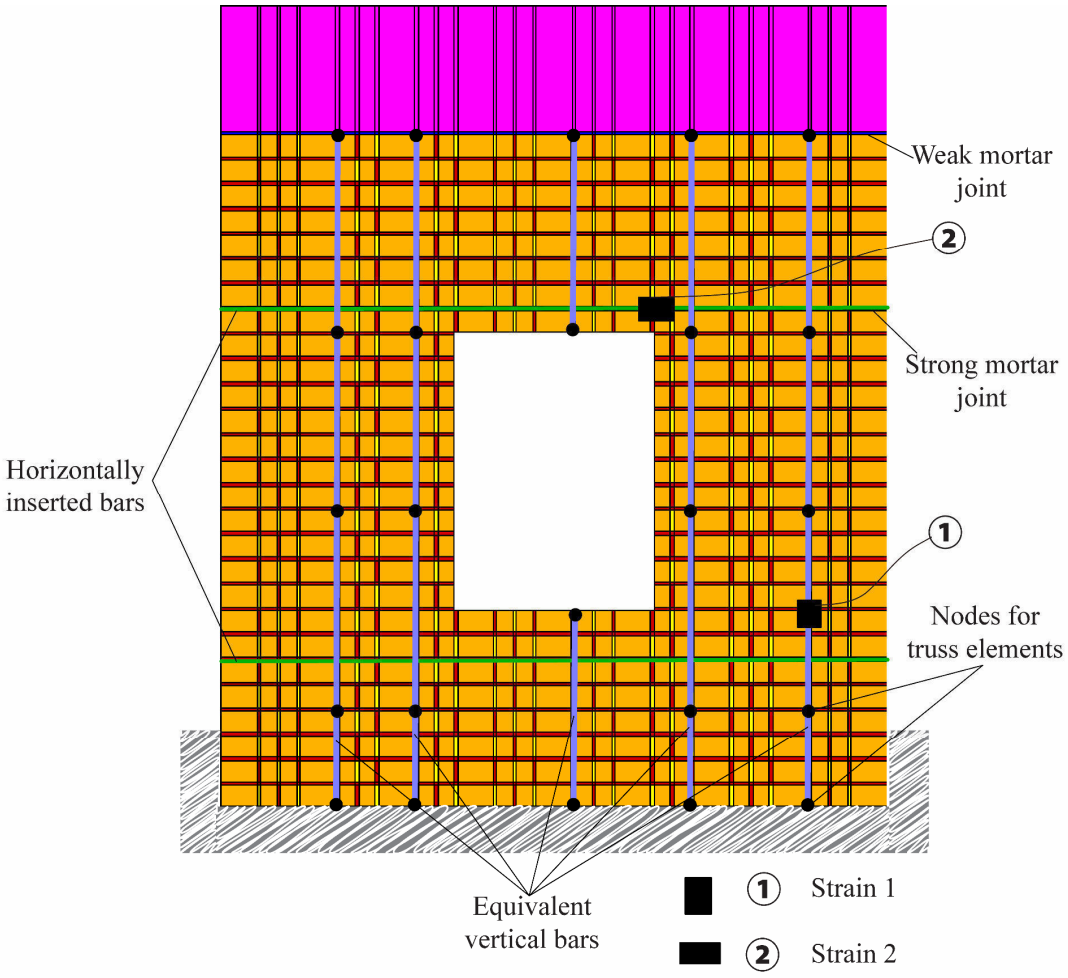

Figure 3.8: Finite element (FE) model for RM specimen.

Equivalent vertical bar model

For 2D representation of inclined inserted bars, authors have proposed a simplified equivalent vertical bar model, as shown in Fig. 3.9, where model with cross pinning at 45 degree in Fig. 3.9(a) is represented by a 2D equivalent vertical bar model in Fig. 3.9(b). The equivalent vertical bar model facilitates in providing both stability as well as reduction in computation burden as compared to more complex 3D FE model.

As shown in Fig. 3.8, equivalent vertical bars are shown by thick vertical solid lines. Black circles show nodes where truss and continuum elements are connected. Material properties are represented by elastic perfectly plastic properties adopting Young's modulus for steel E_{st}=210 GPa and yield stress f_y = 600 MPa. It should be noted that fully threaded stainless steel reinforcing bars (SUS304) were used for retrofitting to provide good bond strength. Material properties adopted for the reinforcing bars are based on tensile tests performed on threaded bars.

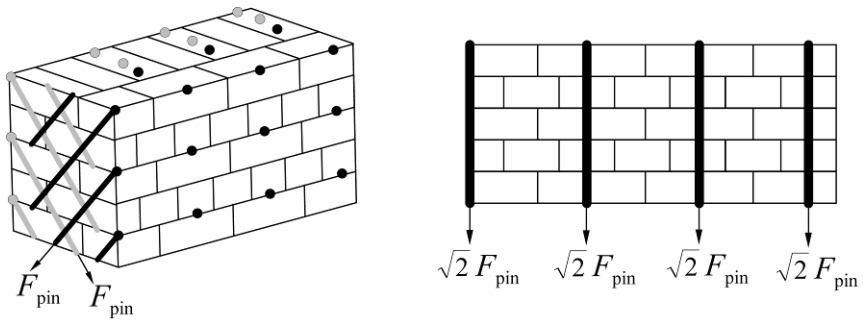

(a) (b)

Figure 3.9: Pinning technique: (a) Cross pinning retrofitting (b) 2D Equivalent vertical bar model.

To determine the equivalent vertical bar cross-sectional area, we count minimum number n of steel bars at the wall's critical section. As shown in Fig. 3.6, reinforced specimen has 2 lines of reinforcement, i.e., at least 2 reinforcing bars at any horizontal wall section. Bars are inclined at a $\pi/4$ radian to the vertical axis, so cross-sectional area $A_{\text{bar}}^{\text{eq}}$ of the equivalent vertical bar is computed as $A_{\text{bar}}^{\text{eq}} = nA_{\text{bar}}\cos(\pi/4)$. A_{bar} is the cross-sectional area of each stainless steel bar.

Horizontally inserted bar model

A stainless steel bar is presented by a two-node truss element with material properties represented by elastic perfectly plastic properties adopting Young's modulus for steel E_{st}=210 GPa and yield stress f_{y} = 600 MPa -- material constants obtained from tensile tests on stainless steel bar specimens 6 mm in diameter. Similar fully threaded stainless steel bars (SUS304) were used as horizontally inserted bars. Green horizontal lines in Fig. 3.8 represent the horizontally inserted bar in the FE model.

Pull-out tests as reported earlier showed the bond between the reinforcing bar and masonry elements to be stronger than that of the reinforcing bar for minimum bond length of 60 mm which is generally met for the retrofitted specimen as shown in Fig. 3.6. For this reason, both ends of each truss element were connected to corresponding nodes of continuum elements representing bricks and no relative displacement was allowed between truss element end nodes and corresponding continuum element nodes.

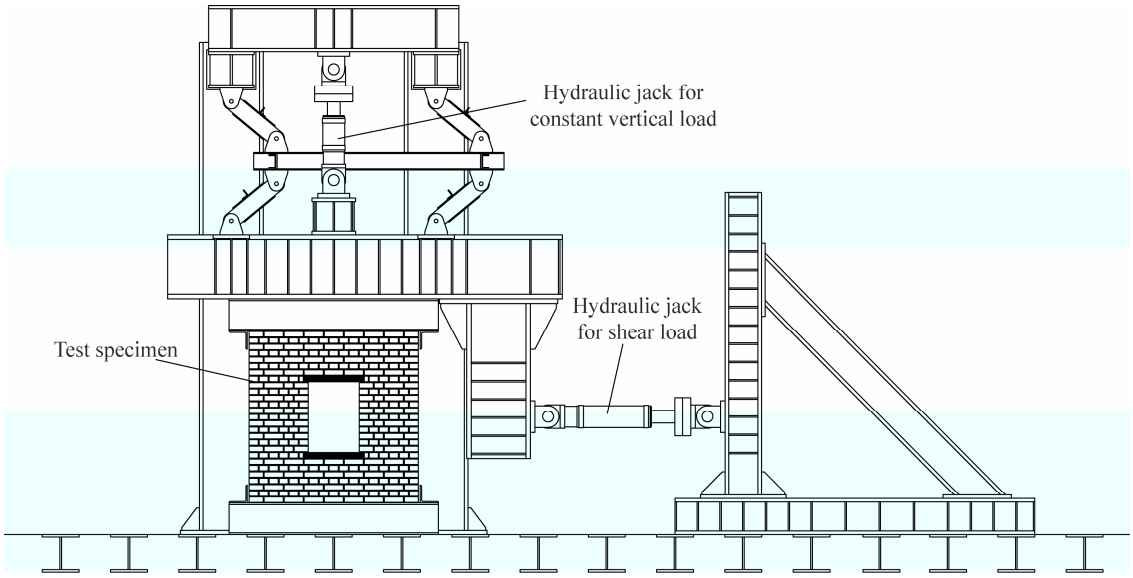

Figure 3.10: Experimental test set up.

3.3.3 Loading and boundary conditions

The test setup in Fig. 3.10 has the in-plane shear load coming at the top section of wall, with constant vertical load of 20 kN at the top. A displacement-controlled cyclic load was provided to make maximum rotation angle θ_{max} of the wall specimen equal to ±1/500, 1/400, 1/200, 1/100, 1/66, 1/50, 1/33 and 1/20 radian. Numerical model includes a multi point constraint at the top portion of the specimen for horizontal and vertical translational motion, restraining the rotation of the top portion of wall, to meet the experimental boundary conditions. The authors have limited presentation of the experimental and numerical results for URM specimen with rotation angle up to θ_{max}<1/400 radian and for RM specimen up to θ_{max}<1/200 radian only since these small deformation ranges are important for design purposes. Additionally there were also convergence problems during FE analysis at large deformation angle.

3.3.4 Theoretical predictions

Collapse capacity of reinforced and unreinforced masonry walls with opening subjected to in-plane shear load can be effectively predicted assuming the failure

mechanism with designated plastic locations and computing the rocking resistance based on equilibrium states [18]. Failure mechanism depends on the relative strength of element sections with two extreme cases -- (1) Strong pier-weak beam mechanism and (2) Strong beam-weak pier mechanism. Both these mechanisms are illustrated in Figs. 3.11 and 3.12.

3.3.4.1 Strong pier-weak beam mechanism

From Fig. 3.11, with strong pier-weak beam failure mechanism, following equilibrium conditions for RM specimen can be obtained from the given free body diagrams:

From free body T*:

$$\begin{aligned} F_{\mathrm{R}} &= F_{\mathrm{A}}^{\mathrm{H}} + F_{\mathrm{B}}^{\mathrm{H}} \\ F_{\mathrm{v}} &= F_{\mathrm{A}}^{\mathrm{v}} + F_{\mathrm{B}}^{\mathrm{v}} \end{aligned} \tag{3.8}$$

From free body A*:

$$F_{\mathrm{A}}^{\mathrm{H}} h_1 = F_{\mathrm{A}}^{\mathrm{v}} L + H h_2 + w_{\mathrm{d}} L/2 + F_{\mathrm{p}}(L_{\mathrm{p1}} + L_{\mathrm{p2}}) \tag{3.9}$$

From free body B*:

$$F_{\mathrm{B}}^{\mathrm{H}} h_1 = F_{\mathrm{B}}^{\mathrm{v}} L - H h_2 + w_{\mathrm{d}} L/2 + F_{\mathrm{p}}(L_{\mathrm{p3}} + L_{\mathrm{p4}}) \tag{3.10}$$

Solving Eqns. 3.8, 3.9 and 3.10, the capacity of wall is obtained as follows:

$$\begin{aligned} F_{\mathrm{R}}^{\mathrm{RM}} &= \frac{L}{h_1}\left\{ F_{\mathrm{v}} + w_{\mathrm{d}} + F_{\mathrm{p}} \frac{(L_{\mathrm{p1}} + L_{\mathrm{p2}} + L_{\mathrm{p3}} + L_{\mathrm{p4}})}{L} \right\} \\ F_{\mathrm{R}}^{\mathrm{URM}} &= \frac{L}{h_1}\left(F_{\mathrm{v}} + w_{\mathrm{d}} \right) \end{aligned} \tag{3.11}$$

Here, we consider the capacity only after diagonal cracking, i.e., contribution of shear strength parameters Q_{v} and Q_{h} as shown in Fig. 3.11(b) has not been taken into account in the above strength formulation.

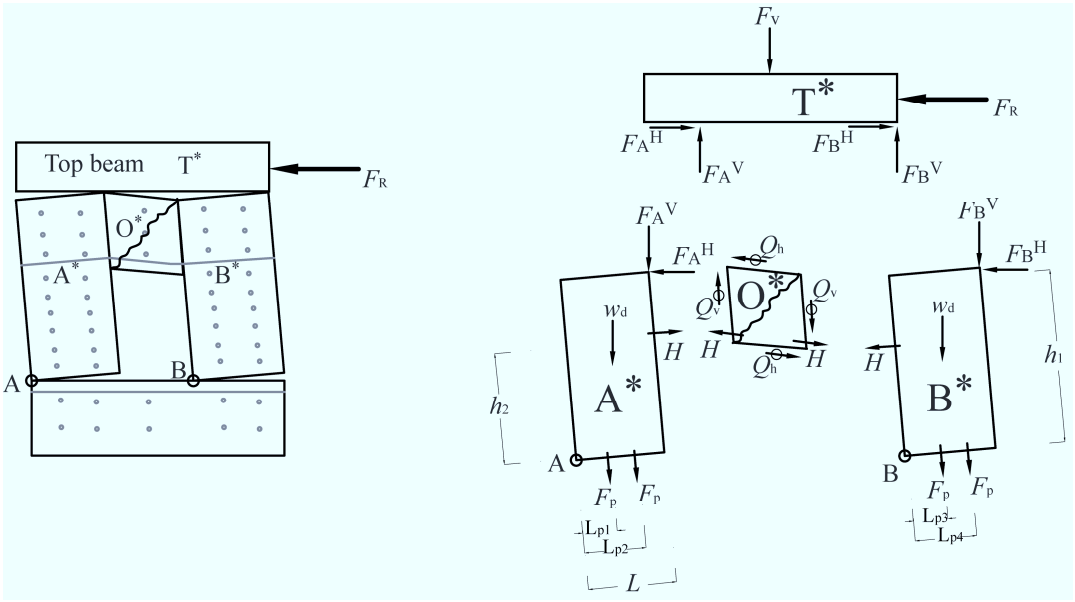

Figure 3.11: Weak beam-strong pier failure mechanism for RM specimen (a) Deformed shape, (b) Free body diagrams.

3.3.4.2 Strong beam-weak pier mechanism

From Fig. 3.12, with strong beam-weak pier failure mechanism, following equilibrium conditions for RM specimen can be obtained:

From free body O*:

$$\begin{aligned} F_R &= F_A^H + F_B^H \\ F_v + w_0 + 4F_p &= F_A^v + F_B^v \end{aligned} \tag{3.12}$$

From free body A*:

$$F_A^H h_2 = F_A^v L + w_d L/2 \tag{3.13}$$

From free body B*:

$$F_B^H h_2 = F_B^v L + w_d L/2 \tag{3.14}$$

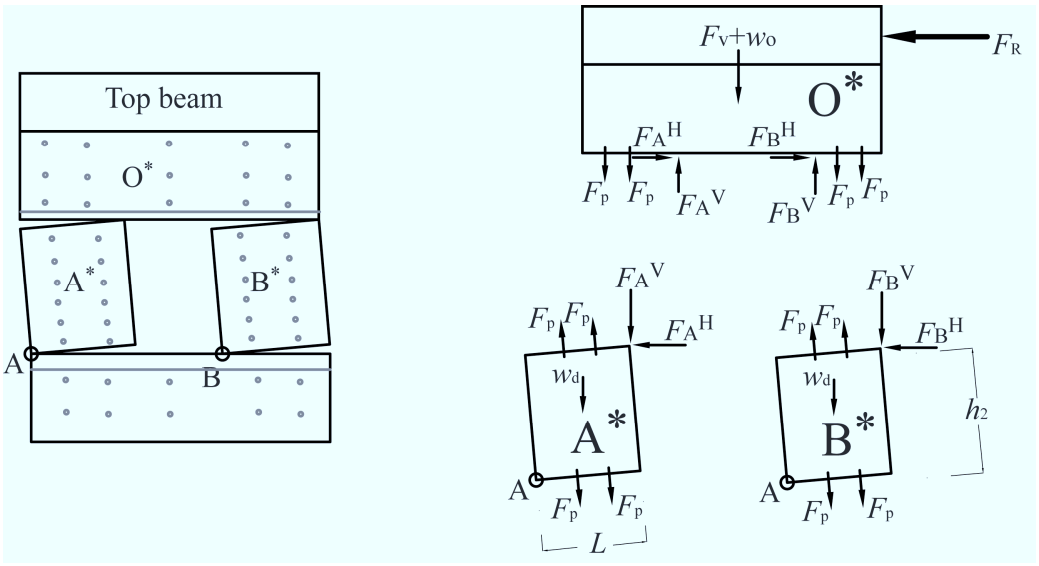

(a) (b)

Figure 3.12: Weak pier-strong beam failure mechanism for RM specimen (a) Deformed shape, (b) Free body diagrams.

Solving Eqns. 3.12, 3.13 and 3.14, the capacity of wall is obtained as follows:

$$F_{\mathrm{R}}^{\mathrm{RM}} = \frac{L}{h_2}\left(F_{\mathrm{v}} + w_0 + w_{\mathrm{d}} + 4F_{\mathrm{p}}\right)$$
$$F_{\mathrm{R}}^{\mathrm{URM}} = \frac{L}{h_2}\left(F_{\mathrm{v}} + w_0 + w_{\mathrm{d}}\right) \tag{3.15}$$

The failure mechanisms and subsequently the resisting force computed using Eqns. 3.11 and 3.15 give two extreme upper and lower bound values. However, the actual failure pattern and resisting force observed experimentally is generally between these two cases. Theoretical prediction made on the basis of experimentally observed final failure pattern has been shown in later sections of this paper with large deformation results.

3.3.5 RESULTS AND DISCUSSION

3.3.5.1 URM Specimen

Summary of experimental observations

Experimental cyclic loading history is shown in Fig. 3.13 where response for maximum rotation angle up to θ_{max} <1/400 radian is presented. A maximum load of 30.2 kN was observed at the very small rotation angle just before cracking. After cracking was initiated, brittle failure occurred with an almost constant residual force of about 20 kN. Here the pre-cracking response remained almost linear until peak force was observed and post-cracking mode is dominated by the sudden drop in resisting force due to brittle failure. An almost constant resisting force was observed thereafter corresponding to the wall's shear and rocking resistance. The presence of opening governed the failure mechanism with diagonal shear cracking originating from the extreme edges of opening and finally causing rocking of piers as shown by the dotted lines in Fig. 3.14(a).

Comparison with numerical simulation

Comparison is made between experimental and numerical response in Fig. 3.13 within the small rotation angle up to θ_{max} <1/400 radian. The numerically computed and experimentally observed resisting forces agree well with each other. Numerical response also shows similar pre-cracking response with almost linear behavior up to initial peak strength. With the completion of pre-cracking, the specimen in the immediate post-cracking stage shows significant wall deformation with no real increase in resisting force with good agreement between the FE and experimental results. Fig. 3.14(b) shows the FE deformed shape for URM specimen at deformation angle of θ_{max} =1/1200 radian which reflects the instant when maximum horizontal resisting force is observed. The contour of color in Fig. 3.14(b) represents the distribution of principal tensile and compressive stresses in FE model.

Comparison with theoretical predictions

Comparisons have been made with two extreme cases – strong pier-weak beam and strong beam-weak pier mechanisms as described previously in Section 3.3.4. For strong pier-weak beam mechanism, using Eqn. 3.11 with L (=650 mm) the width of pier, h_1 (=1330 mm) the height of reaction force from the point of rotation, F_v (=20 kN) the vertical load applied at the top of the specimen and w_d (=5.5 kN) the weight of pier, horizontal resisting force F_R^{URM} of 12.46 kN is obtained. The mechanism underestimates the resistance offered by masonry wall as shown in Fig. 3.13.

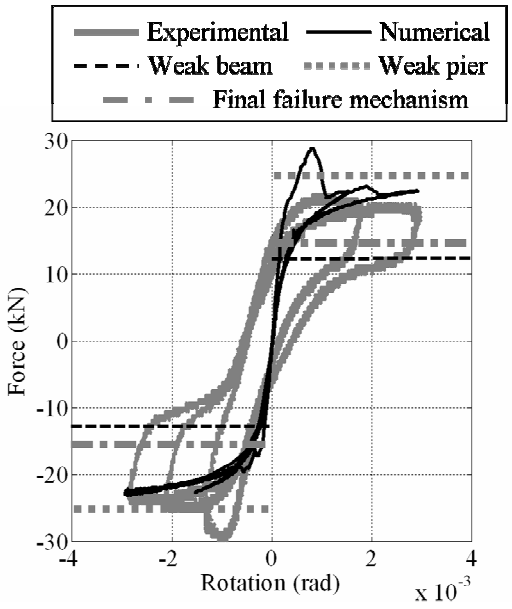

Figure 3.13: Force deformation comparison for URM specimen for θ_{max} <1/400 radian.

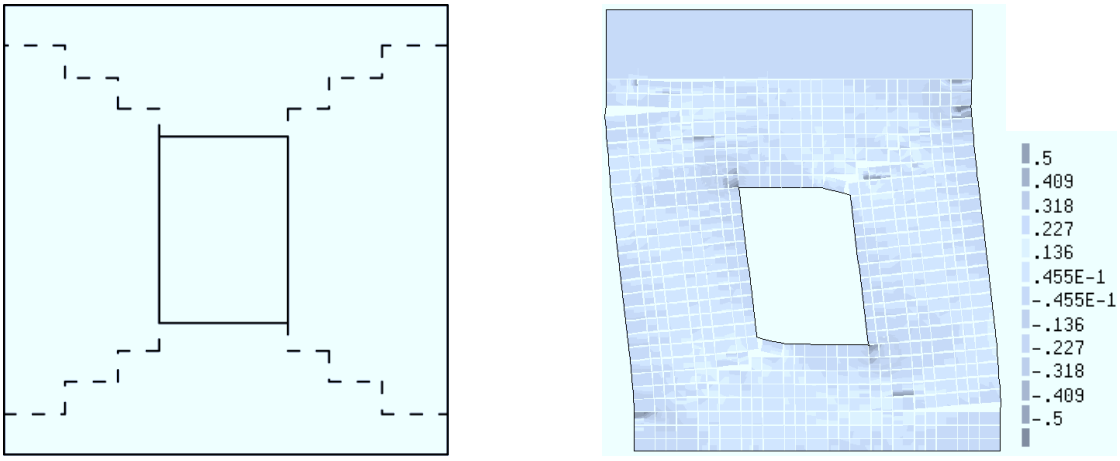

(a) (b)

Figure 3.14: Deformed shapes for URM specimen (a) Experimentally observed for θ_{max} <1/400 radian, (b) Numerical simulation for θ_{max} <1/1200 radian.

For strong beam-weak pier mechanism, the resisting force F_R^{URM} of 24.83 kN is obtained from Eqn. 3.15 which overestimates the experimental response as shown in Fig. 3.13. Here h_2 (=780 mm), w_0 (=6.55 kN) and w_d (=3.25 kN) are taken for computation. w_0 is the weight of brick wall resting on the rocking pier. Additionally, prediction based on the final failure pattern has also been done with failure pattern and subsequent formulation given below in Eqn. 3.16. The resisting force computed from final failure mechanism gives value of 14.4 kN which again underestimates the experimental response as shown in Fig. 3.13. Although the reason for this comparatively lower value of resisting force is unclear, friction is one possible reason.

The final failure pattern observed experimentally as shown in Fig. 3.15(a) showed wide diagonal shear cracks with rocking of a single pier. The horizontal resisting force of URM specimen is compared to the rocking resistance computed by the rigid-body assumption as shown in Fig. 3.15(b). From Fig. 3.15(b), equilibrium condition gives following expression:

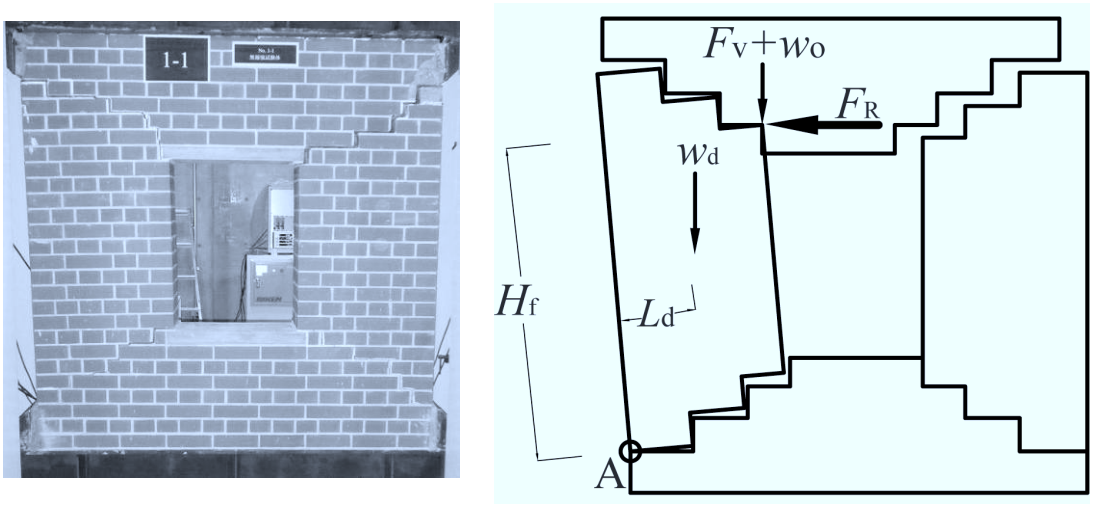

(a) (b)

Figure 3.15: Final failure mechanisms for URM specimen: (a) Experimentally observed at θ_{max} =+0.02 radian, (b) Theoretical prediction.

$$\text{Point A,}\quad F_R = \frac{w_d L_d + (F_v + w_o)L}{H_f} \tag{3.16}$$

L (=650 mm) is pier width, H_f (=1190 mm) the height of the reaction force from the point of rotation, w_d (=5 kN) the weight of the rocking pier, F_v (=20 kN) the load applied at the top of specimen, w_o (=4 kN) the weight of brick wall resting on the rocking pier, L_d (=303mm) the distance of centre of mass for rocking piers. The rocking capacity of URM specimen, F_R^{URM} calculated using Eqn. 3.16 is 14.4 kN.

3.3.5.2 RM Specimen

Summary of experimental observations

Fig. 3.16(a) shows the relationship of resisting force and the rotation angle for RM specimen for small deformation range of θ_{max} <1/200 radian. In contrary to URM specimen response, RM specimen showed higher resisting force and ductility without sudden decrement in strength, showing the effectiveness of reinforcing bars inserted. In addition to force deformation history, strains experienced by the reinforcing bar at two primary locations are shown in Figs. 3.17(a) and (b). Fig. 3.17(a) shows strain history

for the bar inserted at an angle of π/4 radian perpendicular to the plane of wall shown by Strain 1 in Fig. 3.6 and Fig. 3.17(b) is for horizontally inserted bar; its location represented as Strain 2 in Fig. 3.6. Note that strain gage history has been plotted for small deformation range of θ_{max} <1/200 radian, representing the instant when inclined inserted reinforcing bar just started yielding. The strain gage history shows clearly effectiveness of both inclined as well as horizontal inserted bars in providing resistance to shear failure of masonry walls. The failure mechanism observed is shown in Fig. 3.16(b) with mix failure mechanism. Diagonal shear failure observed for URM specimen was prevented for RM specimen.

Comparison with numerical simulation

Comparison is made between experimental and numerical response in Fig. 3.16(a), in terms of force deformation history within the small rotation angle up to θ_{max} <1/200 radian. Comparisons between strain gage histories are shown in Figs. 3.17(a) and (b). Resisting force observed experimentally was slightly lower as compared to numerically computed value. The reason is complex and mixed failure mechanism observed during experimentation; there was significant damage in masonry at top portion of wall specimen which was not seen in case of numerical simulation. It should be noted that reinforcing bar just started to yield at this deformation range, hence no significant energy dissipation in case of numerical results. Good agreements were found for strain gage histories both for Strain 1 as well as Strain 2. The location of Strain 1 and Strain 2 in case of numerical model is shown in Fig. 3.8. The numerical model also showed the effectiveness of both inclined inserted as well as horizontally inserted reinforcing bar in in-plane shear strength enhancement of masonry walls with openings. Stress concentration at the extreme edges of opening, causing diagonal shear cracking of URM specimen, was prevented for RM specimen with cracks distributed uniformly showing evenly distributed load sharing for RM specimen. It should be noted that noise for the strain gage data obtained for Strain 2 persisted even at very

small deformation load steps with maximum step size kept at 1/1000th of maximum deformation angle. The FE deformed shapes at different loading instants are shown in Fig. 3.18. The contour of color in Fig. 3.18 represents the distribution of principal tensile and compressive stresses in FE model.

Comparison with theoretical predictions

As explained in Section 3.3.4, theoretical predictions have been made assuming two extreme cases – strong pier-weak beam and strong beam-weak pier mechanisms. For strong pier-weak beam mechanism as shown in Fig. 3.11, using Eqn. 3.11 with F_p (=16.66 kN) the strength of inclined inserted reinforcing bar, L_{p1} (=330 mm), L_{p2} (=550 mm), L_{p3} (=110 mm), L_{p4} (=440 mm) the distances of inclined inserted reinforcing bars from point of rotation, w_d (=5.5 kN) the weight of pier, the calculated value of horizontal resisting force F_R^{RM} is 30.37 kN. The predicted strength slightly underestimates the resistance offered by masonry wall as shown in Fig. 3.16(a).

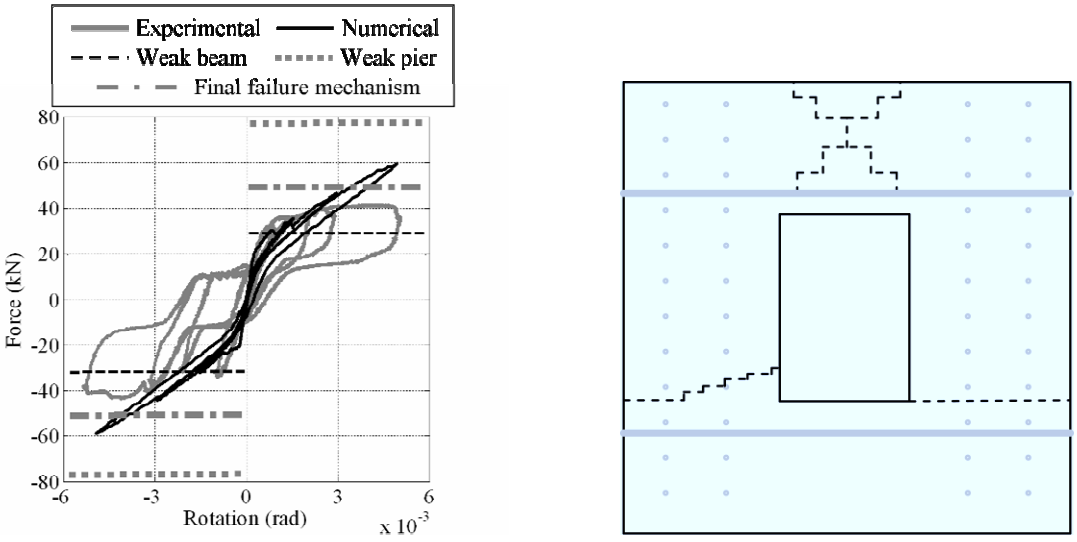

(a) *(b)*

Figure 3.16: Response for RM specimen for θ_{max} <1/200 radian (a) Force deformation comparison, (b) Experimentally observed cracking pattern.

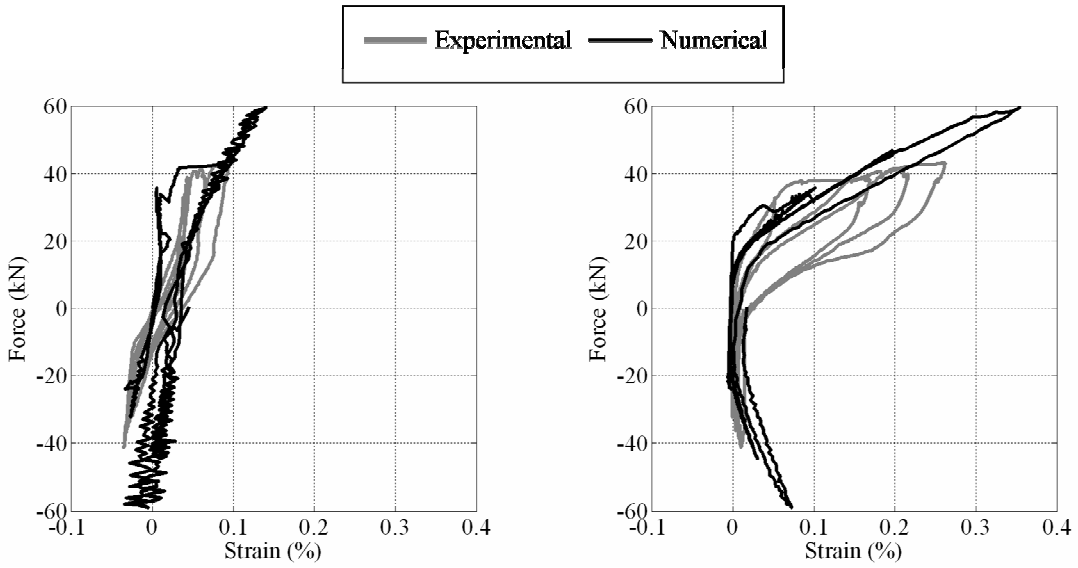

Figure 3.17: Strain gage history comparison for RM specimen (a) Strain 2, (b) Strain 1.

Strong beam-weak pier mechanism assumes failure mechanism as shown in Fig. 3.12. Using Eqn. 3.15, the resisting force F_R^{RM} of 80.36 kN is obtained, which clearly overestimates the experimental response as shown in Fig. 3.16(a). Here, w_0 (=6.55 kN) and w_d (=3.25 kN) are taken for computation. An additional plot has been made in Fig. 3.16(a) with prediction based on the final failure pattern and subsequent formulation as given below. The mix failure mechanism, observed experimentally given in Eqn. 3.20, predicts more closely the experimentally observed resisting force.

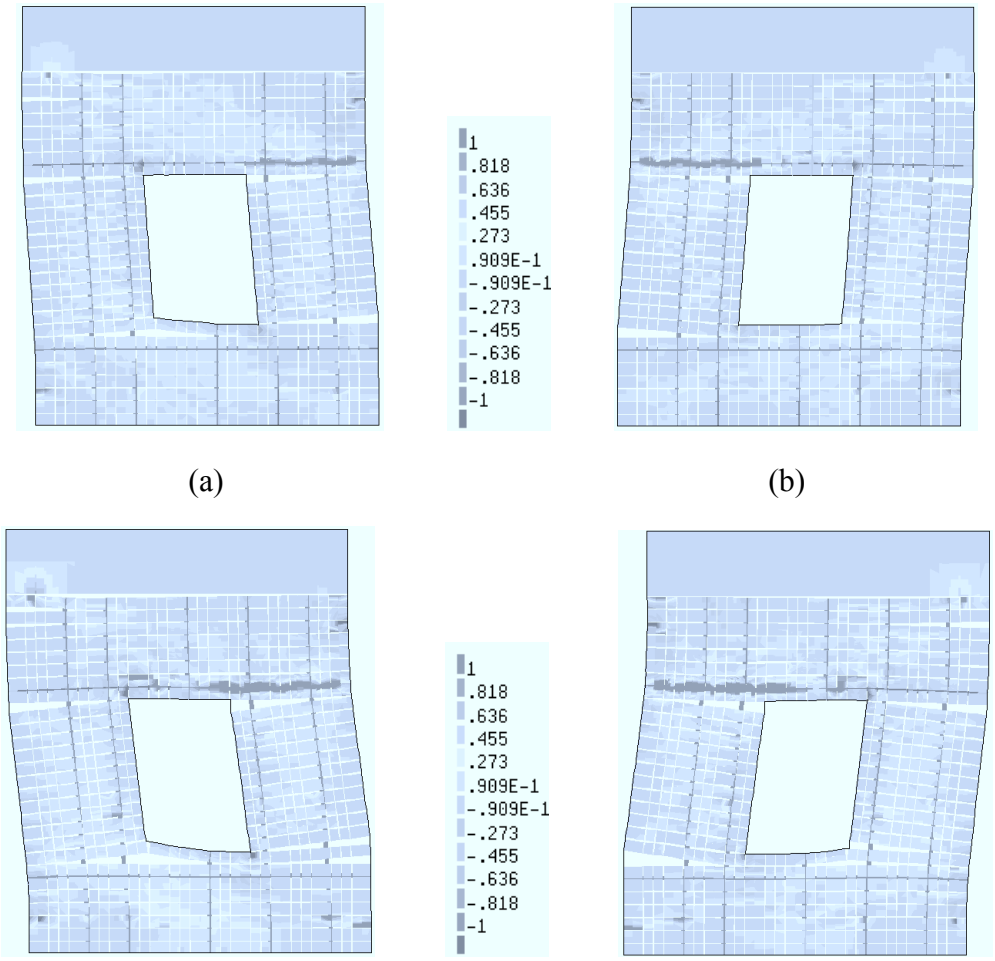

Figure 3.18: Deformed shape for RM specimen at (a) θ_{max} =+0.003 radian, (b) θ_{max} =-0.003 radian, (c) θ_{max} =+0.005 radian, (d) θ_{max} =-0.005 radian (Deformation scale = 20).

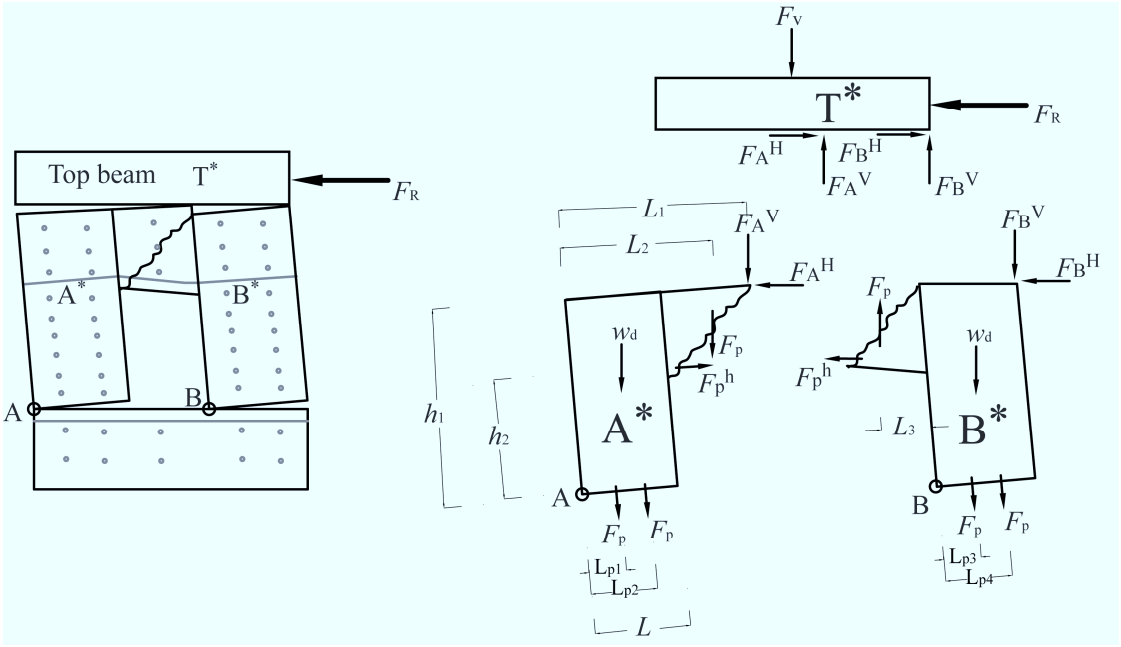

(a) (b)

Figure 3.19: Experimentally observed final failure mechanism for RM specimen (a) Deformed shape, (b) Free body diagrams.

From Fig. 3.19, with mix failure mechanism representing the final cracking pattern observed experimentally, following equilibrium conditions for RM specimen can be obtained:

From free body T*:

$$\begin{aligned} F_R &= F_A^H + F_B^H \\ F_v &= F_A^v + F_B^v \end{aligned} \tag{3.17}$$

From free body A*:

$$F_A^H h_1 = F_A^v L_1 + w_d L/2 + F_p^h h_2 + F_p L_2 + F_p(L_{p1} + L_{p2}) \tag{3.18}$$

From free body B*:

$$F_B^H h_1 = F_B^v L + w_d L/2 - F_p^h h_2 + F_p L_3 + F_p(L_{p3} + L_{p4}) \tag{3.19}$$

Solving Eqns. 3.17, 3.18 and 3.19, the capacity of wall is obtained as follows:

$$F_{\mathrm{R}}^{\mathrm{RM}} = \frac{L}{h_1}\left\{ F_{\mathrm{A}}^{\mathrm{v}} \frac{L_1}{L} + F_{\mathrm{B}}^{\mathrm{v}} + w_{\mathrm{d}} + F_{\mathrm{p}} \frac{(L_2 + L_3 + L_{\mathrm{p1}} + L_{\mathrm{p2}} + L_{\mathrm{p3}} + L_{\mathrm{p4}})}{L} \right\} \qquad (3.20)$$

Here, L_2 (=930 mm), L_3 (=280 mm), w_{d} (=6 kN), h_1 (=1330 mm). Assuming $F_{\mathrm{A}}^{\mathrm{v}} = F_{\mathrm{B}}^{\mathrm{v}} = F_{\mathrm{v}}/2$, the rocking capacity of RM specimen, $F_{\mathrm{R}}^{\mathrm{RM}}$ calculated using Eqn. 3.20 is 49.9 kN.

3.3.5.3 Discussion

Both the experimental observations and numerical simulations showed effectiveness of the pinning retrofitting technique for in-plane shear loaded masonry walls. Retrofitted masonry walls showed sufficient strength enhancement that can avoid brittle collapse during earthquake excitation.

The resisting force computed for FE results and theoretical predictions matched well with each other. The FE result was moderately located between the two extreme theoretical estimations of weak beam and weak pier. Comparison of results for experimental observation and numerical simulation showed that FE prediction slightly overestimated the resisting force value. Bond slip of reinforcing bar might have influenced the failure mechanism during the tests, however, numerically developed model assumed a perfect bond between the reinforcing bars and masonry elements. This could be one of the reasons for overestimation of strength by numerical models. Failure pattern observed experimentally for RM specimen was wide spread with extensive cracking at the top mortar joint between the top steel beam and wall specimen with rocking of piers representing mix failure mechanism which neither belonged to weak beam nor weak pier mode of failure. FE simulation for similar test set-up did show wide cracks at the top mortar joint similar to experimental observation but the response was largely dominated by failure mechanism closer to weak pier mode of failure with relatively stronger upper portion. This could also have resulted in

overestimation of the resisting force. Hence, numerical model is particularly applicable for specific case of perfect bond between reinforcing bars and masonry elements. Nevertheless, the numerical results, with sufficient exactness, provided a strong basis for strength prediction as well as defining possible locations of stress concentrations and stated the effectiveness of retrofitted specimen with both inclined and horizontally inserted reinforcing bars.

3.4 FINITE ELEMENT MODELING OF OUT-OF-PLANE LOADED MASONRY WALL

3.4.1 Masonry wall specimen

Masonry wall specimens involved in this particular study [9] are given in Figs. 3.20 and 3.21. The inclined stainless steel bars are inserted into brick walls diagonally from mortar joints on the plane perpendicular to the wall, as shown in Fig. 3.20. Circles indicate the front from where bars are inserted. Solid and dotted lines are bars inserted in wall specimens RM1 and RM2, which differ only in the number of bars inserted. Ref. [6] reported that specimen RM2 showed better response without substantially decrementing resisting force. Specimen RM1, with fewer bars used, sharply decremented resisting force after the crack at the first bed joint was initiated. Specimen RM2 requires more reinforcing bars, so it costs more than specimen RM1.

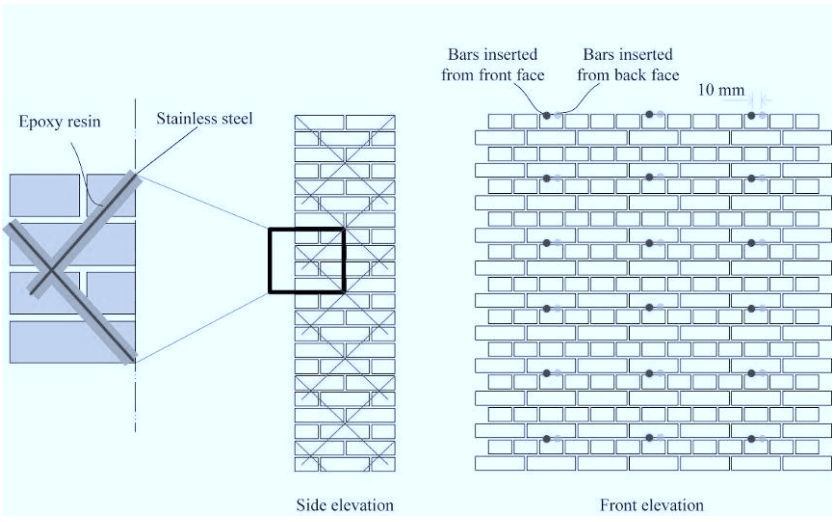

Figure 3.20: Specimen RM1 reinforcing bar locations.

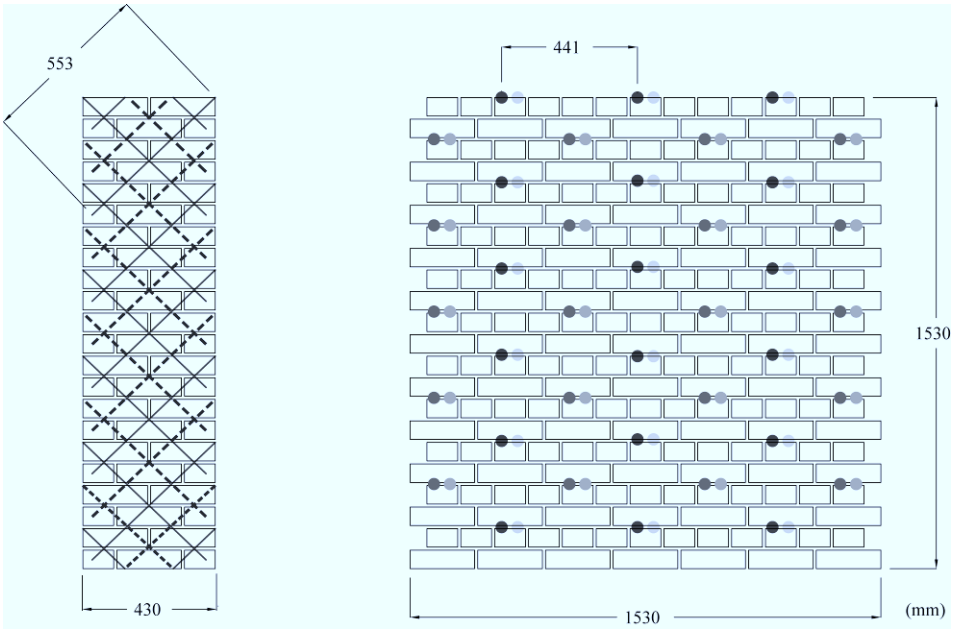

Figure 3.21: Specimen RM2 reinforcing bar locations.

3.4.2 Masonry wall FE model

The brick unit and mortar joint model adopted in FE modeling is similar to the one described in preceding section for in-plane shear loaded wall in Section 3.3.2 with similar constitutive model adopted. Here potential cracks in the brick units have not been modeled to keep the modeling simple and additionally during the experimental observation, cracks predominantly concentrated at mortar joints were observed. An FE model with meshing for a brick unit is shown in Fig. 3.22.

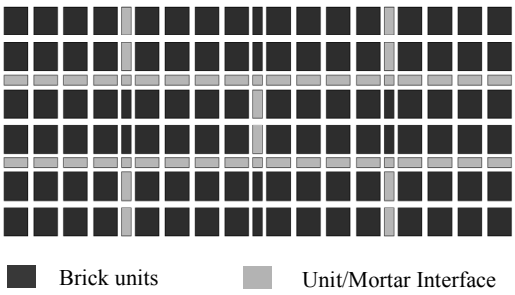

Figure 3.22: Masonry unit and unit/mortar interface discretization.

Properties of brick units adopted were similar to former (Section 3.3.2). Mortar joint properties were however different to the one used for in-plane loaded specimens. Gap arises if tensile traction normal to the interface exceeds tensile strength of 0.61 MPa. Tests on shear triplets [10] determined shear parameters to be c=0.67 MPa and tanφ=1.1. The dilatancy angle is tanψ=0.6 [16]. Normal stiffness D_{11}=30 N/mm^3 and shear stiffness D_{22}= 13 N/mm^3 are used for the unit/mortar interface similar to former.

Inclined bar model

A stainless steel bar is presented by a two-node truss element with material properties represented by elastic perfectly plastic properties adopting Young's modulus for steel E_{st}=200 GPa and yield stress f_y = 667 MPa -- material constants obtained from tensile tests on steel bar specimens 6 mm in diameter.

Pull-out tests showed the bond between the reinforcing bar and masonry elements to be stronger than that of the reinforcing bar, so both ends of each truss element were connected to corresponding nodes of continuum elements representing bricks, as shown in Fig. 3.23 RM1 and RM2 where, circles at both ends of inclined lines indicate nodes where truss and continuum elements are connected. No relative displacement was allowed between truss element end nodes and corresponding continuum element nodes.

The bending resistance of reinforcing bars could be argued as significant and beam elements used to model reinforcing bars instead of truss elements. We used truss elements, however, simply to keep the FE model as simple as possible. The validity of truss element use is discussed in Results Section.

Equivalent vertical bar model

The simplified FE model proposed to stabilize analysis and to reduce the

computational burden uses an equivalent vertical bar to represent inclined reinforcing bars, as shown in Fig. 3.23, where the equivalent vertical bar model for specimen RM1 is $RM1^{eq}$ and that for specimen RM2 is $RM2^{eq}$. Equivalent vertical bars for $RM1^{eq}$ and $RM2^{eq}$ are shown by thick solid lines. In the simplified FE models, the equivalent vertical bars are also represented by truss elements. Circles show nodes where truss and continuum elements are connected.

To determine the equivalent vertical bar cross-sectional area, we count minimum number n of steel bars at the wall's critical section. As shown in Fig. 3.20, specimen RM1 has 6(=3x2) lines of reinforcement, i.e., at least 6 reinforcing bars at any horizontal wall section. Specimen RM2 similarly has at least 14 reinforcing bars at any horizontal section, as shown in Fig. 3.21, so n is 6 for specimen RM1 and 14 for specimen RM2. Bars are inclined at a $\pi/4$ radian to the vertical axis, so cross-sectional area $A_{\text{bar}}^{\text{eq}}$ of the equivalent vertical bar is computed as $A_{\text{bar}}^{\text{eq}} = nA_{\text{bar}}\cos(\pi/4)$. A_{bar} is the cross-sectional area of each stainless steel bar.

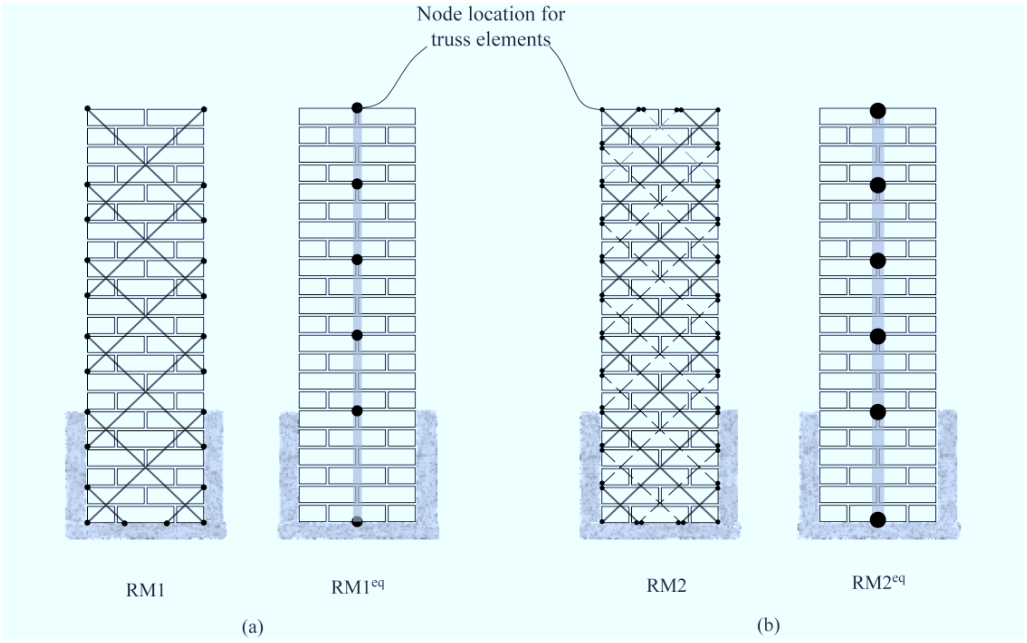

Figure 3.23: Simplified FE modeling specimens (a) RM1, (b) RM2.

3.4.3 Loading condition

The test setup in Fig. 3.24 has the out-of-plane load coming at the top of wall, making it fail in cantilever action. Monotonic loading was applied to the URM specimen and both RM specimens subjected to quasi-static cyclic loading. A displacement-controlled cyclic load was provided by two hydraulic jacks to make maximum rotation angle θ_{max} of the wall specimen equal to ±0.0025, ±0.05, ±0.01, ±0.015, ±0.02, and ±0.03 radian.

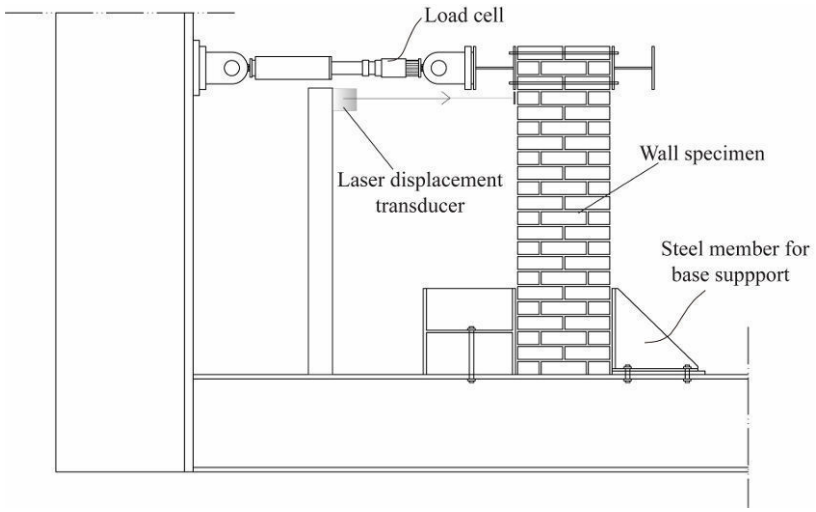

Figure 3.24: Experimental test setup for out-of-plane cyclic loading.

3.4.4 Results and Discussion

3.4.4.1 URM Specimen

A maximum load of 32.2 kN was observed at the very small rotation angle just before cracking. After cracking was initiated, brittle failure occurred with an almost constant residual force of 3.5 kN as the rotation angle increased. The numerically obtained relationship between horizontal resisting force and the rotation angle for the URM specimen is shown in Fig. 3.25**,** where the response up to the maximum rotation angle θ_{max} <0.015 radian presented the pre- and post-cracking responses. The pre-cracking response remained almost linear until peak force was observed. At the

peak, the first crack formed at the mortar joint immediately above the base support. Peak force represents strength associated with bed mortar joint tensile cracking. Post-cracking mode is dominated by the sudden drop in resisting force due to brittle failure. An almost constant resisting force was observed thereafter corresponding to the wall's rocking resistance.

Theoretically, wall rocking resistance is computed assuming a rigid body. The horizontal resistance capacity, assuming that the wall was pre-cracked at the bed joint immediately above the base support, is given by

$$F_{\mathrm{C}}^{\mathrm{U}} = \frac{mgt}{2h} \tag{3.21}$$

t is wall thickness, h the height of the reaction force from the bed mortar joint immediately above the base support, m the mass of the wall specimen above the base support, and g gravity acceleration. As shown in Fig. 3.25, theoretical rocking resistance, computed at 2.65 kN from Eqn. 3.21 and shown by the dotted line, effectively predicts post-cracking resisting force observed both experimentally and numerically.

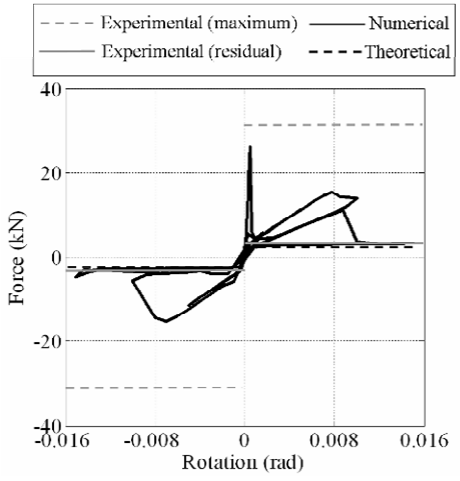

Figure 3.25: Specimen URM response comparison.

3.4.4.2. RM Specimens

Figs. 3.26 and 3.27 show the relationship of resisting force and the rotation angle for specimens RM1 and RM2. FE results include those for both inclined bar models RM1 and RM2 and equivalent vertical bar models $RM1^{eq}$ and $RM2^{eq}$.

Comparison with experiments

Comparison is made between experimental and numerical response. Similar to the URM specimen, the horizontal force-rotation angle relationship features two distinct stages -- (1) pre-cracking and (2) post-cracking. Figs. 3.26(a) and 3.27(a) show the response of specimens within the small rotation angle up to θ_{max} <0.015 radian, with peak horizontal resisting force corresponding to bed joint tensile strength. With the completion of pre-cracking, the specimen in the immediate post-cracking stage shows significant wall deformation with no real increase in resisting force. The large difference between uncracked and cracked wall stiffness decreases the resisting force measured. In the post-cracking phase shown in Figs. 3.26(b) and 3.27(b), the numerical results for both FE models predict experimental observation comparatively well, especially in the post-cracking phase. The good agreement between the FE and experimental results shows that the bending resistance of reinforcing bars is negligible, confirming the efficacy of using truss elements.

Comparison with theoretical prediction

The post-cracking responses of RM specimens are compared to the rocking resistance computed by the rigid-body assumption. The capacity from rigid body rotation, assuming that the wall cracked at the bed joint above the base support, is as follows:

$$F_C^{RM} = t\frac{mg + nF_p\cos(\pi/4)}{2h} \tag{3.22}$$

F_p is reinforcing stainless steel bar strength and n the number of effective stainless steel bars at the critical (cracked) section. For specimen RM1, n is 6, and for specimen

RM2 14 as explained in Section 3.2.2. F_p is calculated assuming stainless steel bar strength to be 667 MPa and the equivalent sectional area assumed to be 5 mm in diameter to incorporate the threading effect. The rocking capacity of specimen RM1 is 14.03 kN, and that of specimen RM2 29.2 kN -- values agreeing well with residual resisting force observed experimentally and numerically.

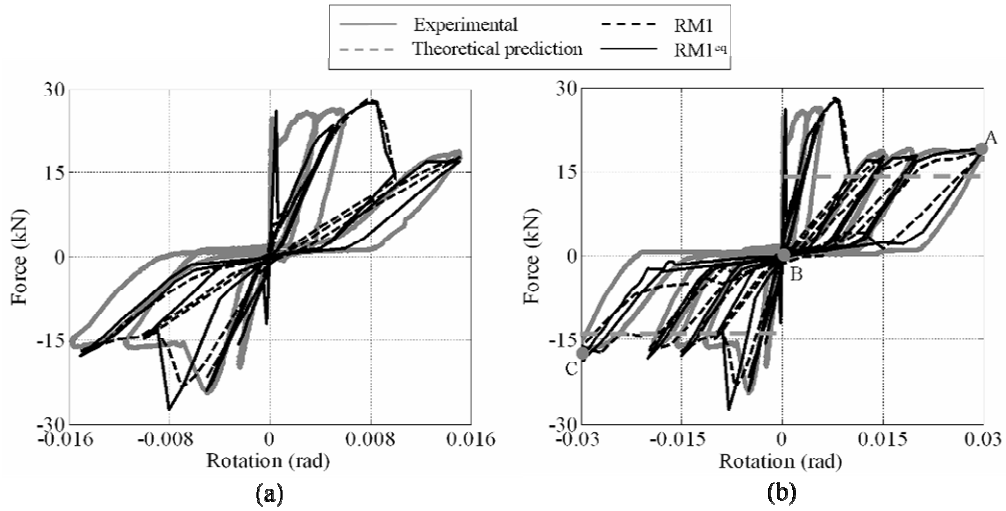

Figure 3.26: Specimen RM1 comparison (a) Force-rotation relation for θ_{max} <0.015, (b) Force-rotation relation for θ_{max} >0.015.

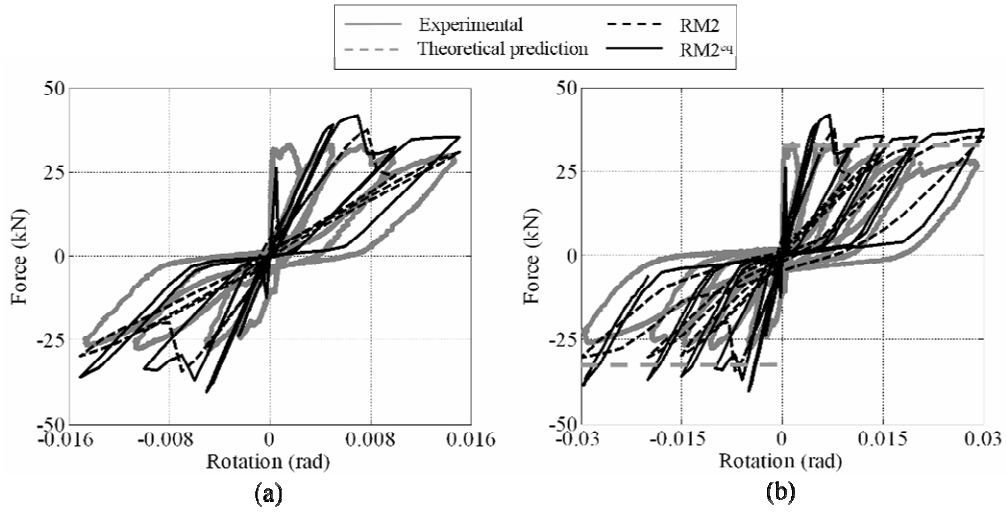

Figure 3.27: Specimen RM2 comparison (a) Force-rotation relation for θ_{max} <0.015, (b) Force-rotation relation for θ_{max} >0.015.

Comparison between inclined and vertical bar models

Equivalent vertical bar models $RM1^{eq}$ and $RM2^{eq}$ effectively represent cyclic behavior observed experimentally. This equivalent vertical bar approach is numerically robust and requires less computational time -- about half that required for inclined bar models RM1 and RM2. Although equivalent vertical bar models tend to slightly underestimate energy dissipation in negative cycles compared to inclined bar models, the difference is insignificant. Unloading stiffness by $RM1^{eq}$ and $RM2^{eq}$ agreed better with experimental results than that by RM1 and RM2, possibly due to the difference in length between nodes of truss elements connected to continuum elements. As shown in Fig. 3.23, the equivalent vertical bar model was about half as long as that for the inclined bar model. Note that a trial-and-error approach was required in determining these lengths because of the trade-off between convergence difficulty and agreement with experimental results.

Pinching phenomena

A pinching phenomenon characterized by reduced stiffness and strength under cyclic loading and common to this type of reinforcement, appears in both FE and experimental results. This phenomenon is not unique to our present reinforcing technique and is also seen in masonry walls reinforced using vertical steel bars [19].

Fig. 3.28 shows FE simulation of the pinching mechanism observed during the last loading history cycle of specimen RM1. The three loading instants in Fig. 3.26(b) are loading up to point A (θ=0.03 radian), unloading up to point B (θ=0 radian), and reverse loading up to point C (θ=-0.03 radian). Point A shows the instant of maximum rotation angle for the specimen with reinforcing bars stretched inelastically as shown in Fig. 3.28(a). Upon load reversal, the wall's compression face is relieved at fully cracked section stiffness, no longer having mechanical stiffness at the cracked joint except flexural stiffness of the reinforcing bar as seen in the deformation in Fig.

3.28(b). This is attributed to the pinching phenomenon observed for the specimen at point B. This zero stiffness lasted until contact with the opposite wall face, after which the specimen retained mechanical stiffness corresponding to the fully cracked section up to point C, where reinforcing bars stretched inelastically as shown in Fig. 3.28(c). The mechanism during the loading history was governed mainly by plastic deformation of reinforcing bars at the cracked section. Pinching and cracking mechanisms observed for Specimen RM2 resemble that above for specimen RM1.

3.4.5 Sensitivity analysis

We studied the sensitivity of masonry material properties or, more importantly, mechanical mortar properties, to determine reinforcing technique robustness, taking into account the four material parameters of the mortar joint -- tensile strength f_t', cohesion c', tangent of friction angle tanφ', and normal and shear stiffness D_{11}' and D_{22}' -- using numerical models representing URM and RM1^{eq} as baselines for comparison. RM1^{eq} is used simply because it is more stable and requires less computational time than other FE models. Strength parameters are varied one at a time to lower and higher values.

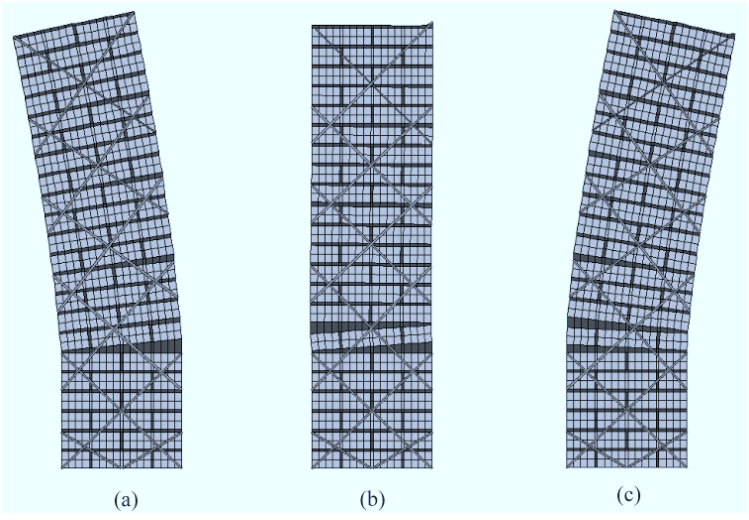

Figure 3.28: Specimen RM1 loading history mechanism with deformed shapes: (a) θ =0.03 radian (Deformation scale, DS = 5), (b) θ =0 radian (DS = 10), (c) θ =-0.03 radian (DS = 5).

Table 3.3 shows parameters controlling the parametric study with corresponding IDs. A variation of ±25% was made for all parameters. To keep the same shear strength of a material under the initial normal stress when the tensile strength, f_t', is varied, the value of tanφ' is adjusted accordingly. The baseline for all parameters was shown in preceding sections. To quantify the influence of individual parameters on structural response, four response quantities were selected to characterize the force-deformation relation as shown in Fig. 3.29 -- initial stiffness K_{ini}, initial peak strength F_{ini}, post-cracking stiffness K_{res}, and residual horizontal force F_{res}. The change in response quantities is assessed in the change in the corresponding response for the changed parameter value for that at the baseline.

Figs. 3.30(a) and (b) clearly show changes in structural response for F_{ini} and K_{ini} in tensile strength f_t and stiffnesses D_{11} and D_{22} of the unit/mortar interface. Such dependencies of structural responses are usual prior to cracking because tensile strength and stiffness parameters mainly control behavior in the pre-cracking phase. A similar pre-cracking response was observed in URM and RM1^{eq}, demonstrating the consistency of analysis results.

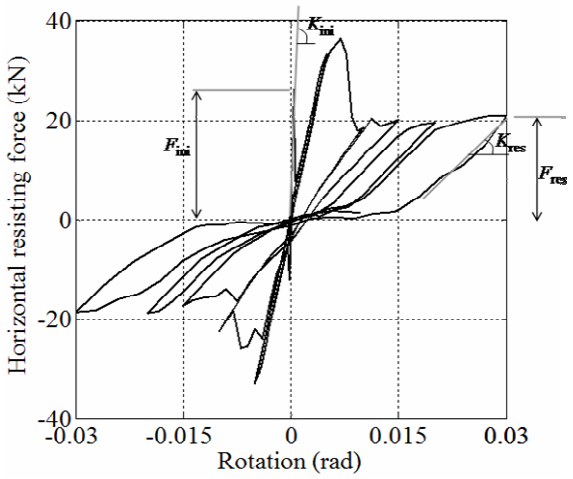

Figure 3.29: Response quantities characterizing the force-deformation relationship.

Table 3.3: Material parameter changes and corresponding sensitivity study IDs.

Parameter	f_t'		c'		tanφ'		D_{11}', D_{22}'	
ID	1	2	3	4	5	6	7	8
Change (%)	-25	+25	-25	+25	-25	+25	-25	+25

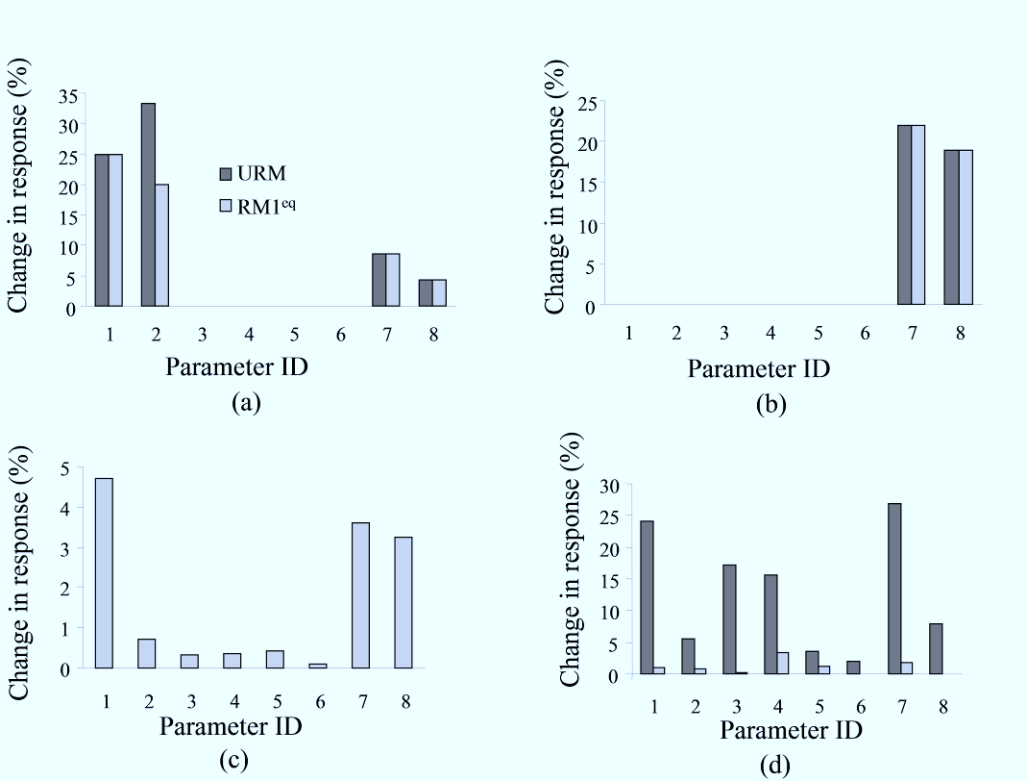

Figure 3.30: Structural response changes with corresponding material parameter changes: (a) initial peak strength, (b) initial stiffness, (c) post-cracking stiffness, (d) residual horizontal force.

The post-cracking response of specimens is shown in Figs. 3.30(c) and (d). Changes in post-cracking stiffness for the RM1^{eq} specimen showed the small variation in Fig. 3.30(c). Note that the effect of parameter variation on post-cracking stiffness of the URM specimen is not included in Fig. 3.30(c) because post-cracking stiffness is not affected by material parameters but by rocking resistance due to the specimen's weight. Changes in structural response in residual horizontal force for URM and RM1^{eq} clearly

differed with changes in material parameters. For the URM specimen with a parameter variation with ID 7 representing the change in stiffness properties, a 26% change is observed compared to the baseline specimen. For the $RM1^{eq}$ specimen, however, this variation was very minimal as shown in Fig. 3.30(d).

We concluded from sensitivity analysis that variations in mechanical properties of masonry materials do not significantly affect post-cracking response of RM models, demonstrating the robustness of our proposed reinforcing technique in variations in material constants of masonry units. Since these variations are usually very large in historical masonry structures, this becomes highly important when selecting the retrofitting technique in practice.

3.5 CONCLUSION

This chapter has presented a 2D FE modeling scheme and theoretical prediction formulation for assessing the nonlinear load-deformation behavior and failure mechanism of masonry walls reinforced by inserting inclined and horizontal steel bars when subjected to quasi-static cyclic in-plane shear loading and out-of-plane loading. FE models have been generated with simplified micro-modeling strategy, where bricks, mortar joints and reinforcing bars are represented by continuum elements, interface elements, and truss elements, respectively. A simplified FE model with equivalent vertical bars representing inclined inserted bars has been proposed. This concept of equivalent vertical bar allows simple theoretical prediction of wall strengths and makes a 2D FE modeling possible for the particular retrofitting technique. Additionally, the proposed equivalent vertical bar model provided better convergence under cyclic loading at expense of lesser computational time as compared to inclined bar model. An evaluation of numerical result sensitivity to modeling parameters using the simplified FE model showed almost no sensitivity to variations in masonry material constants in reinforced specimens, demonstrating the robustness of pinning retrofitting technique

under cyclic loading conditions and the stability of our proposed simplified FE modeling.

REFERENCES

[1] KARANTONI F. V. and FARDIS M. N. Effectiveness of seismic strengthening techniques for masonry buildings. *Journal of Structural Engineering*, ASCE, 118(4):1884-1902, 1992.

[2] ELGAWADY M. A., LESTUZZI P. and BADOUX M. A review of conventional seismic retrofitting techniques for URM. *Proc. of 13th International Brick and Block Masonry Conference*, Amsterdam, 2004.

[3] ABRAMS D., SMITH T., LYNCH J. and FRANKLIN S. Effectiveness of rehabilitation on seismic behavior of masonry piers. *Journal of Structural Engineering*, ASCE, 133(1):32-43, 2007.

[4] EHSANI M. R., SAADATMANESH H. and VELAZQUEZ-DIMAS J. I. Behavior of retrofitted URM walls under simulated earthquake loading. *Journal of Composites for Construction*, 3(3):134-142, 1999.

[5] WILLIS C. R., SERACINO R. and GRIFFITH M. C. Out-of-plane strength of brick masonry retrofitted with horizontal NSM CFRP strips. *Engineering Structures*, 32(2):547-555, 2010.

[6] TAKIYAMA N., NAGAE T., MAEDA H., KITAMURA M., YOSHIDA N. and ARAKI Y. Cyclic out-of-plane flexural behaviour of masonry walls rehabilitated by inserting steel pins. *Proc. Of the 14th WCEE*, Beijing, 2008. http://www.iitk.ac.in/nicee/wcee/article/14_S11-015.PDF (Last accessed date: January 19, 2011).

[7] YOSHIDA N., NAGAE T., MAEDA H., FUKUMOTO S., TAKIYAMA N., SHRESTHA K. C., IBARADA I. and ARAKI Y. Cyclic in-plane shear-flexural experiments of masonry walls with opening reinforced by inserting stainless pins: Part I and II. *Proc. of Annual Meeting of Architectural Institute of Japan*, C-2:963-964, 967-968, 2009 (In Japanese).

[8] SHRESTHA K.C., NAGAE T. AND ARAKI Y. Finite element study on pinning retrofitting technique of masonry walls with opening subjected to in-plane shear load. *Proc. of 7th International Conference Analytical Models and New Concepts in Concrete and Masonry Structures*, Krakow, 2011.

[9] SHRESTHA K. C., NAGAE T. and ARAKI Y. Finite element modeling of cyclic out-of-plane response of masonry walls retrofitted by inserting inclined stainless steel bars. *Journal of Disaster Research*, 6(1):36-43, 2011.

[10] *RILEM, RILEM Technical recommendations for the testing and use of construction materials*, Taylor & Francis, New York, 1994.

[11] *ASTM, Annual Book of ASTM Standards. Section Four, Construction, Volume 04.05, Chemical-Resistant Nonmetallic Materials; Vitrified Clay Pipe; Concrete Pipe; Fiber-Reinforced Cement Products; Mortars and Grouts; Masonry; Precast Concrete*, ASTM International, West Conshohocken, PA, 2007.

[12] MODENA C., VALUZZI M. R., TONGINI FOLLI T. and BINDA L. Design choices and intervention techniques for repairing and strengthening of the Monza cathedral bell-tower. *Construction and Building Materials*, 16:385-395, 2002.

[13] VALLUZI M. R., BINDA L. and MODENA C. Mechanical behaviour of historic masonry structures strengthened by bed joints structural repointing. *Construction and Buinding Materials*, 19:63-73, 2005.

[14] SCHULTZ A.E., HUTCHINSON R.S. and CHEOK G.. C. Seismic performance of masonry walls with bed joint reinforcement. *Proc. of Structural Engineers World Congress*, San Francisco, California, USA, 1998.

[15] GOUVEIA J. P. and LOURENCO P. B. Masonry shear walls subjected to cyclic loading: Influence of confinement and horizontal reinforcement. *Proc. Of tenth North American Masonry Conference*, St. Louis, Missouri, USA, 2007.

[16] LOURENCO P. B. and ROTS J. G. Multisurface interface model for analysis of masonry structures. *ASCE Journal of Engineering Mechanics.* 123(7):660-668, 1997.

[17] *DIANA. DIANA User's Manual Release 9.3*, TNO DIANA BV, Delft, 2008.

[18] ELSHAFIE H., HAMID A. and NASR E. Strength and stiffness of masonry shear walls with openings. *TMS Journal*, 20(1):49-60, 2002.

[19] BUTTON M. R., and MAYES R. L. Out-of-Plane Seismic Response of Reinforced Masonry Walls. *ASCE Journal of Structural Engineering*, 118(9):2495-2513, 1992.

4

APPLICABILITY OF POLYMER CEMENT PASTES (PCPs) AS BONDING AGENTS FOR PINNING RETROFIT OF MASONRY

4.1 GENERAL

Historical masonry constructions are vulnerable to earthquake excitations and hence require proper strengthening and retrofitting. Among various available retrofitting techniques [1-2], pinning retrofitting procedure practiced in Japan as reported in Chapter 3 has strong potential in masonry retrofitting since in addition to strength and ductility improvements, this technique also causes minimal change in original appearance of structure. Extensive experimental [3] and numerical [4,5] studies have been done to prove robustness of this pinning retrofitting technique in masonry

constructions. However retrofitting procedure involves use of epoxy resin for bonding between masonry and reinforcing bar and epoxy resin, being an organic adhesive, has got its limitations -- low fire resistance, higher cost and poor bond to wet surfaces.

Use of ordinary mortar as bonding agent in place of epoxy resin largely affects the workability environment. During pinning retrofitting, a professional mason would normally require an open time limit up to 10 minutes between the injection of mortar and insertion of reinforcing bar, but with an ordinary mortar as bonding agent, it is very difficult to insert reinforcing bar. As an alternative, use of polymer-cement paste (PCP) as bonding agent has been proposed in this study with investigation on comparison of bond strengths of various commercially available polymer based admixtures in brick masonry.

Mechanical properties of polymer-based cementitious bonding agents as PCP and polymer-cement mortar (PCM) have already been reported as highly superior over normal conventional mortar [6-9]. Latex-modified PCM provide an improved workability over normal cement mortar and also with increase in polymer-cement ratio, there is subsequent reduction in water-cement ratio, which ultimately contributes to strength development and drying shrinkage reduction. In hardened state PCM shows an improved water-proofness and improved bond strength over ordinary cement mortar which makes it a potential bonding material as PCP and PCM in masonry retrofitting.

Application of PCP in masonry requires another important consideration regarding check in workability. If applied as masonry in its normal state, water from PCP gets absorbed by masonry making the paste poor in workability. For this purpose, there is need for pretreatment of masonry to create a water penetration barrier film so that there is minimum effect on workability of PCP after insertion. The present study involves comparison on various impregnants as pretreatment agent and their effect on workability of PCP in masonry.

The use of PCM for repair and restoration purpose of masonry structures has been limited to its use more as surface coating over grid of reinforcing bars [10-11] on unreinforced masonry walls. In this present study, we have examined and compared the effectiveness of PCPs prepared from various commercially available polymer admixtures as bonding adhesive between reinforcing bar used for pinning and masonry considering the effect of pretreatment using impregnant.

This chapter involves report on extensive experimental works carried out beginning with workability and pull-out tests on PCPs as bonding agents in masonry [13]. These tests were followed by tests on masonry assemblages to check the response of PCPs used pinning retrofitted masonry specimens involving compression tests, shear tests and one-point bending tests [14]. Finally, the chapter concludes with simulation of experimental results using finite element (FE) tool to state the applicability of use of PCPs in pinning retrofit of masonry walls.

4.2 TEST PROGRAM FOR WORKABILITY AND PULL-OUT TESTS

4.2.1 Materials

Polymer based admixtures

Five different types of polymer admixtures used in this study [12] were -- EVA2, ACL1, PAE2, SBR1 and SBR2, representing the most popular commercially used polymers. The corresponding numerology and properties of above mentioned polymer dispersions are given in Table 4.1. Polymer-cement pastes (PCPs) for the above listed polymers were prepared using ordinary Portland-cement with polymer-cement ratio (P/C) of 20% and water-cement ratio (W/C) at 40% for all the mixes. The above mentioned proportions were attained after extensive sensitivity and trial and error studies on PCPs used.

Table 4.1: Properties of polymer dispersion

Type of polymer	Chemical Constituent	Viscosity	Mechanical properties of polymer-cement paste		
			E	f_c	υ
		(mPa.s)	(MPa)	(MPa)	
EVA2	Ethylene vinyl acetate copolymer emulsion	1000±200	1.82	43.19	0.24
ACL1	Acrylic resin	14	1.55	44.21	0.20
PAE2	Polyacrylic ester-methacrylate ester copolymer emulsion	300	1.29	35.29	0.21
SBR1	Styrene-butadiene rubber	200	1.76	49.78	0.22
SBR2	Styrene-butadiene rubber	50	1.97	50.10	0.20

E - Young's Modulus, f_c - Compressive Strength, υ - Poisson's ratio

Water penetration barrier agents (Impregnants)

Three types of alkyl alkoxysilane based water penetration barrier agents were used -- BPA-I, BPA-II and BPC-I in this study. Additionally application of water and polymers as water penetration barrier agents in place of impregnants was also checked.

4.2.2 Laboratory procedure

4.2.2.1 Workability test

First phase of experiment involved workability tests for different PCPs with pre-application of above mentioned impregnants. Each specimen, as shown in Fig. 4.1, first involved drilling of 8 mm diameter holes 100 mm deep on 100×105×60 mm^3 well-cut brick samples. Dusts in the holes were blown out by applying air pressure. Afterwards 25.13 cm^3 of impregnant was injected into the hole as shown in Fig. 4.2. After 60 minutes of impregnant injection, PCP was injected into the hole. A 6 mm diameter zinc plated full threaded steel bar (SS400) was inserted into the hole at three

different open times -- 0 minute, 5 minutes and 10 minutes for each type of impregnant and PCP. The specimen was placed over digital weighing balance and the amount of force required for the insertion of pin was recorded to measure the workability.

Additional tests were also performed using polymer and water in place of impregnants for the pretreatment. In case of polymer, polymer used in corresponding PCP was used in two different ways. For Polymer-I, polymer was injected into the hole and PCP was poured out after 15/30 minutes. However in case of Polymer-II, PCP was injected into the holes after drying polymer for 5 days after pretreatment of the hole. For comparison, untreated specimens without application of any water penetration barrier agents, termed as untreated specimen here onwards, were also prepared. 63 specimens for each PCP type, with different pretreatment performed and at different open times, were prepared. Total of 315 specimens were prepared for all PCPs to test the workability.

4.2.2.2 Pull-out test

Direct pull-out tests of steel bars were performed on each specimen as illustrated in Fig. 4.3 to compare the bond strength of the PCP in brick masonry. Test specimen was mounted upside down on the testing machine as shown in Fig. 4.3 and the bar was clamped at the other end to the fixed grip at the bottom.

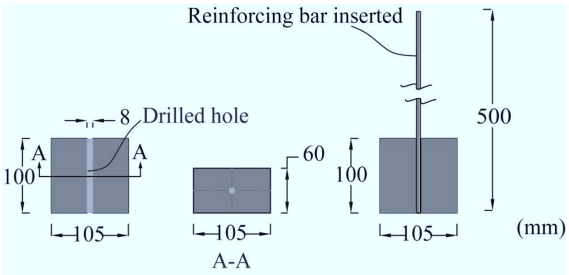

Figure 4.1: Details of test specimen.

Figure 4.2: Application of impregnant (water penetration barrier agent).

The following expression for a straight reinforcing bar inserted in masonry may be derived from the equilibrium of the forces:

$$A_r f_r = \tau_b \pi d_r l_b \tag{4.1}$$

where, A_r and d_r are the area and diameter of reinforcing bar, l_b is the bond length, f_r is the stress developed in the bar, and τ_b is the average bond stress. The average bond stress can be obtained simplifying Eq. 4.1:

$$\tau_b = \frac{f_r d_r}{4 l_b} \tag{4.2}$$

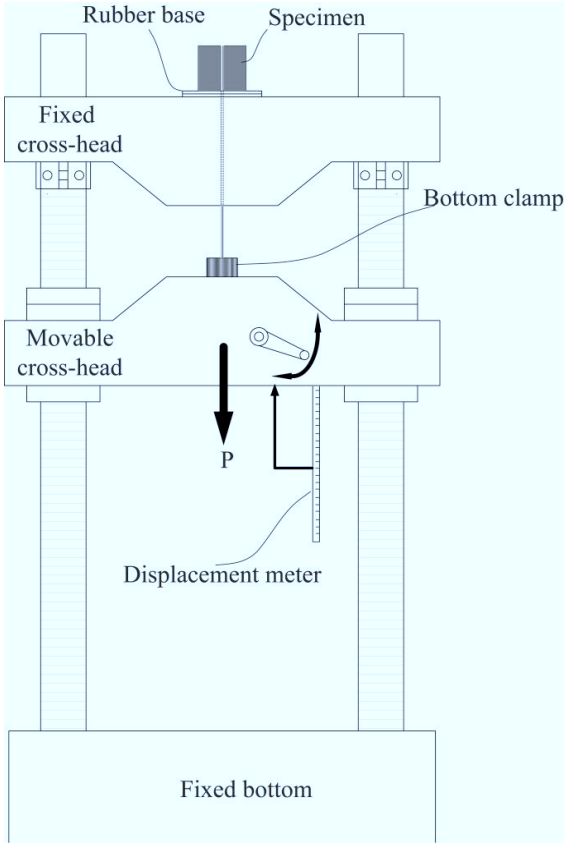

Figure 4.3: Pull-out test set-up.

4.2.3 Results and discussion

4.2.3.1 Workability test

Fig. 4.4 shows results for the test of workability of PCPs with different pretreatments performed. At open time of 0 minute, all combination of pretreatments with PCPs used showed good workable response as shown in Fig. 4.4. With increment in open time up to 5 min with results given in Fig. 4.4(e), reinforcing bar could not be inserted in case of ACL1 PCP when pretreated with Polymer-II. Finally, for open time of 10 min, Polymer-II pretreated ACL1 and SBR2 PCPs were not workable enough for pin insertion and additionally untreated ACL1 sample was also not workable.

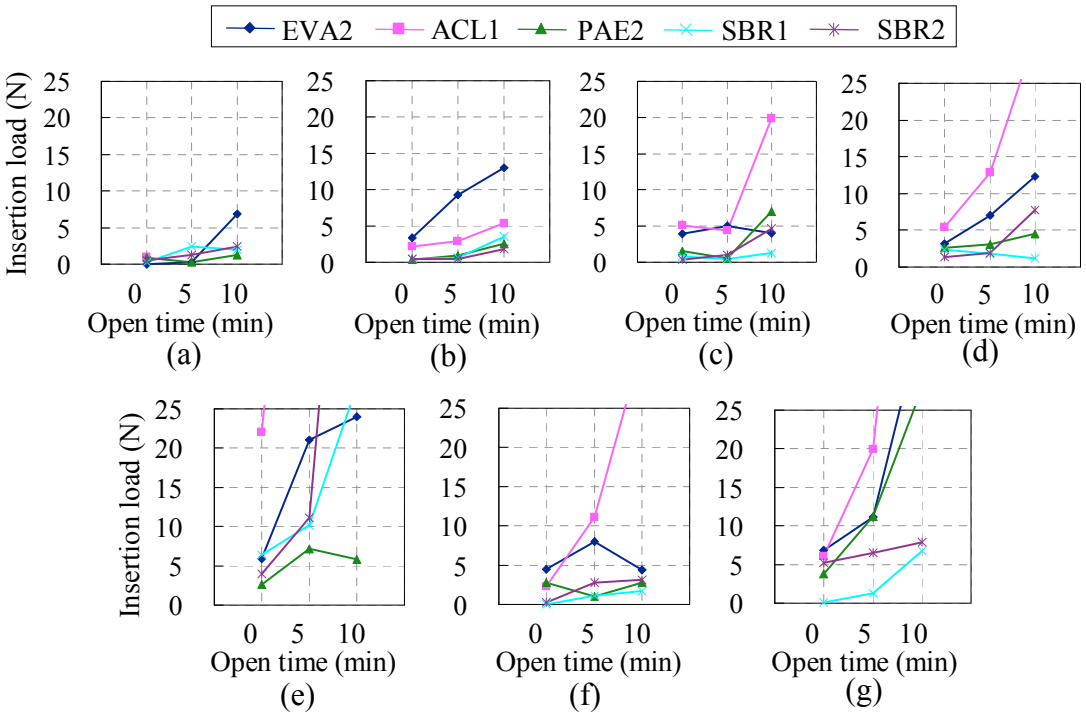

Figure 4.4: Insertion load for combination of PCPs and impregnants at varying open times: : (a) BPA-I, (b) BPA-II, (c) BPC-I, (d) Polymer-I, (e) Polymer-II, (f) Water treated, (g) Untreated.

Workability tests showed clearly that pretreatment plays an important role in keeping the PCP workable for longer duration of time. Use of impregnants -- BPA-I, BPA-II and BPC-I, all significantly increased the workability of all the PCPs used. Test on the use of polymer itself as a water penetration barrier system showed significant differences with Polymer-I working better as a water penetration barrier system as compared to Polymer-II. In fact, Polymer-II adversely affected the workability of the PCPs due to the formation of a thick layer of polymer film by drying, with its response inferior even compared to the untreated specimens.

4.2.3.2 Pull-out test

Direct pull-out test results on steel bars of the specimens are shown in Figs. 4.5 and 4.6. Fig. 4.5 shows the failure patterns observed for pull-out test results. Three different types of failure patterns were observed during the pull-out tests -- bond slip along PCP joint interface, tensile failure of reinforcing bar and brick failure as shown in Fig. 4.5. For impregnant pretreated specimens, dominant failure mechanism observed varied with the type of PCP used. For EVA2, ACL1, PAE2 PCPs, majority of pull-out tests showed bond slip along PCP joint for all the impregnant pretreated specimens. However, for SBR1 and SBR2 PCPs injected specimens pretreated with impregnants, slightly higher bond strengths were observed with higher number of tests resulting in tensile failure of reinforcing bars. This showed the superiority of SBR1 and SBR2 over other PCPs.

Fig. 4.6 shows pull-out test results for specimens with three impregnants -- BPA-I, BPA-II and BPC-I, polymer treated, water treated and untreated for the comparison purpose. There is an obvious variation in bond strengths of different PCPs used with ACL1 and PAE2 having the least of bond strength among the used PCPs. EVA2, SBR1 and SBR2 showed comparatively better bond strengths.

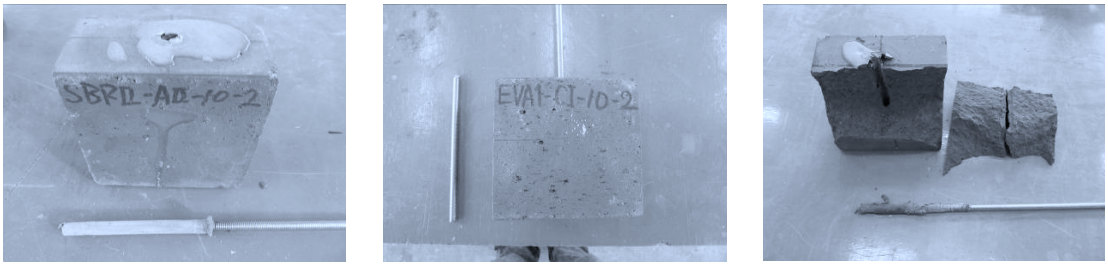

(a) (b) (c)

Figure 4.5: Failure patterns observed during bond strength tests: (a) Bond slip along PCP, (b) Tensile failure of reinforcing bar (c) Brick Failure.

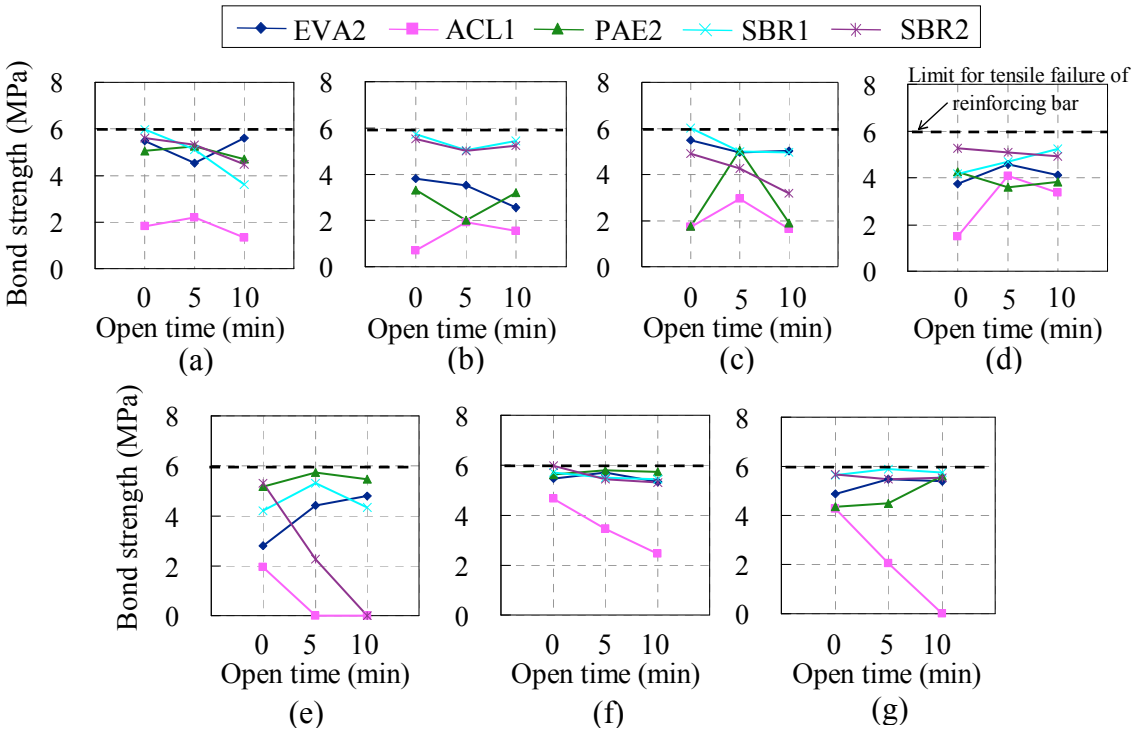

Figure 4.6: Average bond strength from pull-out tests on specimen for different impregnants, polymers, water treated and untreated: (a) BPA-I, (b) BPA-II, (c) BPC-I, (d) Polymer-I, (e) Polymer-II, (f) Water treated, (g) Untreated.

Also bond strength of each PCP was largely affected by other two factors -- pretreatment agent used and open time set. With the increment in open time, average bond strength of PCP was seen to be decreasing in most of the cases. Better PCP would

be the one which shows better bond strength even at larger open time, or the one which shows lesser variation of bond strength at variable open time sets. Table 4.2 shows the consistency of results in terms of bond strength and its coefficient of variation at different open times for combinations of PCPs and impregnants. The best combination of PCP and pretreatment agent showing strong bond with minimum strength variation at different open times was attained for SBR1 and SBR2 PCPs with BPA-II as pretreatment agent as shown in Fig. 4.6(b) and Table 4.2.

Table 4.2: Results for pull-out tests.

PCP / Impregnant	OT	EVA2			ACL1			PAE2			SBR1			SBR2		
		τ_b	σ	γ	τ_b	σ	γ	τ_b	σ	γ	τ_b	σ	γ	τ_b	σ	γ
	(min)	(MPa)	(MPa)	(%)	(MPa)	(MPa)	(%)	(MPa)	(MPa)	(%)	(MPa)	(MPa)	(%)	(MPa)	(MPa)	(%)
BPA-I	0	5.48			1.81			5.06			5.98			5.60		
	5	4.54	0.48	9.15	2.21	0.36	20.45	5.25	0.23	4.50	5.10	0.97	19.85	5.31	0.48	9.35
	10	5.60			1.32			4.71			3.62			4.47		
BPA-II	0	3.82			0.69			3.31			5.72			5.52		
	5	3.52	0.54	16.48	1.93	0.52	37.42	2.00	0.59	20.95	5.04	0.28	5.18	5.00	0.21	4.03
	10	2.55			1.55			3.19			5.44			5.24		
BPC-I	0	5.50			1.72			1.74			6.02			4.91		
	5	4.97	0.24	4.61	2.94	0.59	28.29	5.04	1.52	52.32	4.99	0.49	9.18	4.25	0.71	17.20
	10	5.02			1.65			1.91			4.97			3.19		
Water	0	5.48			5.60			5.63			5.71			5.97		
	5	5.72	0.16	2.91	4.82	0.81	17.36	5.78	0.06	1.07	5.51	0.11	2.01	5.44	0.29	5.14
	10	5.33			3.62			5.73			5.45			5.31		
Untreated	0	4.86			5.67			5.51			5.64			5.68		
	5	5.47	0.27	5.20	N/A	N/A	N/A	4.49	0.51	9.74	5.89	0.10	1.73	5.47	0.09	1.55
	10	5.40			N/A			5.61			5.74			5.53		

OT-Open Time, τ_b – Average bond strength, σ – Standard deviation, γ – Coefficient of Variation

N/A – Not available (unable to insert reinforcing bar)

Untreated and water treated specimens also showed good workability as illustrated in Fig. 4.4 for EVA2, SBR1 and SBR2 injected specimens and majority of pull-out tests resulted in tensile failure of reinforcing bar which meant better bond strength as shown in Table 4.2. However, it should be noted that the experimental tests were performed in

an idealistic condition with well-cut bricks which is particularly different to that in actual practice with old brick masonry and porous mortar joints. This possibly makes untreated and water treated specimens show contradictory behavior to the one observed in this study when performed in real practice. Additionally, when water is used as a pretreatment agent, it is very difficult to pour water in to the hole uniformly resulting in non-uniform distribution of dry and wet surfaces. Therefore, there exists strong evidence of variability for untreated and water treated specimens in actual practice making their use less appealing. A better control of loss of water by PCP, when used in old brick masonry with mortar joints, can be done with the selection of proper water penetration barrier reagents which results in an improved workability without affecting the actual strength of PCP. SBR1 or SBR2 PCP with BPA-II impregnant is the best combination of PCP and pretreatment agent found in this study.

4.3 TEST PROGRAM FOR COMPRESSION TESTS

URM itself is extremely strong in compression; hence it does not require additional strengthening to enhance its compressive strength. The only concern is whether the compressive strength of pinning retrofitted masonry specimens deteriorates from the original URM due to the fissures caused by drilling of holes through the masonry cross-section. Therefore, the main aim of this compression test is to study the change in compressive strength of masonry when pinning retrofitted.

4.3.1 Materials and test set-up

Fig. 4.7 shows masonry assemblage with dimensions 210×210×410 mm^3 (L×B×H) for compression tests. One set of each PCP bonded specimens were prepared. Three different types of commercially available polymer admixtures were used in this study -- SBR, ACL and PAE. Details on these polymer admixtures have been given previously in Section 4.2. PCPs for the above listed polymers were prepared using

ordinary Portland-cement with polymer-cement ratio (P/C) of 20% and water-cement ratio (W/C) at 40% for all the mixes. URM and epoxy bonded (ER) specimens were also prepared for comparison with PCP bonded specimens. For the reinforced specimens, fully threaded SS400 reinforcing bars of 5mm diameter were used. The present study involves use of BPA (Barrier Penetrant) as impregnant for all the PCP bonded specimens. The choice of BPA as impregnant for the purpose of water penetration barrier came from workability tests and bond strength tests performed previously with different types of impregnants available. Fig. 4.8 shows the test set-up for the compression tests.

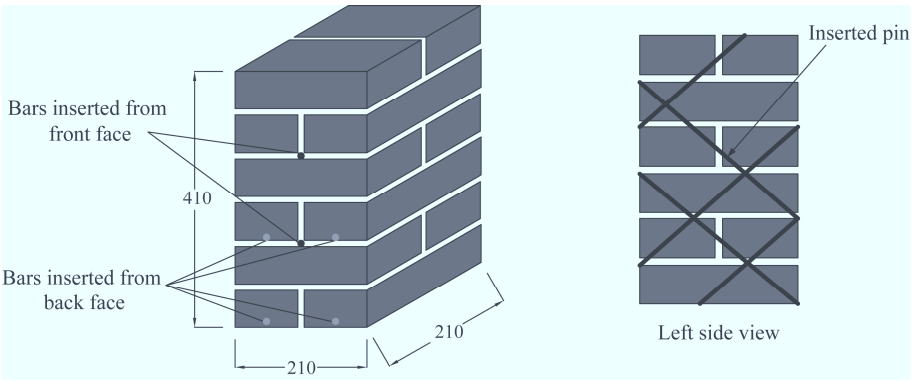

Figure 4.7: Test specimen of masonry assemblage for compression test.

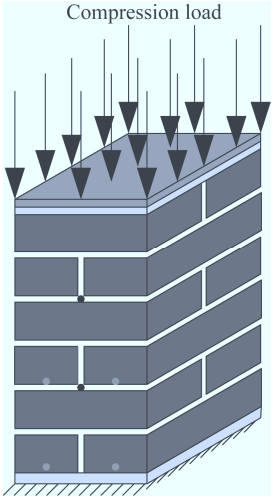

Figure 4.8: Compression test set-up.

4.3.2 Results and discussion

Crack observed for majority of specimens originated from bottom of the specimen where brick units at the bottom showed micro-cracks to start with. For URM specimen, there was no particular stress location with cracks distributed all over the specimen as shown in Fig. 4.9. However for reinforced masonry (RM) specimens, first potential structural crack initiated from the center line of specimen at the exact location from where the pins were inserted as shown in Fig. 4.10. There is an obvious indication of stress concentration and defined crack propagatory path in case of RM specimens as compared to URM specimens. However this behavior did not necessarily affected the performance of the RM specimen as seen from the comparisons made for the resisting force.

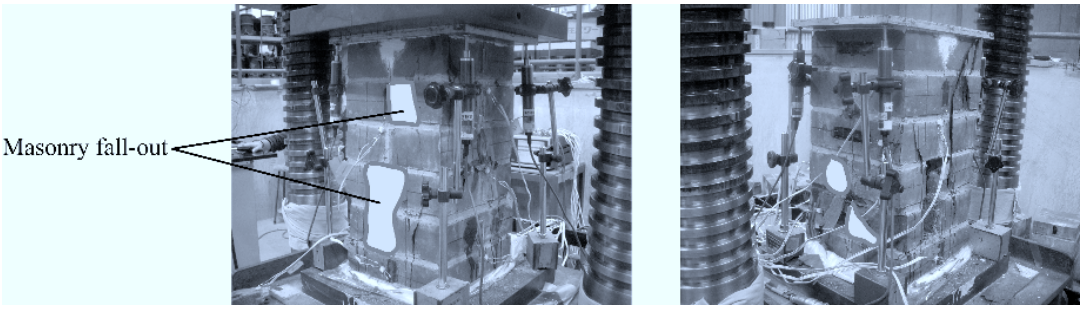

(a) (b)

Figure 4.9: Final failure mechanism for URM specimen: (a) Front view, (b) Back view.

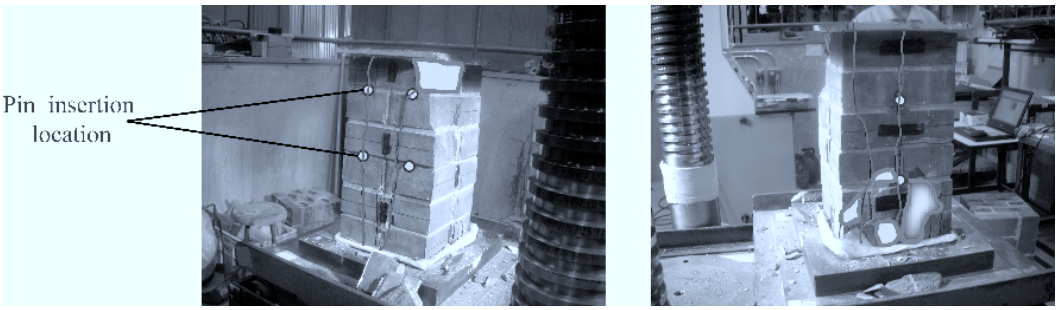

(a) (b)

Figure 4.10: Final failure mechanism for RM specimen: (a) Front view, (b) Back view.

Fig. 4.11 shows the results for the compression test performed on each of the above mentioned specimens. The compressive strength observed for SBR-2 and epoxy specimens were marginally lower that that observed for URM specimen. Additionally, for URM specimen, sudden brittle crushing of masonry was observed. All the RM specimens on the other hand showed improved ductilities.

Fig. 4.12 shows comparison on energy absorption capacity for each of the specimens tested. Slightly enhanced energy absorption characteristics for RM specimens can be seen as compared to URM specimen.

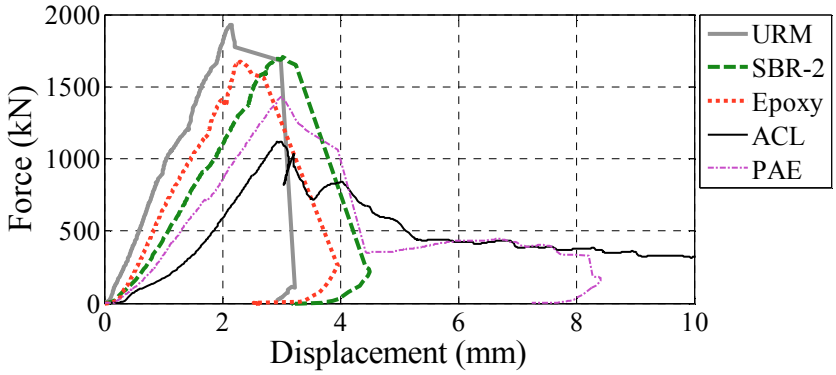

Figure 4.11: Compression test results for all specimens.

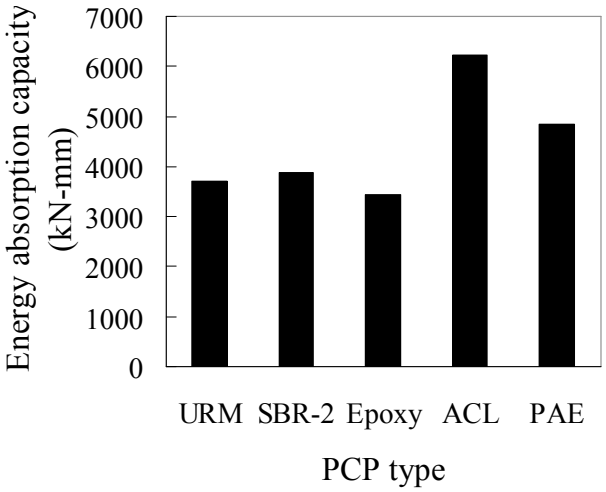

Figure 4.12: Energy absorption capacity for compression tested specimens.

4.4 TEST PROGRAM FOR SHEAR TESTS

4.4.1 Materials and test set-up

Fig. 4.13 shows masonry assemblage with dimensions 340×320×320 mm^3 (L×B×H) for triplet shear tests. Sets of specimens same as the ones in compression test were prepared as described in Section 4.3. Details on these polymer admixtures have been given in previous section. In total 5 different types of specimens were tested, namely URM, SBR-2, Epoxy, ACL and PAE. Fig. 4.13 shows the test set-up for the triplet shear test. An additional frame for horizontal precompression load was also set-up, solely for safety purpose. Hence the bolts were sufficiently loosely tightened at the ends so that the precompression load does not affect the shear strength of masonry assemblage.

4.4.2 Results and discussion

For all the specimens, cracks occurred at the two predefined mortar planes by the sides of center of shear load. Fig. 4.14 shows the response of all the specimens as plot between resisting force versus shear displacement. The first cracking load for all the specimens were very close to each other ranging from 260 to 280 kN. Fig. 4.14 clearly shows brittle failure nature observed in case of URM specimen. RM specimens on the other hand showed better ductile response.

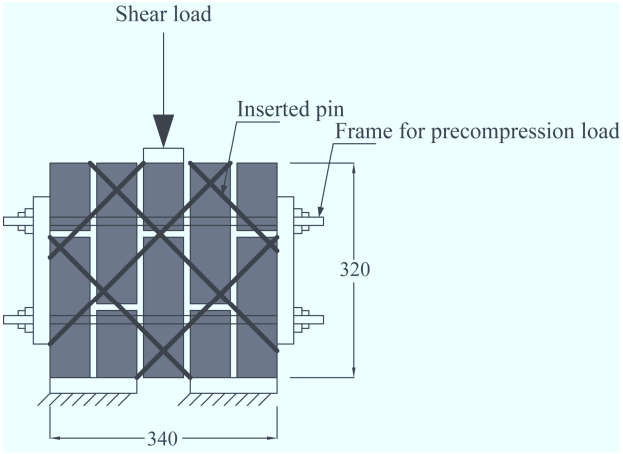

Figure 4.13: Test specimen and set-up for triplet shear test.

Fig. 4.15 shows comparison on energy absorption capacity for each of the specimens tested. Clear indication can be seen of enhanced energy dissipation characteristics for RM specimens as compared to URM specimen. These results reinforce the fact that RM specimens are more capable for resisting load for longer duration showing better ductile response resulted due to reinforcement yielding.

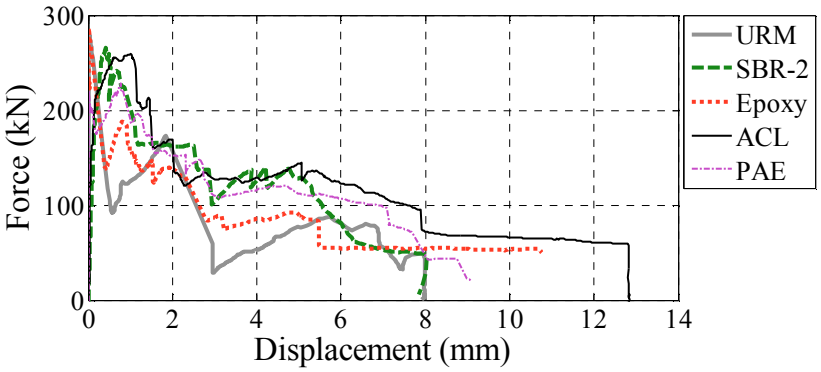

Figure 4.14: Shear test results for all specimens.

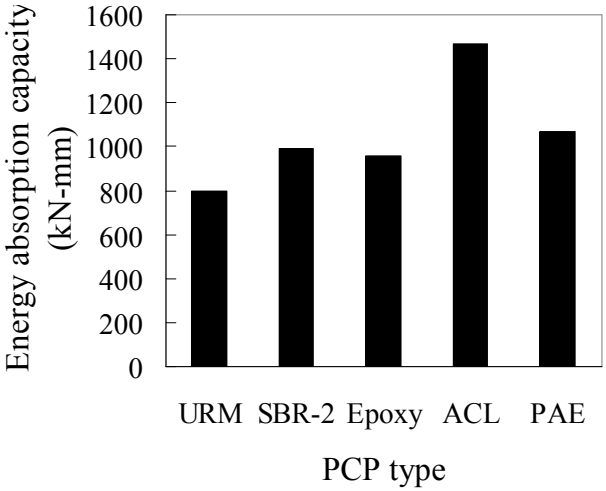

Figure 4.15: Energy absorption capacity for shear tested specimens

4.5 TEST PROGRAM FOR ONE-POINT BENDING TESTS

4.5.1 Materials and test set-up

Fig. 4.16 shows the masonry beam specimen with dimensions 1040×320×320 mm^3. Two sets of each PCP bonded specimens were prepared. Three different types of commercially available polymer admixtures were used in this study – SBR2, ACL and PAE same as to the ones performed in former compression and shear tests. Details on these polymer admixtures have been given previously in Section 4.2.

4.5.2 Results and discussion

Fig. 4.17 shows the results for one-point bending test performed on each specimen [13]. Cracks observed for the specimens as shown in Figs. 4.18 and 4.19 varied with the type of specimen. ER and SBR-2 specimens showed mode 1 kind of failure shown in Fig. 4.18. For URM, SBR-1 and ACL-1 specimens, mode 2 failure as shown in Fig. 4.19 was observed. The prediction of crack in masonry is highly unpredictable mainly attributed by the fact that there exists large deviation in strength of mortar joints from specimen to specimen. Resisting force corresponding to the particular failure mode has been predicted assuming a free-body as shown in Figs. 4.18(b) and 4.19(b) neglecting the bed-joint tensile strength. Equilibrium condition for the given free bodies gives following expression:

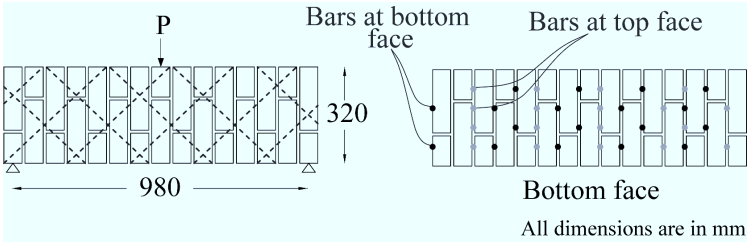

Figure 4.16: Specimen and test set-up for one-point bending test.

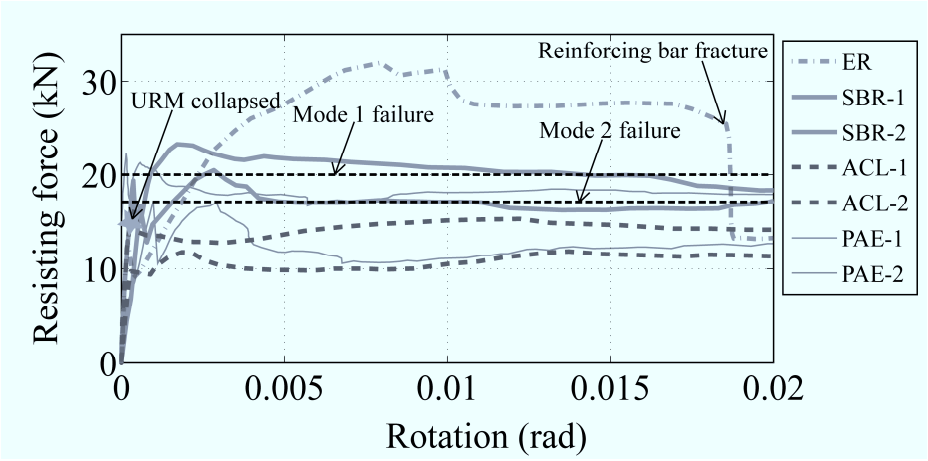

Figure 4.17: Bending test results for all specimens.

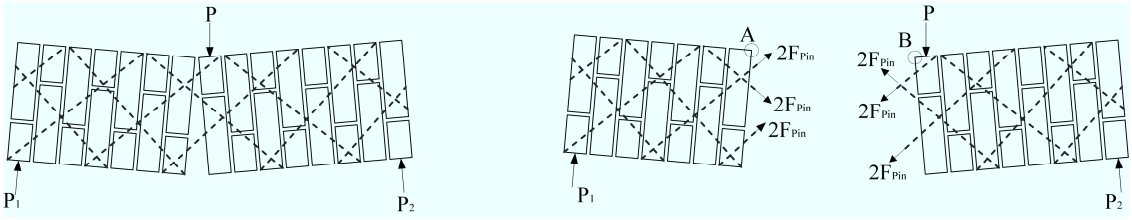

(a) (b)

Figure 4.18: Failure mode 1: (a) Deformed shape, (b) Free body diagram.

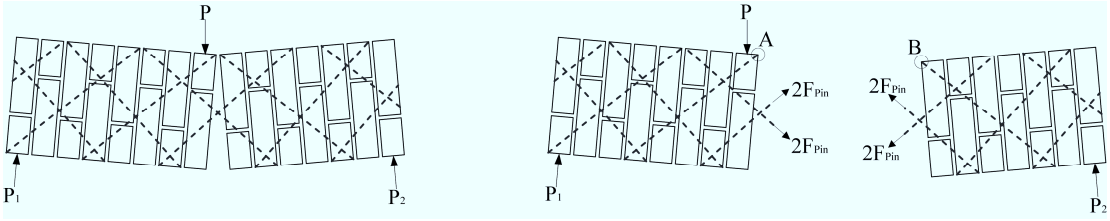

(a) (b)

Figure 4.19: Failure mode 2: (a) Deformed shape, (b) Free body diagram.

$$\begin{aligned} &\text{Moment about A, } P_1 \times L_1 = \frac{2F_{\text{pin}}}{\sqrt{2}} \sum_{i=1}^{n} L_{\text{pin}}^{i} \\ &\text{Moment about B, } P_2 \times L_2 = \frac{2F_{\text{pin}}}{\sqrt{2}} \sum_{i=1}^{n} L_{\text{pin}}^{i} \\ &F_{\text{R}} = P_1 + P_2 \end{aligned} \tag{4.3}$$

where L_1, L_2 is the distance of reaction force from the point of rotation, F_{pin} is the reinforcing bar tensile strength assuming f_{y}=400MPa and L_{pin}^{i} is the distance of ith

reinforcing bar from the point of rotation in the free body. Using Eqn. 4.3, the value of predicted resisting force F_R for mode 1 failure is 20.5kN and mode 2 failure is 17.3kN as shown in Fig. 4.17.

In Fig. 4.17, resisting force versus rotation angle plot has been made for each specimen. For URM specimen, after the initiation of first crack at around 15kN of resisting force and very small deformation angle, the specimen collapsed with no resistance shown afterwards. For ER specimen, maximum resisting force of around 32kN was observed larger than for any of other specimens and even higher than the theoretically predicted resisting force for both failure modes. This large resisting force was contributed by strength of epoxy resin itself whose bond strength is higher than the reinforcing bar's tensile strength. For the same reason fracture of reinforcing bar was observed for ER specimen at 0.018 radian rotation angle.

For PCP bonded specimens, SBR specimens showed comparatively better response. The maximum resisting force for SBR specimens showed resistance close to the theoretically predicted strength representing yielding of reinforcing bars used. No fracture of reinforcing bar was observed for SBR specimens. ACL and PAE specimens on the other hand showed relatively lower value of resisting force significantly lower than the theoretically predicted value which clearly signified bond slip of the reinforcing bars.

4.5.3 Finite element modeling

Corresponding finite element models for the one-point bending tests performed were prepared. The basic methodology and modeling technique adopted are in close relation to the one described in detail in Chapter 3, so further discussions on FE generation will be avoided. The major difference however in the model generation here would be inclusion of bond slip interface elements between reinforcing bar and masonry elements to simulate the bond slip of reinforcing bars.

Special bond slip interface elements as shown in Fig. 4.20 has been incorporated in the FE model. It should be noted that bond slip interface was modeled only for the pins inserted near the center of the specimen where majority of cracks, reinforcement yielding and bond slips were observed during the experimentation. Another notable assumption was exclusion of horizontal mortar joint; only vertical mortar joints were modeled since cracks were only observed in vertical mortar joints. Main reasons for above assumption and confining of bond slip interfaces to certain zones were to reduce the model complexity and get better solution convergence.

For FE analysis, models with varying bond slip strengths were adopted with 5 cases of bond strength values -- $0.4\tau_b$, τ_b, $1.6\tau_b$, $2.0\tau_b$, $3.0\tau_b$, where mean value of PCP bond strength τ_b is 2.5 MPa.

FE result plotted against the experimental observations showed comparable response and effective prediction of resisting force as shown in Fig. 4.21. Sensitivity of varying bond strength on the flexural response of the specimens can be clearly seen in Fig. 4.22. Higher bond strength meant larger resisting force and lower bond strength corresponded to lower resistance. More importantly all the reinforced specimens showed largely ductile response.

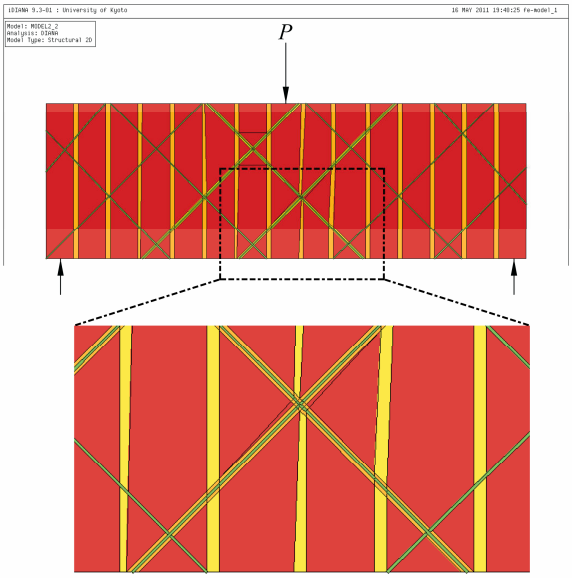

Figure 4.20: FE model generation with bond slip interface.

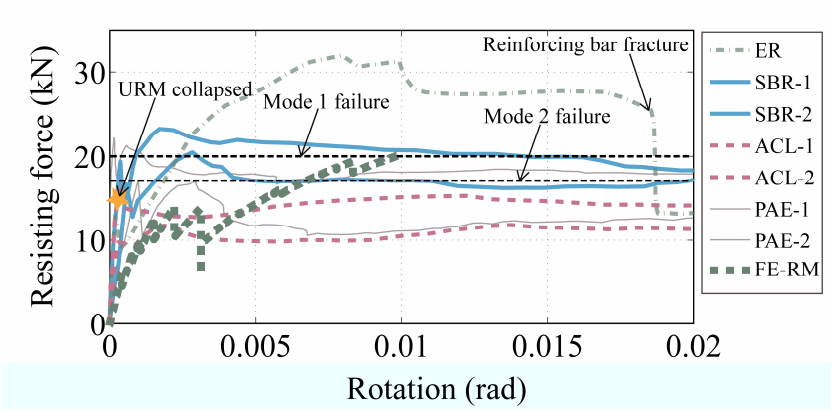

Figure 4.21: Comparison of experimental and FE bending test results.

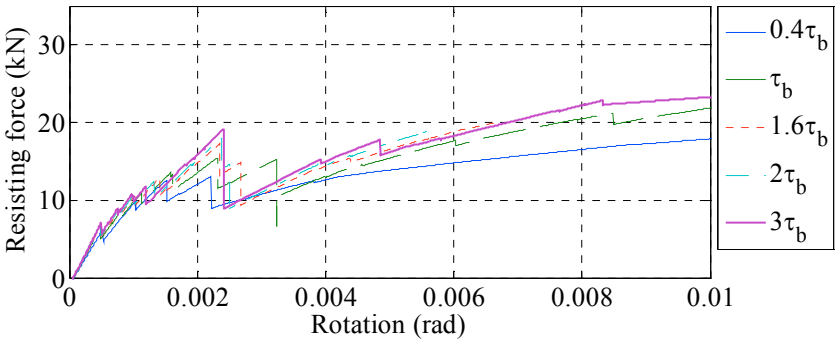

Figure 4.22: Comparison of FE sensitivity study at varying bond strengths.

4.6 CONCLUSION

This chapter deals with the experimental works done to compare the workability and bond strength of different polymer-cement pastes (PCPs) -- EVA2, ACL1, PAE2, SBR1 and SBR2, in brick masonry. Additionally, compression tests, shear tests and one-point bending tests were also performed to compare the effectiveness of particular PCPs in masonry assemblages. Based on these tests, the following conclusions can be drawn:

(1) Results of workability tests showed PCPs are highly workable even at adverse working conditions, specifically for untreated specimens of SBR1 and SBR2 PCPs workable even at the open time of 10 minutes. The workability test also showed the importance of pre-treatment agents or impregnants, as water penetration barrier system, to increase the workability of PCP, effectively avoiding the loss of water from PCP. The

untreated and polymer treated specimens showed poor performance whereas use of BPA-I, BPA-II and BPC-I as impregnants resulted in substantial increment of workability. Additionally, use of impregnants did not influence the strength of PCPs used.

(2) From the pull-out test results, ACL1 and PAE2 have least bond strength as compared to EVA2, SBR1 and SBR2 PCPs. Observed bond strengths of EVA2, SBR1 and SBR2 PCPs were in the range of 5 MPa or more, which represents extremely superior bond strength.

(3) Both compression and shear tests showed notable difference in response between unreinforced and reinforced specimens with the later showing substantial increment in ductility.

(4) One-point bending tests performed also showed significant difference in unreinforced and reinforced specimens. ACL and PAE bonded specimens showed relatively lower resistance due to premature bond slip of the reinforcing bars. SBR PCP bonded specimen showed better resistance. Proposed theoretical and FE prediction also showed response comparable to the experimental observations.

(5) The best combination of PCP and pretreatment agent, showing strong bond with minimum strength variation at different open times and also better resistance when tested as masonry assemblage, was attained for SBR PCPs with BPA-II impregnant as pretreatment agent.

REFERENCES

[1] ABRAMS D., SMITH T., LYNCH J., and FRANKLIN S. Effectiveness of Rehabilitation on Seismic Behavior of Masonry Piers, *Journal of Structural Engineering*, 133(1): 32-43, 2007.

[2] WILLIS C. R., SERACINO R. and GRIFFITH M. C. Out-of-Plane Strength of Brick Masonry Retrofitted with Horizontal NSM CFRP Strips, *Engineering Structures*, 32(2): 547-555, 2010.

[3] TAKIYAMA N., NAGAE T., MAEDA H., KITAMURA M., YOSHIDA N., and ARAKI Y. Cyclic out-of-plane flexural behavior of masonry walls rehabilitated

by inserting STAINLESS pins, *Proceedings of 14WCEE*, Beijing, 2008. http://www.iitk.ac.in/nicee/wcee/article/14_S11-015.PDF (Last accessed date: January 19, 2011).

[4] SHRESTHA K. C., NAGAE T. and ARAKI, Y. Finite Element Modeling of Cyclic Out-of-Plane Response of Masonry Walls Retrofitted by Inserting Inclined Stainless Steel Bars, *Journal of Disaster Research*, 6(1): 36-43, 2011.

[5] SHRESTHA K.C., NAGAE T. and ARAKI Y. Finite element study on pinning retrofitting technique of masonry walls with opening subjected to in-plane shear load. *Proceedings of 7th International Conference Analytical Models and New Concepts in Concrete and Masonry Structures*, Krakow, 2011.

[6] PAREEK S. Evaluation of Polymer-Cement Pastes as Bonding Agents for Flexural Strengthening of RC Beams by Continuous Fiber Sheets, *Proceedings of the International Symposium on Latest Achievement of Technology and Research on Retrofitting Concrete Structures*, Japan Concrete Institute, 2003, pp. 107-112.

[7] OHAMA Y. Polymer-Based Admixtures, *Cement and Concrete Composites*, 20: 189-212, 1998.

[8] OHAMA Y. Handbook of Polymer-Modified Concrete and Mortar, Properties and Process Technology, Noyes Publications, 1995.

[9] FOWLER D. W. Polymers in Concrete: A Vision for the 21st Century, *Cement and Concrete Composites*, 21: 449-452, 1999.

[10] KIKUCHI K., KUROKI, M., TOYODOME M., ESCOBAR C., and NAKANO Y. Seismic Retrofit of Unreinforced Clay Brick Masonry Wall Using Polymer-Cement Mortar, *Proceedings Of the 14WCEE*, Beijing, 2008.

[11] ANAGNOSTOPOULOS C. A., and ANAGNOSTOPOULOS A. C. Polymer-Cement Mortars for Repairing Ancient Masonries Mechanical Properties, *Construction and Building Materials*, 16: 379-384, 2002.

[12] SHRESTHA K. C., PAREEK S., and ARAKI Y. Use of polymer-cement pastes as bonding agents for pinning retrofitting of masonry construction, *Proceedings of JCI*, 33, 2011.

[13] SHRESTHA K. C., PAREEK S., ARAKI Y. Bending tests on pinning-retrofitted masonry beams with use of polymer cement pastes as binding agents, *Proceedings of Architectural Institute of Japan*, 2011.

5

APPLICABILITY OF Cu-Al-Mn SHAPE MEMORY ALLOY (SMA) BARS TO RETROFITTING OF MASONRY WALLS

5.1 GENERAL

As reported extensively in Chapter 2 through 4, recent accountings on Italy and New Zealand earthquakes showed clearly proneness of unreinforced masonry (URM) walls in historical masonry constructions. As a result there have been extensive researches in developing techniques for improving seismic behavior of URM walls [1-6] with techniques involving - attachment of reinforcing members, surface treatment, grout injection, post-tensioning, and reinforced core technique.

Among the reinforcing techniques listed above, reinforced core technique, wherein reinforcing steel bars are inserted vertically into holes drilled at the center of URM

walls, is often suitable for retrofitting historical masonry constructions because the technique does not change the appearance of URM walls and enhances both strength and ductility [1,5]. In reinforced core technique, however, the use of steel bars as reinforcing elements may lead to pinching, or degradation of stiffness and strength under cyclic loading caused by inelastic elongation of reinforcing steel bars [7,8]. Pinching phenomena, represented by large narrow region of zero stiffness in the hysteresis loops for load in the stages of cycle beyond yielding of the vertical steel, is attributed to residual plastic deformations in the steel. This particular phenomenon with its typical stages during the loading history has been schematically presented in Fig. 5.1. These unstable states as shown in Fig. 5.1, typically in second post-yield cycle, increase collapse potential of masonry walls. Moreover, it becomes difficult to repair with minor interventions like inserting grouts into mortar joints. This pinching region can be greatly reduced with use of high strength steel, allowing reinforcing bars to work essentially in linear range, but this also has major drawback of no energy dissipation and possibility of sudden brittle failure of reinforced masonry walls.

To overcome the difficulties mentioned above, there is a surge in interest in application of shape memory alloys (SMAs) to retrofitting of historical masonry constructions [9-11]. The desired phenomenon with a typical flag shaped hysteresis for the SMA reinforced structure is shown in Fig. 5.1. The first known example of SMAs applied in a retrofit project of a historical masonry construction is done by Ref.[12] on S. Giorgio Church Bell Tower. The rehabilitation process involved post tensioning using devices with SMA wires of 1 mm diameter. After this project, SMA wires were applied to several retrofitting projects of existing historical masonry constructions [13-15]. SMAs with superelasticity, or shape recovery property on unloading, are attractive in retrofitting of historical masonry constructions because they dissipate energy, limit force transmissions, and reduce or eliminate residual deformations. These characteristics stabilize retrofitted historical masonry constructions during and after intense earthquakes.

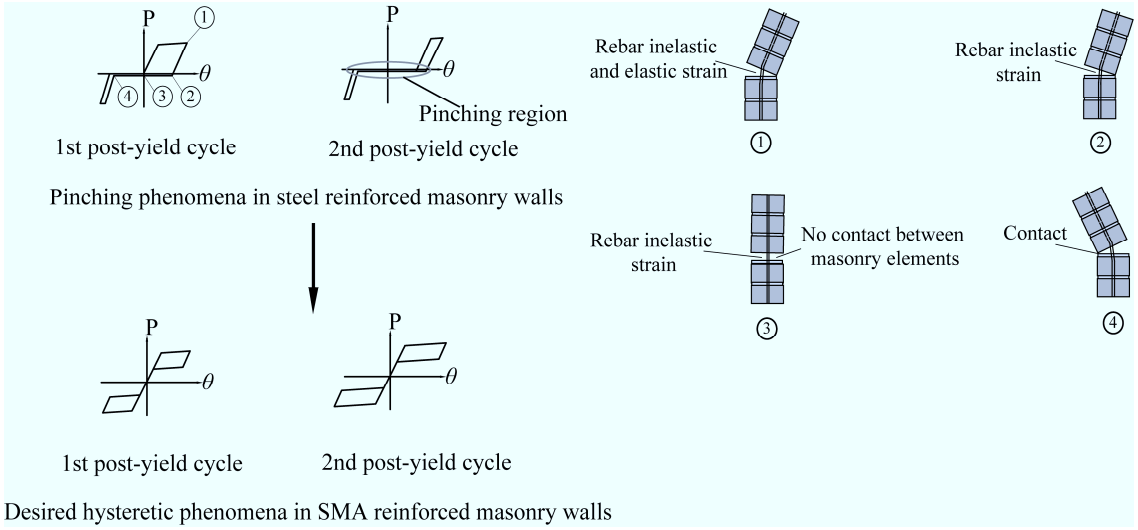

Figure 5.1: Typical post yield cyclic behavior of steel reinforced center core technique with deformed shapes [7] and desired hysteretic phenomena for SMA reinforced masonry walls.

In most studies and projects conducted so far, Ni-Ti SMAs were applied to retrofitting of historical masonry constructions because of their superior mechanical properties to other SMAs. Nevertheless, high material cost and machining difficulty of Ni-Ti SMAs hinder their wide-spread use in retrofitting of historical URM constructions. As an alternative class of SMAs, application of Cu-Al-Be SMAs to retrofitting of historical masonry constructions was studied because of their lower cost and higher machinability [16]. To the authors' knowledge, however, superelasticity of Cu-Al-Be SMAs is significantly inferior to, about half of, that of Ni-Ti SMAs. Moreover, beryllium and beryllium compounds have potential risks to human health unless properly handled.

With a goal for superior SMAs with lower cost and higher machinability, development Cu-Al-Mn SMAs is underway [17,18]. The superelasticity of Cu-Al-Mn SMAs is comparable to Ni-Ti SMAs, and they have essentially no risks to human health. Nevertheless, the diameter of the Cu-Al-Mn SMA wires produced was limited to be less than or equal to 1.5 mm due to the dependence of superelasticity on grain size. Recently,

Ref.[19] have succeeded to obtain Cu-Al-Mn SMA bars with diameters of 4 mm and 8 mm whose superelasticity is comparable to Ni-Ti SMA bars by making grain sizes large enough.

This chapter is devoted to state the applicability of newly developed Cu-Al-Mn SMA bar to retrofitting of historical URM constructions. Although superelasticity of Cu-Al-Mn SMA is not superior to that of Ni-Ti SMAs, Cu-Al-Mn SMA is superior from the viewpoints of machinability, cold workability, and material cost. The first portion of the chapter reports on quasi-static cyclic out-of-plane tests performed on masonry walls reinforced by SMA bars with reinforced core technique presented by author in Ref.[20]. Quasi-static tests showed effectiveness and suitability of SMA bars over conventional steel reinforcements. However, the rate dependence and overall dynamic response of SMA reinforced masonry walls was still not known. The second portion of this chapter hence presents the dynamic tests conducted on SMA reinforced specimens subjected to actual earthquake excitation. Tests were performed on half scaled SMA reinforced masonry (SMA-RM) specimens; URM and steel reinforced masonry (ST-RM) specimens were also tested for comparison purpose. Finite element (FE) models are developed in reference to the mechanism obtained from the test results.

5.2 SPECIMENS AND MATERIALS

Fig. 5.2 shows the geometry of a brick wall specimen. A single-wythe brick wall specimen was constructed respectively for the URM, ST-RM and SMA-RM wall. The wall specimen represents a top storey gable wall with low level of anchorage system between the wall and the top support making the wall fail in cantilever action. Half-scaled bricks of 95 mm x 53 mm x 31 mm were used to construct the wall specimens. The bricks have holes for inserting bars in case of the reinforced specimens. For the reinforced masonry specimens, 2 reinforcing bars with 4 mm diameter were inserted at the spacing of 150 mm. The reinforcement design satisfies the minimum

requirement of reinforcement in European Standard [21]. Fig. 5.3 shows the procedures involved in the reinforced specimen preparation. Fig. 5.3(a) shows a SMA bar after threading. Threading of SMA bars was as easy as normal steel, which is a distinct characteristic of Cu-Al-Mn SMAs compared to Ni-Ti SMAs. As shown in Figs. 5.3(b) to (e), the specimen was constructed on a concrete block by professional masons. After placing another concrete block on the specimen as shown in Fig. 5.3(f), bolts were tightened lightly at the both ends of reinforcing bars to fix the brick wall specimen to the concrete blocks.

Table 5.1 shows the mean and standard deviation values obtained from the material tests of bricks, mortars, and masonry prisms for compressive strength f_c and tensile strength f_t [22,23]. The composition of water, cement, and sand for the mortar was 1:1:4.5. JIS SS400 steel bars of 4 mm diameter were used in the ST-RM specimens. Tensile tests done on SS400 steel bars gave yield stress and strength of about 200 MPa and 400 MPa respectively. For the SMA-RM specimens, Cu-Al-Mn SMA bars with 160 mm length were used only at the lower portion of the SMA-RM wall specimen. The upper portion of the reinforcing bar was SUS304 stainless steel, whose nominal strength is 520 MPa.

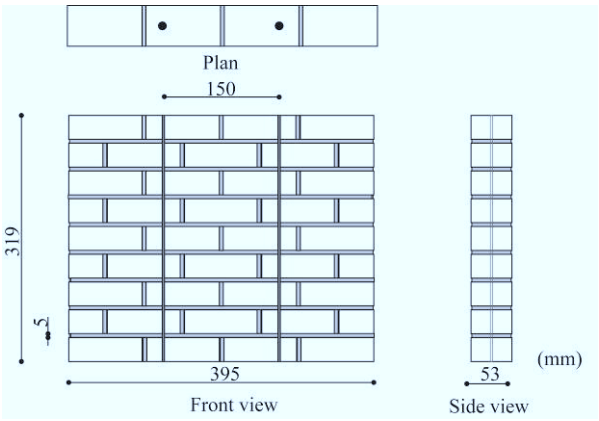

Figure 5.2: Geometry of a brick wall specimen.

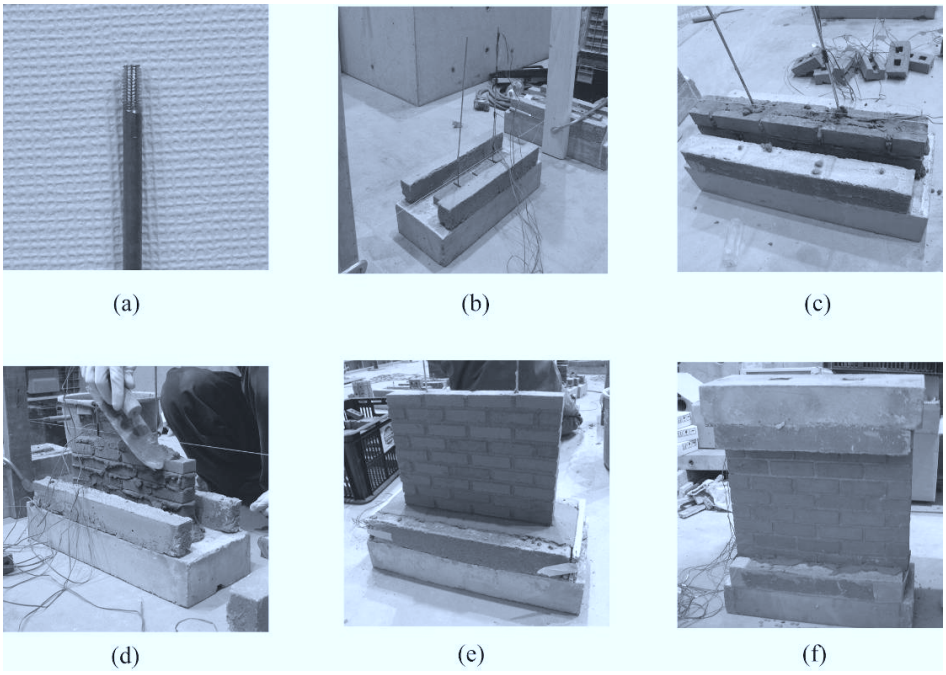

Figure 5.3: Processes involved during specimen preparation: (a) threaded SMA bar, (b) concrete block with SMA bar inserted, (c) position of coupler connecting SMA bar and stainless steel bar, (d) brick laying, (e) completion of brick laying, and (f) placement of concrete block support on the top of specimen.

Cu-16.7 at.%Al-11.6 at.%Mn alloy was prepared by Furukawa Techno Material Co., Ltd, where SMA bars with diameters of 4 mm were obtained by hot forging and cold drawing. The solution treatment was conducted at 900 ºC, followed by quenching in water, and they were subsequently aged at 200 ºC to stabilize superelastic property. The SMA bars were trained beforehand up to strain of 3 % by applying quasi-static cyclic loading before inserting them into brick wall specimens. Stress-strain histories for the two SMA bars after training are shown in Fig. 5.4. From the figure, it can be seen that the yield, or forward transformation stresses of the SMA bar are in the range between 120 MPa to 140 MPa. And the maximum stress experienced ranges from 240 MPa to 250 MPa. Both the SMA bars have the recovery strain of more than 2% after the training. It should be noted that strain observations made in Fig. 5.4 could possibly be overestimated due to cross-head measurements of strain. As a result, the initial modulus observed in Fig. 5.4 may be significantly less than the nominal value of SMAs.

Table 5.1: Material properties of brick and mortar.

	Masonry prism f_c (MPa)	Brick unit f_c (MPa)	Mortar cube f_c (MPa)	Masonry prism f_t (MPa)	Mortar bar f_t (MPa)
Method	LUMB 1 [22]	ASTM C 67-07 [23]	ASTM C 1019-05 [23]	ASTM E 518-03 [23]	ASTM C 580-02 [23]
Mean	13.52	35.79	18.40	0.47	4.50
Deviation	3.13	6.57	0.17	0.22	0.15

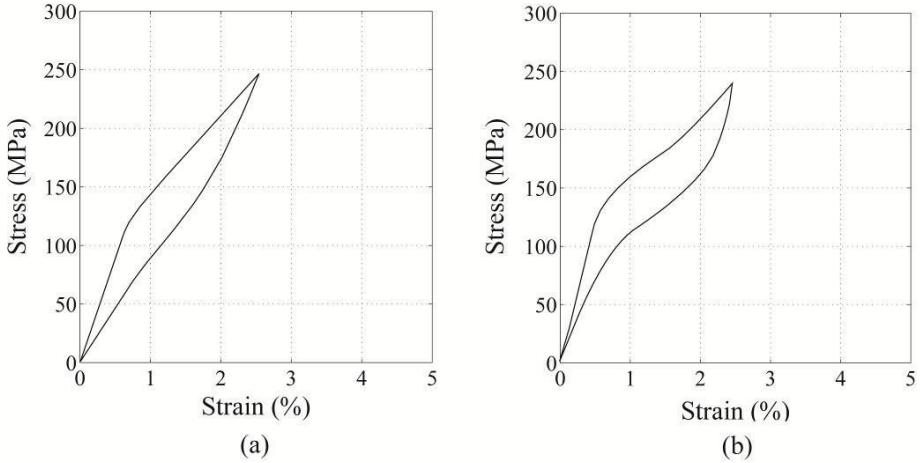

Figure 5.4: Stress-strain relations after training for: (a) SMA bar 1, (b) SMA bar 2.

5.3 FINITE ELEMENT MODELING

5.3.1 Model generation

Masonry walls subjected to out-of-plane loading experience predominantly tensile failure in mortar joints. The out-of-plane response of URM walls is highly nonlinear and is often governed primarily by cracking at mortar joints and rocking resistance due to gravity rather than compressive failure of masonry and mortar materials. Masonry walls can be represented with significant simplification with entire mortar joint by interface element [24]. With this approach, the failure of brick-mortar interface is not distinguished from that of mortar layer itself. In this paper, complete FE models were generated and analyzed using the general purpose FE program DIANA9.3 [25].

Masonry walls were modeled by assuming that brick units are fully elastic and material nonlinearity was concentrated on truss elements and interface elements. Rocking resistance due to gravity is incorporated by considering geometrical nonlinearity.

The FE model with the meshing adopted for the brick continuum elements and the interface elements are shown in Fig. 5.5. A masonry brick unit was modeled using rectangular continuum elements that were connected with vertical and horizontal interface elements representing mortar and bond slip interface. For the reinforced masonry wall specimens, truss elements with proper constitutive relations and interface elements representing the bond slip interface between reinforcement elements and masonry elements were used. The details of the elements used are described below.

5.3.1.1 Brick

As mentioned above, bricks were modeled to work perfectly elastic during the whole loading history and modeled with four-node quadrilateral continuum elements. Material properties used included Young's modulus E_b = 12 GPa, Poisson's ratio υ_b = 0.15, and density, ρ_b =2000 kg/m^3 taken for typical masonry bricks [26].

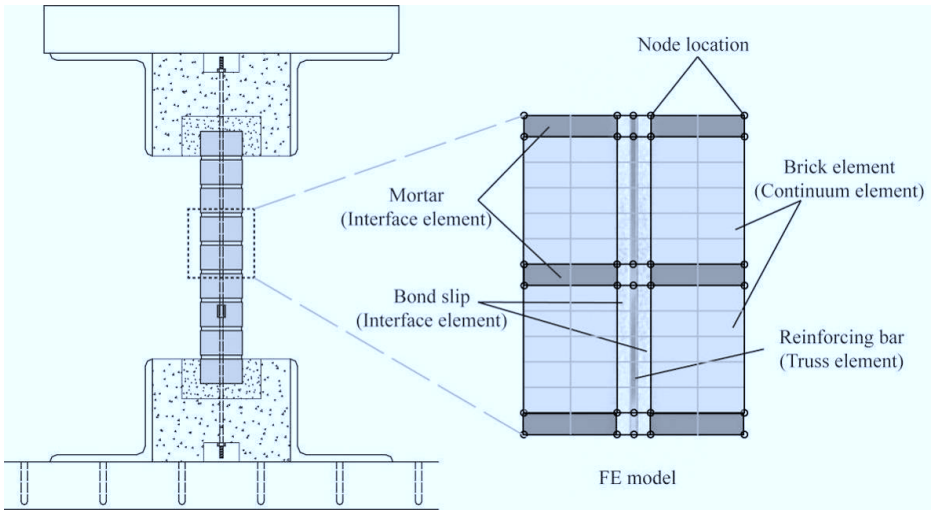

Figure 5.5: FE mesh showing the brick unit, mortar interface, bond slip interface and reinforcing truss element bar.

5.3.1.2 Interface

Entire mortar joint was represented by brick unit/mortar interface. The interface model used in this study is implemented in DIANA9.3 [25] as linear interface elements between two lines (2+2 nodes). The constitutive model adopts a discrete crack initiation criterion of normal traction characterized by full reduction of strength after the strength criterion has been violated. A discrete crack arises if the normal traction f_n exceeds the tensile strength of mortar, f_t=0.47 MPa. The behavior can be written as

$$\frac{f_n(\Delta u_n)}{f_t} = \begin{cases} 1 & \text{if } \Delta u_n \le 0 \\ 0 & \text{if } 0 < \Delta u_n < \infty \end{cases} \tag{5.1}$$

where Δu_n is the deformation in the direction of normal traction f_n. The normal stiffness of D_{11}=82 N/mm^3 and the shear stiffness of D_{22}=36 N/mm^3 were adopted for the brick/mortar interface [24].

A special interface element, named as nut interface as shown in Fig. 5.6, was incorporated to simulate the contact between nuts and brick. This element was particularly important to represent the pinching mechanism of the ST-RM specimen. The nut interface element adopted a discrete crack initiation criterion of normal traction with brittle behavior similar to the one adopted for mortar as given in Eqn. 5.1. Here, the material strength property with f_t=0.2MPa was used. The tensile strength of this interface element was kept low enough and calibrated suitably so as to result in the loss of contact, or crack initiation, during unloading.

The bond-slip interface between reinforcing elements and masonry elements were represented by two types of interface elements, named Bond 1 and Bond 2, as shown in Fig. 5.6. The bond slip model proposed by Dörr [25] was used. The model uses a polynomial relation between shear traction and slip which shows a limit if the slip is larger than a certain value dt^0. The formulation for shear traction t_t is given by a cubic function:

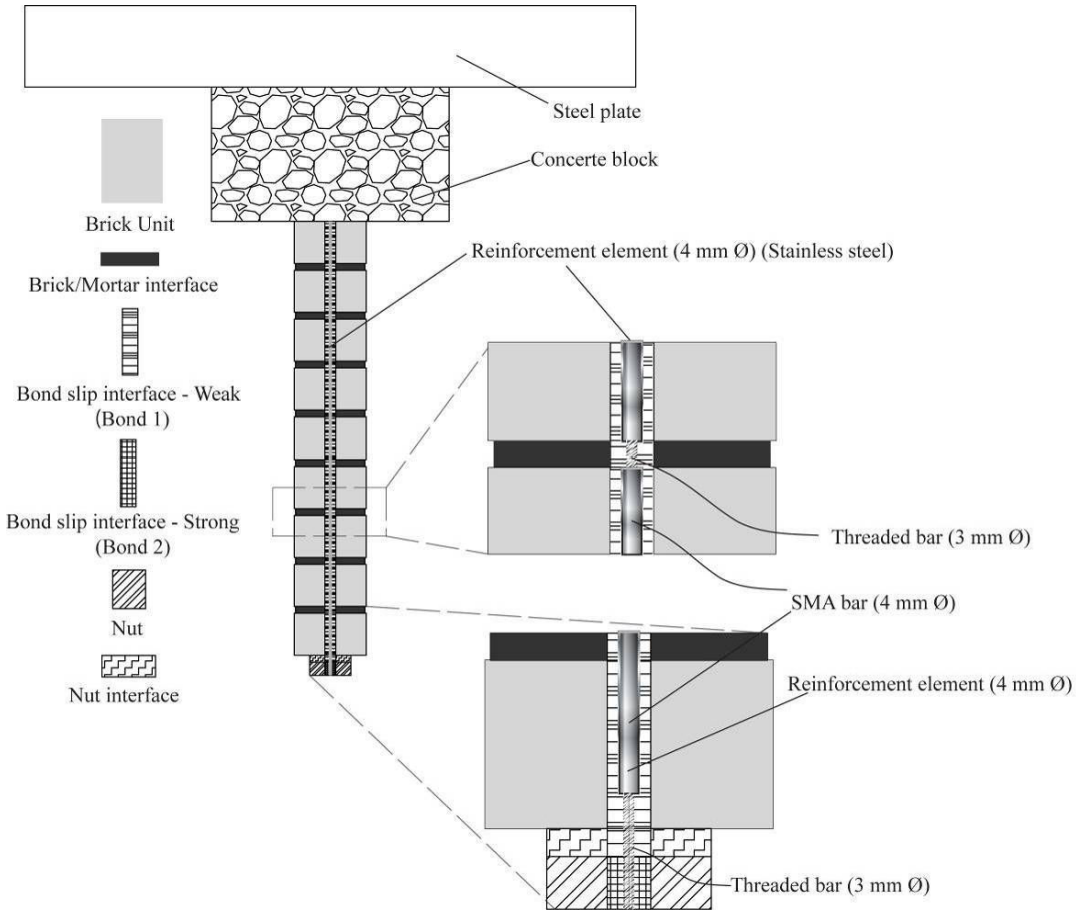

Figure 5.6: FE model generation (SMA-RM model).

$$t_{\mathrm{t}} = \begin{cases} f_{\mathrm{s}}\left(5\left(\dfrac{\mathrm{d}t}{\mathrm{d}t^{0}}\right) - 4.5\left(\dfrac{\mathrm{d}t}{\mathrm{d}t^{0}}\right)^{2} + 1.4\left(\dfrac{\mathrm{d}t}{\mathrm{d}t^{0}}\right)^{3}\right) & \text{if } 0 \le \mathrm{d}t < \mathrm{d}t^{0} \\ 1.9 f_{\mathrm{s}} & \text{if } \mathrm{d}t \ge \mathrm{d}t^{0} \end{cases} \tag{5.2}$$

where f_{s} is the slip strength and $\mathrm{d}t^{0}$ is the limiting slip distance. Unloading and reloading of the interface shear behavior is modeled using a secant approach as shown in Fig. 5.7.

FE model incorporates two bond-slip interfaces as reported earlier, one between the reinforcing elements and the masonry elements represented as Bond 1 and the other between reinforcing elements and nut represented by Bond 2 as shown in Fig. 5.6. The bond strength for Bond 1 interface was intentionally made very weak to allow slip of reinforcing elements with slip strength, f_{s}=0.1MPa and limiting slip distance,

dt^0=0.06mm, where the slip strength parameter has been properly calibrated and kept sufficiently low so as to allow slip during unloading once the reinforcing bars get elongated. Additionally, a very strong bond slip interface was also included to resist the slip between the reinforcing bar and the nut at the bottom of the specimen in Bond 2. The slip strength property for this strong bond slip Bond 2 was taken to be 100 MPa which is strong enough to resist slip beyond the yield strength of the reinforcing bars used. The strength parameters for assigning bond-slip behavior have been calibrated appropriately so as to represent the experimental observations.

5.3.1.3 Reinforcing bar

Steel reinforcements were represented by truss elements with material properties represented by suitable hardening parameters for JIS SS400 steel bars of diameter 3 mm representing the threaded portion of the bar. Isotropic hardening was assumed with hardening parameters as shown in Fig. 5.8(a) with yield stress of 180 MPa adopted with Young's modulus E_{st}=200GPa. The tangent modulus of the second branch was taken to be 0.4% of the initial modulus up to maximum stress of 400 MPa and almost perfectly plastic beyond this stress level.

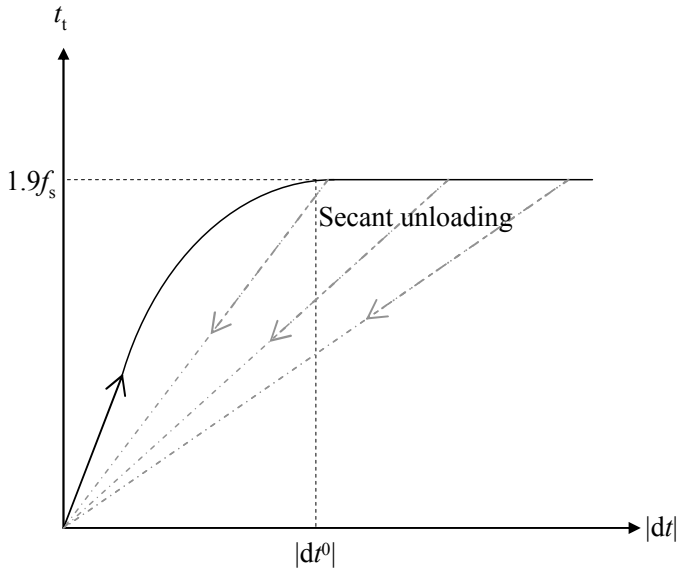

Figure 5.7: Traction stress versus displacement plot with secant unloading for bond slip interface.

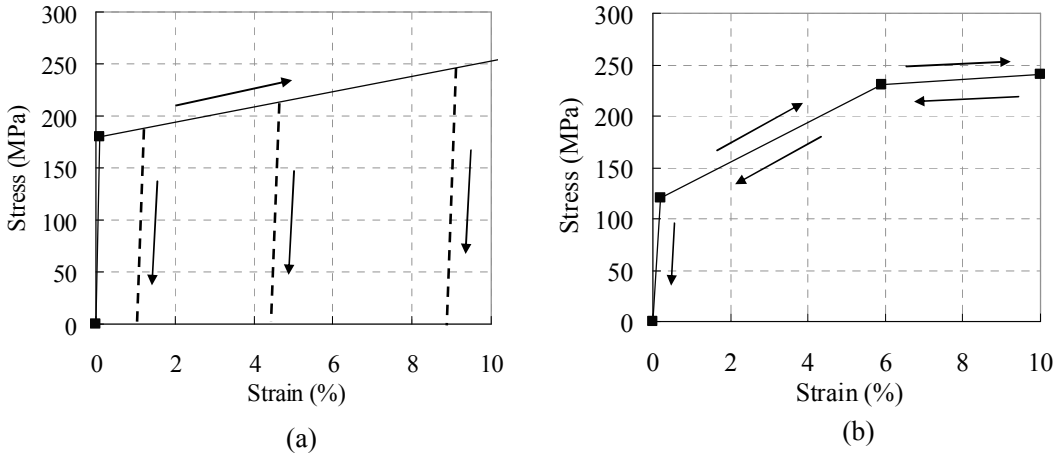

Figure 5.8: Constitutive models for the reinforcing bars: (a) steel bar, (b) SMA bar.

SMA bars were also represented by truss elements with its superelastic property incorporated by assuming tri-linear elastic constitutive model shown in Fig. 5.8(b). The initial modulus for SMA was E_{SMA}=60 GPa up to yield stress of 120 MPa. The tangent modulus of the 2nd branch was taken to be 3% of initial tangent modulus up to stress of 230 MPa. And beyond this stress level, very low tangent modulus of 310 MPa was adopted.

It was observed from the experiments that portions of the reinforcing bars where strain gage were attached did not necessarily yield. It was inferred from this result that the behavior of the reinforced specimens was controlled by yielding concentrated at the threaded portions of the reinforcing bars. To simulate this behavior, reduced section truss elements of 3 mm diameter were used at the bottom and top portion of the reinforced specimens. Also in case of the SMA-RM model, reduced section truss element was used at the 3rd mortar level from the bottom where a coupler, or a long nut, was attached. The length of the reduced section reinforcing bar was kept at 10 mm for the bottom threaded portion, and 5 mm for the threaded portion where the coupler was attached. These values were determined to make the mesh as simple as possible. The threaded portions for the SMA-RM model are shown in Fig. 5.6. One threaded portion was located at the bottom where the nut was connected. And the other portion

was located at the 3rd mortar level from the bottom at the coupler's location. Note that, in case of the ST-RM model, no coupler was used and that threaded portions were located only at the bottom and top of the brick wall specimen.

5.4 QUASI-STATIC CYCLIC TEST PROGRAM

5.4.1 Test setup and loading program

Fig. 5.9 shows the test arrangement for static test. All the specimens were subjected to quasi-static cyclic loading using a hydraulic shaking table. As shown in Fig. 5.9(a), the lower concrete support was fixed to the shaking table using angle steel members, and a steel plate was fixed to the upper concrete block support to apply a constant vertical load. The mass of the steel plate was 145 kg. The average compressive stress at the base of the brick wall specimen was 0.08 MPa. Two roller supports were provided at the both sides of the steel plate as shown in Fig. 5.9(b). The support allowed vertical translation and rotation of the steel plate but did not allow horizontal translation. Displacement controlled cyclic ramp load was given by the shaking table so that the amplitude θ_a of the rotation angle of the wall specimen as shown in Fig. 5.9(a) was equal to 1/700, 1/350, 1/175, 1/116, 1/87, 1/70, 1/58, 1/44, 1/35 and 1/18 radian. The base displacement was applied at an average rate of 0.2 mm/sec to realize quasi-static loading. Laser displacement transducers were used to acquire displacement records during the experiment. Cross marks in Fig. 5.9(c) show the locations where displacements were measured. Strain data of reinforcing bars were measured using strain gages at the locations shown in Fig. 5.9(c).

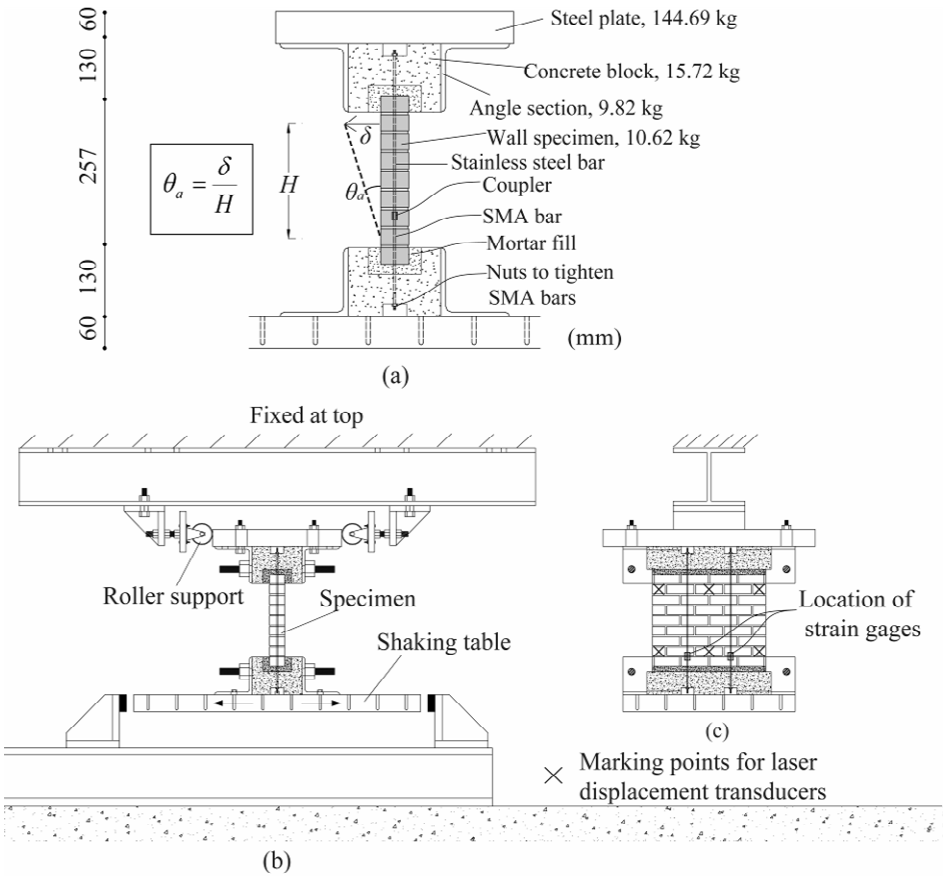

Figure 5.9: Out-of-plane test set-up on shaking table: (a) test set-up, (b) front view showing laser displacement cross-marks, (c) specimen with its major components.

5.4.2 Experimental observation

5.4.2.1 URM specimen

The relationship between the horizontal resisting force and the rotation angle for the URM specimen is shown in Fig. 5.10. Fig. 5.11 shows the deformed shape and the bed joint cracking for the URM specimen. As seen from Fig. 5.10, the load-deformation response showed two distinct stages; the first was linear pre-cracking stage, and this was followed by the second stage with a descending curve. Fig. 5.10(a) shows the response when θ_a<1/70 radian. The pre-cracking response was almost linear until the peak force was observed. After the peak, the formation of the first crack was observed at the 1st mortar joint level from the bottom. The peak force represents the strength

associated with the tensile cracking of the bed mortar joint. Fig. 5.10(b) shows the response including the range θ_a>1/70 radian. The post-cracking descending curve was nearly linear, where the deformation continued to increase while the resisting force decreased up to the loss of horizontal resisting force.

The post-cracking response of the URM specimen can be reasonably predicted by a rigid body assumption [27]. The horizontal resistance F_C^U, assuming that the wall was cracked at the bed joint at the 1st mortar level from the bottom, is given by,

$$F_C^U = \frac{\left(\frac{t}{2} - h\theta\right)mg}{(h + t\theta)} \tag{5.3}$$

where t is the wall thickness, h is the height of the position of action of horizontal force measured from the 1st mortar joint level, θ is the rotation angle of the wall, m is the total mass of the steel plate, the upper concrete block, and the steel angle member, and g is the gravity acceleration. From Eqn. 5.3, it is clear that the critical rotation angle θ_s for the loss of horizontal resistance is expressed as $\theta_s = t/(2h)$, which is around 0.06 radian. The dotted line in Fig. 5.10 shows that Eqn. 5.3 predicts the post-cracking behavior reasonably well. As seen from the figure, after the first cracking of the wall, the force quickly dropped off and approached the prediction by the rigid body assumption.

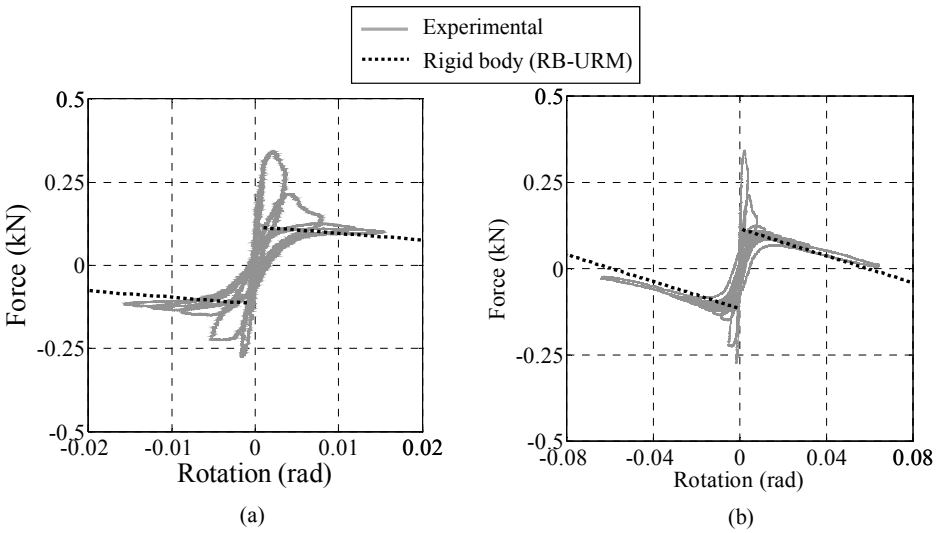

Figure 5.10: Force-rotation relation for the URM specimen: (a) θ_a <1/70 radian, (b) θ_a >1/70 radian.

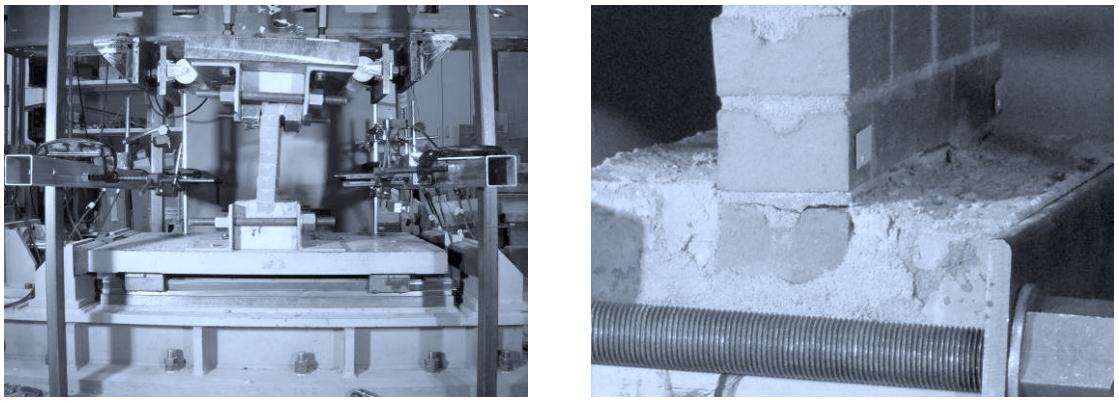

(a) (b)

Figure 5.11: Deformed shapes for the URM specimen: (a) deformed shape, (b) bed joint cracking.

5.4.2.2 ST-RM specimen

Fig. 5.12 illustrates the resisting force-rotation angle relationship. As shown in Fig. 5.12, the horizontal resisting force-rotation angle relationship of the ST-RM specimen was characterized by three distinct stages: (1) the pre-cracking stage, for θ_a <1/175 radian, (2) the post-cracking stage, for 1/175< θ_a <1/58 radian, and (3) the large

deformation stage, for θ_a>1/58 radian. First, for θ_a<1/175 radian, similar to the URM specimen, almost linear pre-cracking stage was seen with the peak horizontal resisting force corresponding to the bed joint tensile strength as shown in Fig. 5.12(a). With the completion of the pre-cracking stage, the ST-RM specimen showed significant deformation with no real increase in the resisting force as seen in Fig. 5.12(b). Large difference between the un-cracked and cracked wall stiffness resulted in a continuous decrease in the resisting force measured. Fig. 5.12(b) also shows typical pinching phenomenon for the ST-RM specimen in the large deformation range. Detailed discussion on this issue is given later in Section 5.4.3.2.

The post-cracking response of ST-RM specimen is compared with a rigid body assumption as shown in Fig. 5.12(b). The horizontal resistance F_C^{ST} obtained from the rigid body model, assuming that the wall was cracked at the bed joint at the 1st mortar level from the bottom, is given by,

$$F_C^{ST} = \frac{\left(\frac{t}{2} - h\theta\right)mg + F_p^{ST} \times \frac{t}{2}}{(h + t\theta)} \tag{5.4}$$

where F_p^{ST} is the strength of the reinforcing steel bar. The bar strength F_p^{ST} was computed using the yield stress of 210 MPa and the effective sectional area of the threaded portion of the steel bar, where the diameter was assumed to be 3 mm. The experimental response and the prediction by the rigid body assumption agree reasonably well as shown in Fig. 5.12(b).

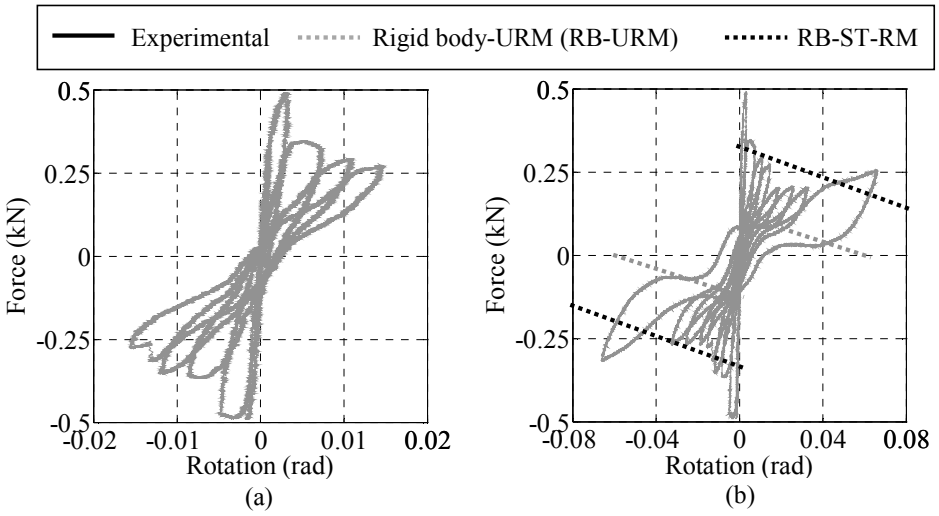

Figure 5.12: Force-rotation relation for the ST-RM specimen: (a) θ_a <1/70 radian, and (b) θ_a >1/70 radian.

5.4.2.3 SMA-RM specimen

As shown in Fig. 5.13, the horizontal resisting force-rotation angle response of the SMA-RM wall specimen showed behavior with three different stages. The pre- and post-cracking stages were similar to those of the ST-RM specimen. On the other hand, the large deformation stage showed major distinct features as compared to that of the ST-RM specimen. During the unloading phase, the behavior was particularly different with no pinching phenomenon. Also during the loading phase, constant restoring force was observed beyond the rotation angle of 0.04 radian. More details on these features are discussed later in Section 5.4.3.3.

The post-cracking response of SMA-RM specimen is also compared with the prediction by the rigid body assumption as shown in Fig. 5.13(b). Similar to the ST-RM specimen, the horizontal resistance obtained from the rigid body assumption is given by,

$$F_C^{SMA} = \frac{\left(\frac{t}{2} - h\theta\right)mg + F_p^{SMA} \times \frac{t}{2}}{(h + t\theta)} \tag{5.5}$$

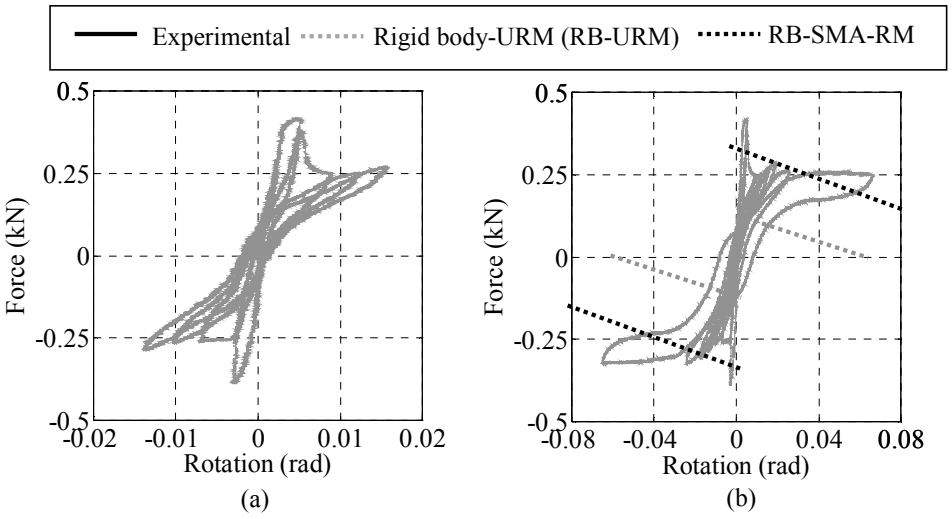

Figure 5.13: Force-rotation relation for the SMA-RM Specimen: (a) θ_a <1/70 radian and (b) θ_a >1/70 radian.

where F_p^{SMA} is the strength of the reinforcing SMA bar assuming the maximum stress of 210 MPa. Here, 3 mm diameter of effective cross sectional area of the SMA bar is taken for representing the threaded portions. The results obtained from the experimental observation agree reasonably well with the rigid body assumption as shown in Fig. 5.13(b).

5.4.3 Finite element results

5.4.3.1 URM Specimen

Fig. 5.14 shows the horizontal resisting force-rotation angle plot for the experimental as well as numerical observations. The plots show good comparable response. The FE response simulated well the two distinct phases; the pre- and post-peak stages. Simulating the decrement in the resisting force in the post-peak stage was possible by including geometric nonlinearity. The numerical results also agreed well with the theoretical rigid body assumption as shown in Fig. 5.14 (b).

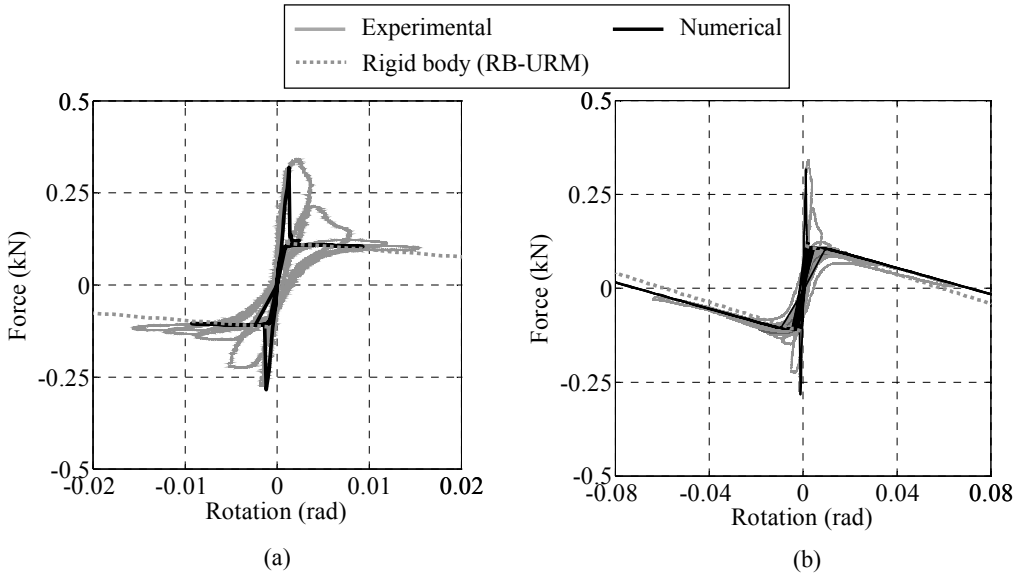

Figure 5.14: Comparison for the URM specimen: (a) θ_a <1/70 radian, and (b) θ_a >1/70 radian.

5.4.3.2 ST-RM Specimen

Fig. 5.15 shows the comparison of the responses of the ST-RM specimen. In Figs. 5.15(a) and (b), the pre- and post-peak behavior of the FE model matched the experimental results and the theoretical predictions reasonably well. The initial peak strength, attributed to tensile cracking of mortar bed joint, for the FE model was in the lower side. Large variability in the tensile strength seems to be the reason of the lower prediction. The FE results predicted reasonably well the more important post-cracking phase as seen in Figs. 5.15(a) and (b). In Fig. 5.15(b), pinching phenomenon was clearly observed for the FE results during unloading phase as well. Figs. 5.15(c) and (d) show the comparison of the strain history prediction with the strain gage data for θ_a <1/70 radian and θ_a >1/70 radian respectively. No significant residual deformation was observed from the experiment with the exception of the last cycle, where residual strain of 0.06% was recorded. Numerical results in Figs. 5.15(c) and (d) agreed well with the experimental observations with the exception of the last 2 cycles. As shown in shown in Fig. 5.15(e), the portion of reinforcing bar where the strain gage measurement was made primarily worked in its elastic range while yielding

concentrated at the threaded portion of the reinforcing bars as shown in Fig. 5.15(f). Note that, in Fig. 5.15(e), the experimentally observed bar force $F_{\mathrm{p}}^{\mathrm{RM}}$ was obtained inversely by Eqn. 5.6 making the rigid body assumption and using the horizontal restoring force F_{R} measured.

$$F_{\mathrm{p}}^{\mathrm{RM}} = \frac{2}{t} F_{\mathrm{R}} (h + t\theta) - \left(1 - \frac{2h}{t}\theta\right) mg \tag{5.6}$$

Fig. 5.16 illustrates the mechanism of the pinching phenomenon. Three different loading instants are shown in Fig. 5.16(a) represented by Point B at $\theta = 1/18$ radian, Region A, and Point C at $\theta = -1/18$ radian. Up to Point B, with increasing the rotation angle, the horizontal resisting force also increased as shown in Fig. 5.16(a). With the release of the load from Point B, unloading took place almost linearly up to the rotation angle of 0.04 radian. From this point on, pinching phenomenon in the wall was observed. In Region A, rocking resistance due to gravity was observed, which can be represented by the rigid body assumption for the URM model. The reinforcing bars were allowed to deform almost freely at the bottom of the wall specimen which resulted in the rocking response observed. The deformed shape of the numerical model, as shown in Fig. 5.16(c), shows the crack occurring at the nut interface. In the negative loading towards Point C, the gap between the nut and the concrete block closed, and the crack was initiated at the 1st mortar joint level as shown in Fig. 5.16(d). Afterwards, the horizontal resisting force increased with increasing the rotation angle up to Point C. To summarize, it can be seen from the numerical results that the whole mechanism during the loading history was primarily governed by the plastic residual deformation concentrated in the threaded region of the steel reinforcing bar.

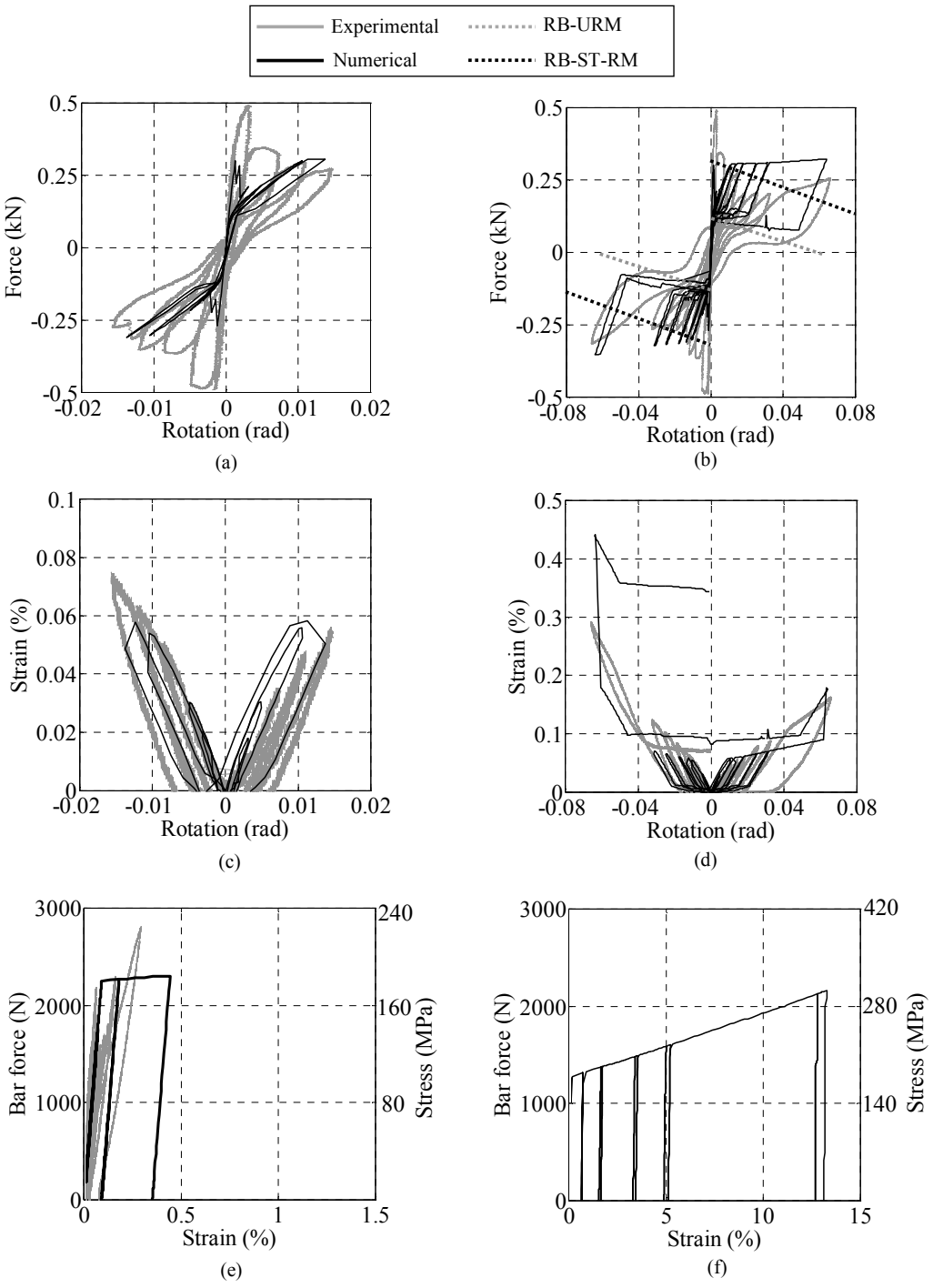

Figure 5.15: Comparison for the ST-RM specimen: (a) force-rotation relation for θ_a<1/70 radian, (b) force-rotation relation for θ_a>1/70 radian, (c) strain-rotation relation for θ_a<1/70 radian, (d) strain-rotation relation for θ_a>1/70 radian, (e) bar force-strain relation at strain measured portion, and (f) bar force-strain relation at threaded portion.

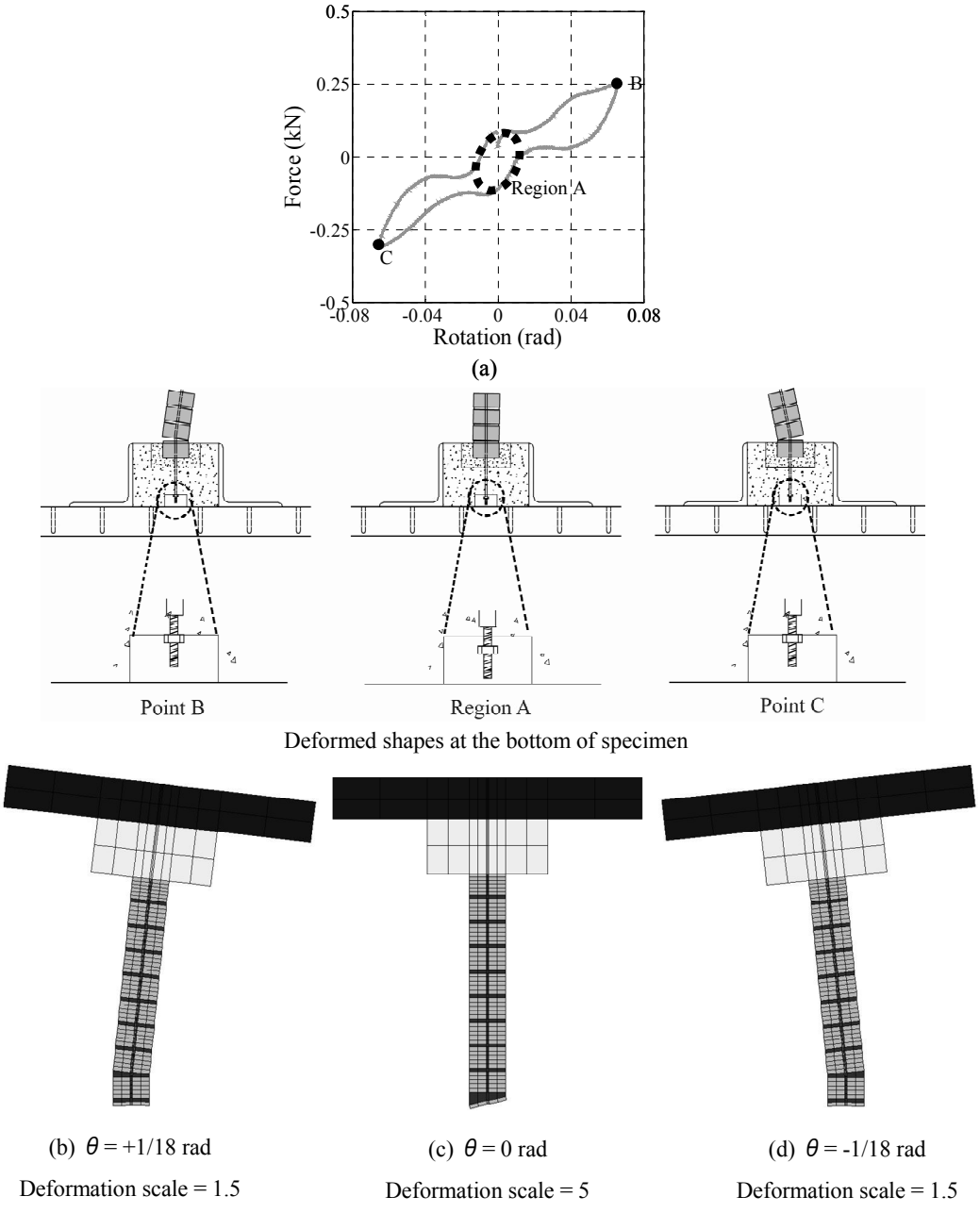

Figure 5.16: Mechanism observed for the ST-RM specimen: (a) typical distinct phases in the force rotation angle history (10th cycle), (b) deformed shape at θ_a=+1/18 radian, (c) deformed shape at θ_a=0 radian, (d) deformed shape at θ_a=-1/18 radian.

5.4.3.3 SMA-RM specimen

The horizontal resisting force-rotation relations obtained from the FE model are

compared with the experimental results and the theoretical predictions as shown in Figs. 5.17(a) and (b). Both plots show comparable pre- and post-peak responses. Fig. 5.17(b) shows constant horizontal resisting force for θ >0.04 radian representing yielding of the SMA bars. During the subsequent unloading, due to superelastic property of SMA bars, comparatively stable response was observed with no pinching phenomenon. Figs. 5.17(c) and (d) show the comparisons of the strain-rotation angle relationship. The tri-linear elastic model adopted for the SMA bar represented the experimentally observed strain history reasonably well. The strain gage data observed experimentally and computed numerically both exhibited no residual strain in any of the loading cycles. In Fig. 5.17(e), the experimentally observed force in the SMA bar was obtained by Eqn. 5.6. From the FE computation, the strain observed at the threaded portion of the SMA bar showed clear sign of yielding beyond 0.2% strain as shown in Fig. 5.17(f).

Fig. 5.18 shows the response observed at the bottom of the SMA-RM model obtained through the numerical simulation. Here, the results are shown for three different instants of loading, θ =1/18 radian, θ =0 radian and $\theta = -1/18$ radian. For θ =1/18 radian, the out-of-plane loading caused cracking at the 1st mortar joint level from the bottom as shown in Fig. 5.18(a). With the initiation of unloading phase, the resisting force decreased gradually with the decrement in rotation angle with no sign of pinching due to absence of residual deformation of the SMA reinforcing bar. The crack at the nut interface was not seen at the instant of θ =0 radian as shown in Fig. 5.18(b). In the negative loading, for $\theta = -1/18$ radian, again the crack at the 1st mortar joint level from the bottom was observed as shown in Fig. 5.18(c).

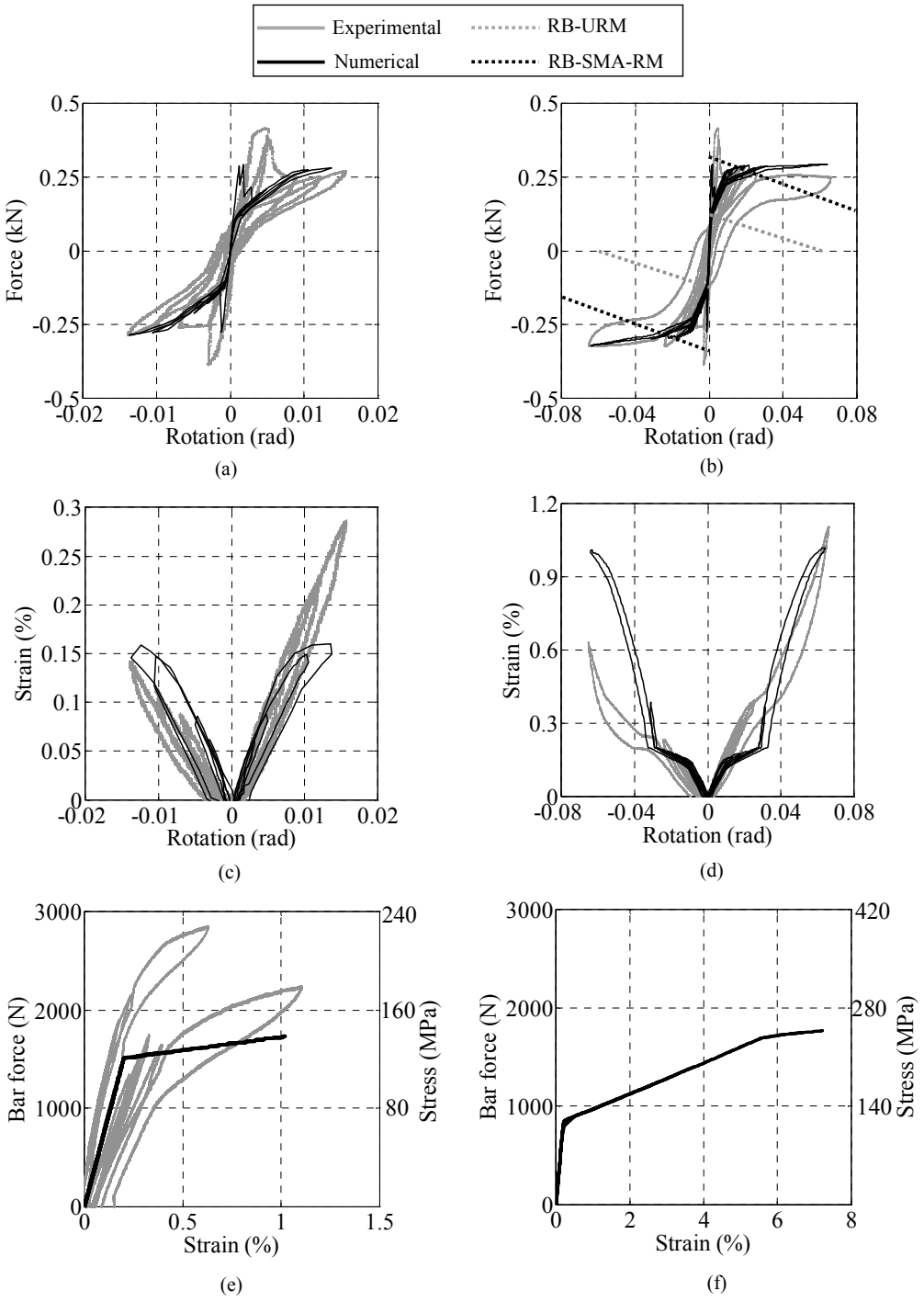

Figure 5.17: Comparison for the SMA-RM specimen (a) force-rotation relation for θ_a<1/70 radian, (b) force-rotation relation for θ_a>1/70 radian, (c) strain-rotation relation for θ_a<1/70 radian, (d) strain-rotation relation for θ_a>1/70 radian, (e) bar force-strain relation at strain measured portion, and (f) bar force-strain relation for threaded portion.

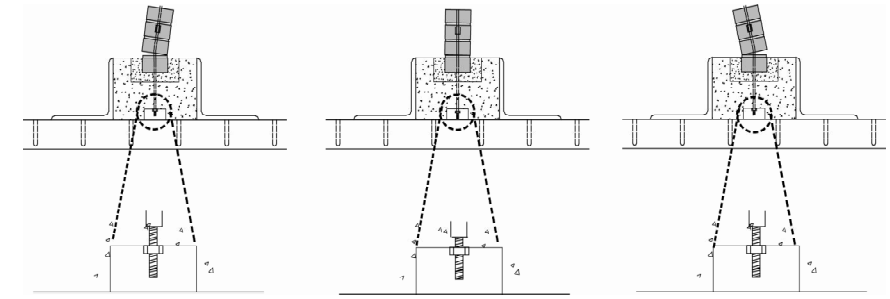

Deformed shapes at the bottom of specimen

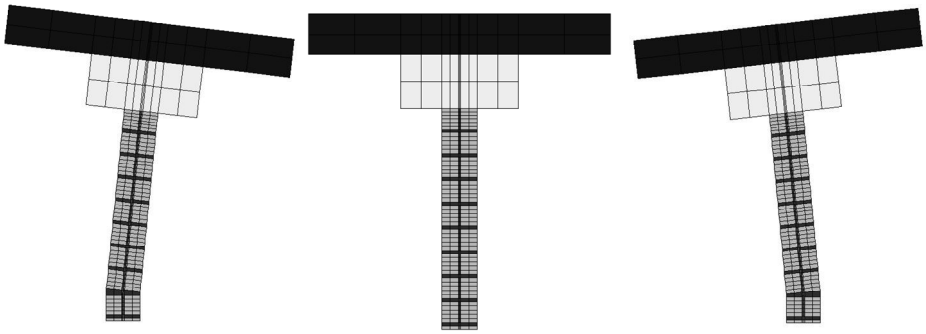

(a) θ = +1/18 rad
Deformation scale = 1.5

(b) θ = 0 rad
Deformation scale = 5

(c) θ = -1/18 rad
Deformation scale = 1.5

Figure 5.18: Deformed shapes for the SMA-RM specimen: (a) θ_a =+1/18 radian (b) θ_a =0 radian, and (c) θ =-1/18 radian.

5.4.4 Discussions

As shown in the previous sections, the behavior of the ST-RM and SMA-RM specimens are considerably different. Nevertheless, the increments in strength and ductility are almost similar in both specimens. And the differences in the response of the specimens are not very large especially in the small deformation range. As a result, the strengths of the use of SMA reinforcing bars over steel bars may be argued. This section discusses this issue in detail, and also discusses some other issues concisely.

As described in the preceding sections, reinforcing bars were not fixed and allowed to deform almost freely at the bottom of the wall specimen in the present experiment, while in actual practice reinforcing bars are usually fixed at the bottom. As a result, the experimental observations in the present study are different in some points from those

in more practical settings [7,28]. When reinforcing bars are fixed at the bottom of the wall as shown in Fig. 5.19, pinching is caused by inelastic elongation of reinforcing bars around the crack at the 1st bed joint. In this case, the crack at the bed joint does not close and the reinforcing bar works as a pin support when the wall returns to initial straight position as shown in Fig. 5.19(b). The stiffness around the initial position becomes nearly zero after yielding of reinforcing bars. On the other hand, when reinforcing bars are not fixed as in the present experiment, the crack at the 1st bed joint closes when the rotation angle returns to zero as shown in Fig. 5.16(c). This leads to rocking resistance due to gravity as depicted in Fig. 5.16(a).

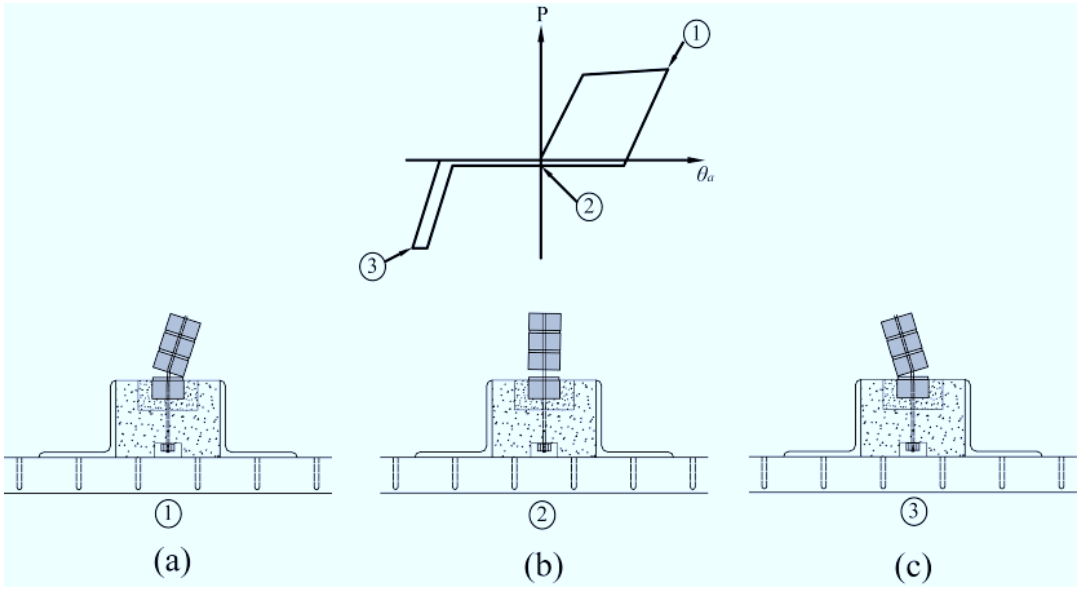

Figure 5.19: Schematic representations for mechanisms of steel reinforced specimens with reinforcing bars fixed at the bottom at: (a) maximum positive loading post yield of reinforcing bar, (b) initial straight position, and (c) maximum negative loading.

In order to examine the response of reinforced walls to show the above behavior in a more practical setting, FE models were developed wherein reinforcing bars are fixed at the bottom of the wall specimen. SMA-RM^{FB} and ST-RM^{FB} represent the corresponding SMA reinforced and steel reinforced FE models where reinforcing bars are fixed at the bottom of the wall specimen. Comparisons between the non-fixed and fixed models in Fig. 5.20 show contrasting characteristics. As shown in Figs. 5.20(a) and (c), the tangent stiffness around the initial position becomes nearly zero in case of ST-RM^{FB} model, while it does not in case of ST-RM model. The difference can be clearly seen even in the small deformation range. On the other hand, as shown in Figs 5.20(b) and (d), the stiffness around the initial position for SMA-RM and SMA-RM^{FB} is always high and similar regardless of the condition of fixing the reinforcement at the bottom.

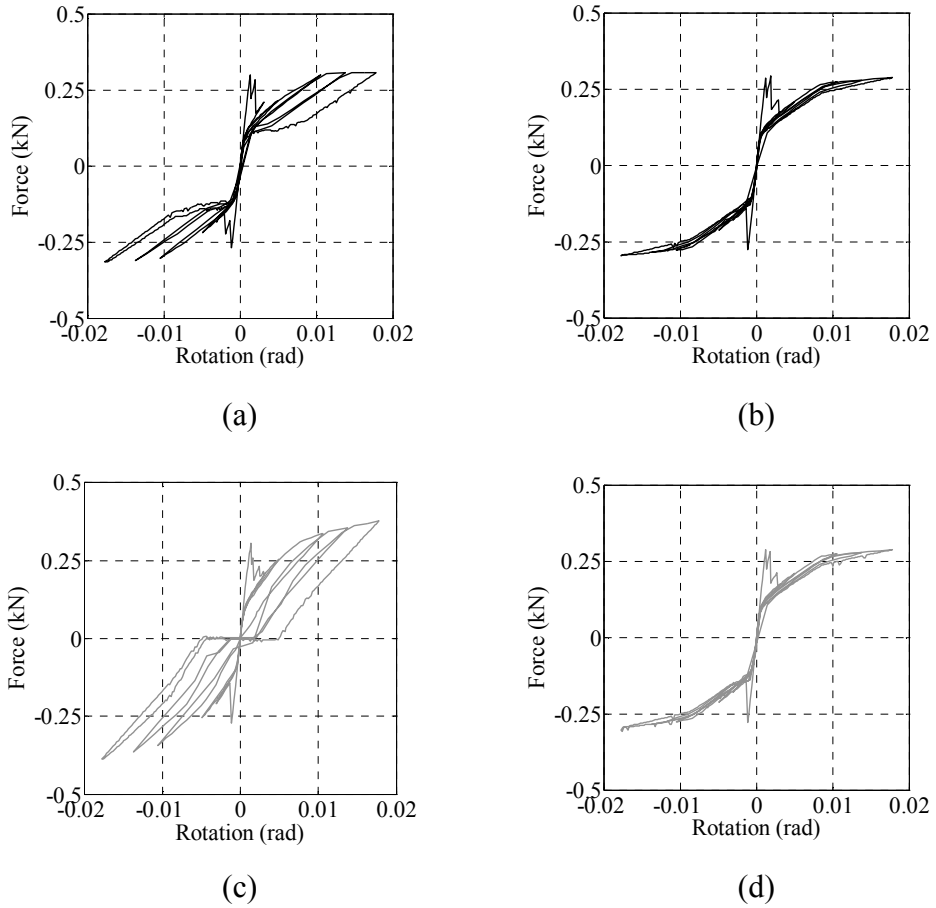

Figure 5.20: Force rotation relation for the non-fixed and fixed base models: (a) ST-RM, (b) SMA-RM, (c) ST-RM^{FB}, and (d) SMA-RM^{FB}.

Fig. 5.21 shows comparisons of typical post yield cyclic responses, and Fig. 5.22 illustrates the FE deformed shapes for all the models at the initial straight position at the end of corresponding post yield cycles of Fig. 5.21. In Fig. 5.21(a), the difference between responses of ST-RM and ST-RM^{FB} models in their post yield behavior can be clearly seen with ST-RM model showing rocking response around the initial position with crack at the nut interface as shown in Fig. 5.22(a). ST-RM^{FB} model in Fig. 5.22(c) shows crack at the mortar bed joint as depicted schematically in Fig. 5.19. On the other hand SMA-RM and SMA-RM^{FB} models show no significant difference in their force-rotation relation as shown in Fig. 5.21(b) and both show no cracks with the release of loads at the initial straight position as illustrated in Figs. 5.22(b) and (d) respectively. These figures clearly demonstrate the effectiveness of SMA bars over steel bars as reinforcing elements in a more practical setting.

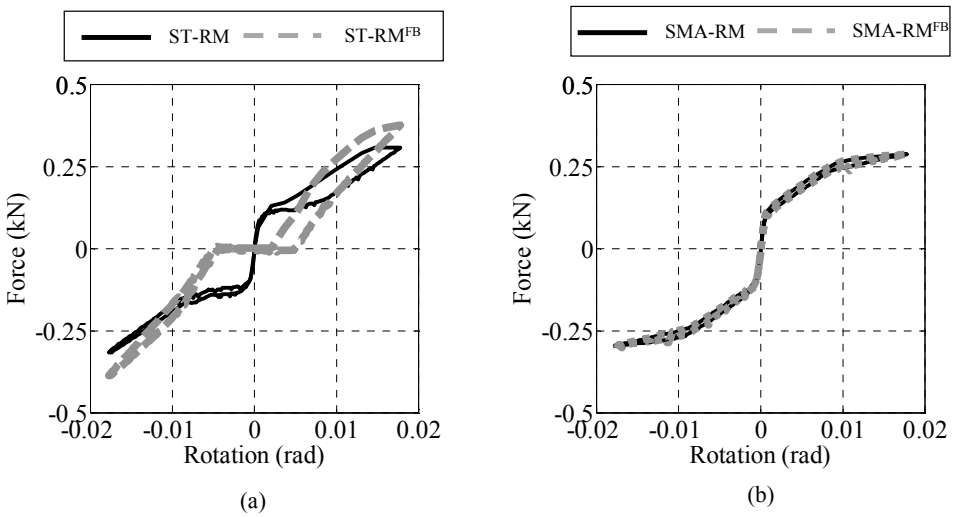

Figure 5.21: Comparison between typical post yield cycle for the non-fixed and fixed base models: (a) ST-RM and ST-RM^{FB}, and (b) SMA-RM and SMA-RM^{FB}.

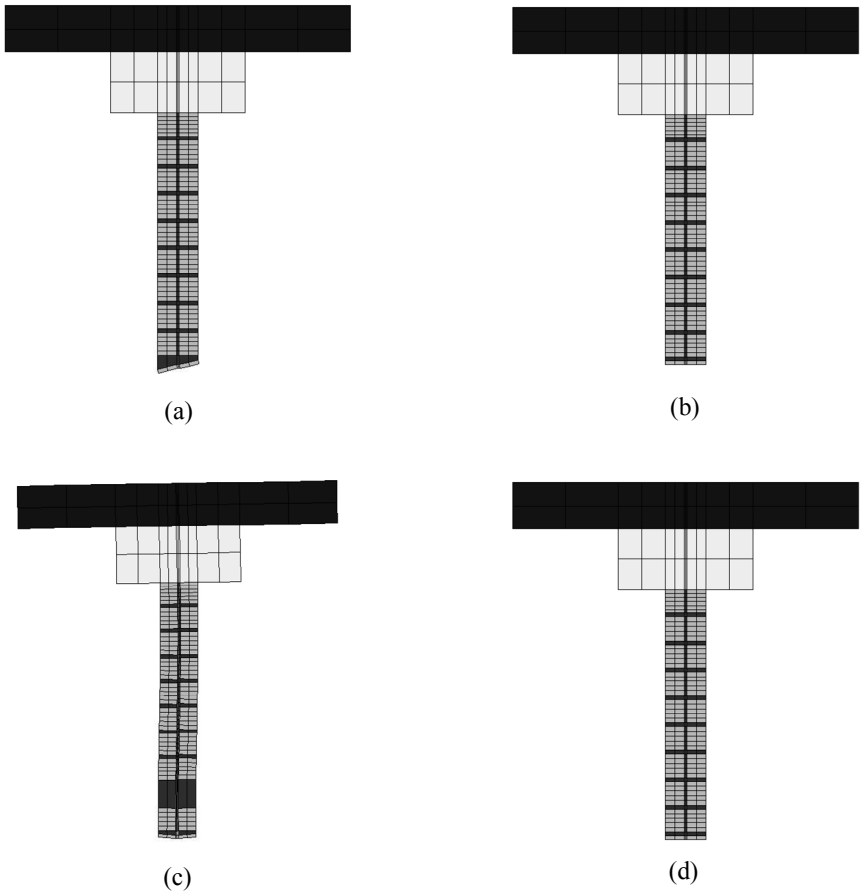

Figure 5.22: FE deformed shapes around initial equilibrium position of θ_a=0 radian for the non-fixed and fixed base models: (a) ST-RM, (b) SMA-RM, (c) ST-RM^{FB}, and (d) SMA-RM^{FB}.

5.5 DYNAMIC LOADING TEST PROGRAM

5.5.1 Test set-up

The test specimen set-up is similar to the one adopted for static test as shown in Fig. 5.23 with omission of any lateral supports at the top with brick wall specimen fixed to the upper concrete block. The total mass at the top of the specimen (involving steel plate, angle steel members and concrete block) and the reinforcing bars were designed to cause the collapse within the maximum input ground acceleration capacity of the shaking table. The reinforcing bars were designed so that they yield at the critical

section when the inertial force of 0.2*mg* is applied to the top of the specimen. Here, *m* is the total mass of the steel plate, the upper concrete block, and the steel angle member and *g* is the gravity acceleration. The nominal yield stress of 240 MPa was assumed in design.

5.5.2 Instrumentation and input ground motion

The laser displacement transducers were used to acquire the displacement records during the experiment. The cross marks in Fig. 5.23 show the locations where displacements were measured. Accelerometers were set at the top, center and bottom of the wall specimen. Accelerations of the shaking table and the steel plate at top were also measured.

Reference ground motion of scaled El-Centro NS earthquake excitations were adopted to study the dynamic response properties of the specimens ranging from elastic state low level excitation to ultimate state severe excitation. The shaking table used is driven by displacement input motion. Each test was initiated with two runs of 1 mm amplitude 20 cycle sine wave excitation to study the elastic dynamic response properties.

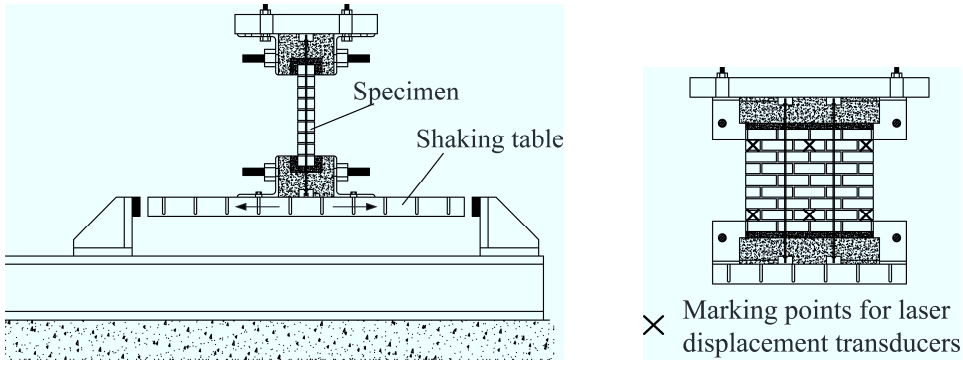

Figure 5.23: Out-of-plane test set-up on shaking table: (a) test set-up and (b) front view showing laser displacement cross-marks.

To meet the limited capacity of shaking table, the actual El-Centro NS earthquake wave excitation was reduced properly so that the maximum velocity (v_{max}) is 5 kine. Reduction on excitation parameters like displacement as well as velocity was essential to perform the test on the available shaking table. Care has been taken so that the reinforced wall specimen yields during the given excitation level. Table 5.2 shows the sequence of earthquake loading with their respective peak ground accelerations (PGAs) starting from low level excitation of 0.19*g* up to severe excitation of 1.04*g*. Fig. 5.24(a) shows the experimentally input displacement time history represented by RUN 2 or 2* in Table 5.2. Fig. 5.24(b) shows the input acceleration that was observed on the shaking table corresponding to adjoining displacement time history. Fig. 5.25 compares the acceleration response spectra at 5% damping for experimentally input excitations from RUN 2 to RUN6.

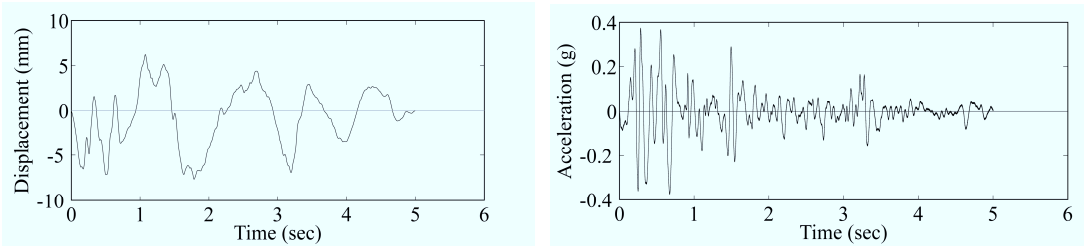

(a) (b)

Figure 5.24: Details on earthquake excitation used: (a) Displacement time history of earthquake excitation, (b) Acceleration time history of earthquake excitation.

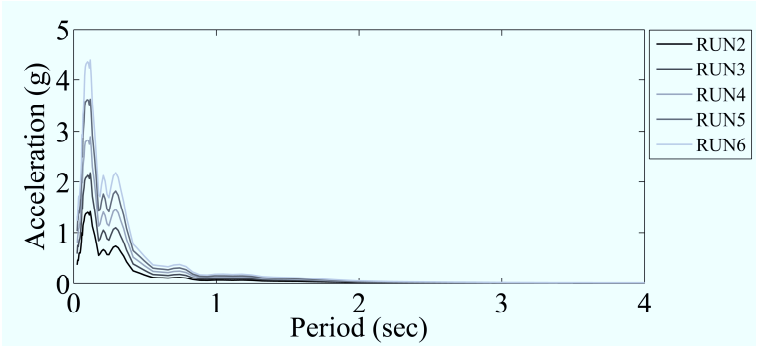

Figure 5.25: Comparison of response spectra at 5% damping for input excitation runs.

5.5.3 Experimental observations

5.5.3.1 Visual observations for earthquake ground motion

Table 5.2 summarizes the visual observations under earthquake ground excitation. U, ST and SMA indicate the unreinforced, steel-reinforced and SMA-reinforced specimens respectively. The numbers following these characters represent the number of specimens for each type. Signs of first visible cracking were observed for PGA 0.37*g* at RUN2 and RUN2* as shown in Table 5.2.

For URM specimens, primarily cracking originated from the bottom of the wall at the 1st mortar joint. Both the URM specimens collapsed with brittle failure mechanism at earthquake excitation with PGA 0.58*g* at RUN3.

For earthquake excitations, the ST-RM specimens exhibited rocking response but with visibly large residual deformations. For ST1 specimen, rocking response was observed for PGA up to 0.94*g* but residual inclination at the end of RUN5 was clearly visible. With initiation of RUN6 at PGA of 1.04*g*, ST1 specimen collapsed due to instability, not able to sustain the progressively increasing P-Delta moment. ST2 specimen showed similar response to ST1 specimen. Complete collapse of the wall was not seen, but it was visibly very unstable at the end of RUN6* with large residual inclination of the wall.

For the SMA-RM specimens, stable rocking response was observed even for the high level of base excitations with very small residual deformation observed. SMA2 specimen showed stable rocking response throughout the test and did not collapse even at maximum shaking table excitation RUN6*. However, SMA1 collapsed at RUN6* with PGA of 1.04g. The observed collapse mode was distinctly different from the ones seen for URM and ST-RM specimens. The fractured mortar joint belonged to relatively upper part of the wall specimen as shown in Fig. 5.26. Very strong rocking of the top steel plate was visibly seen possibly induced by higher mode vibrations.

Table 5.2: Earthquake wave excitation test sequence and visual observations for each specimen.

S. No.	Code	PGD (mm)	PGA (*g*)	U1	U2	ST1	ST2	SMA1	SMA2
1[a)]	-	1	0.02	NC	NC	NC	NC	NC	NC
2[a)]	-	1	0.02	NC	NC	NC	NC	NC	NC
3	RUN1	3.82	0.19	NC	NC	NC	NC	NC	NC
4	RUN1*	3.82	0.19	NC	NC	NC	NC	NC	NC
5	RUN2	7.22	0.37	NC	CR-1	CR-1	CR-1	CR-2	CR-2
6	RUN2*	7.22	0.37	CR-1	SR	SR	SR	SR	SR
7	RUN3	10.80	0.58	CO-1	CO-1	LR	LR	LR	LR
8	RUN3*	10.80	0.58			LR	LR	LR	LR
9	RUN4	14.55	0.76			LR	LR	LR	LR
10	RUN4*	14.55	0.76			LR	LR	LR	LR
11	RUN5	18.20	0.94			LR	LR	CR-7	CR-6
12	RUN5*	18.20	0.94			LR,RR	LR+RR	LR	LR
13	RUN6	21.84	1.04			CO-2	LR+RR	LR	LR
14	RUN6*	21.84	1.04				LR+RR	CO-1,7	LR

PGD: Peak ground displacement, PGA: Peak ground acceleration, NC: No crack, CR-i: Crack at joint number i from bottom, SR: Slight rocking, LR: Large rocking, RR: Residual rotation, CO-i: Collapse at joint number i from bottom

a) First two runs to study dynamic characteristics involve 20 cycles of 1 mm amplitude sine waves at frequency of 2 Hz

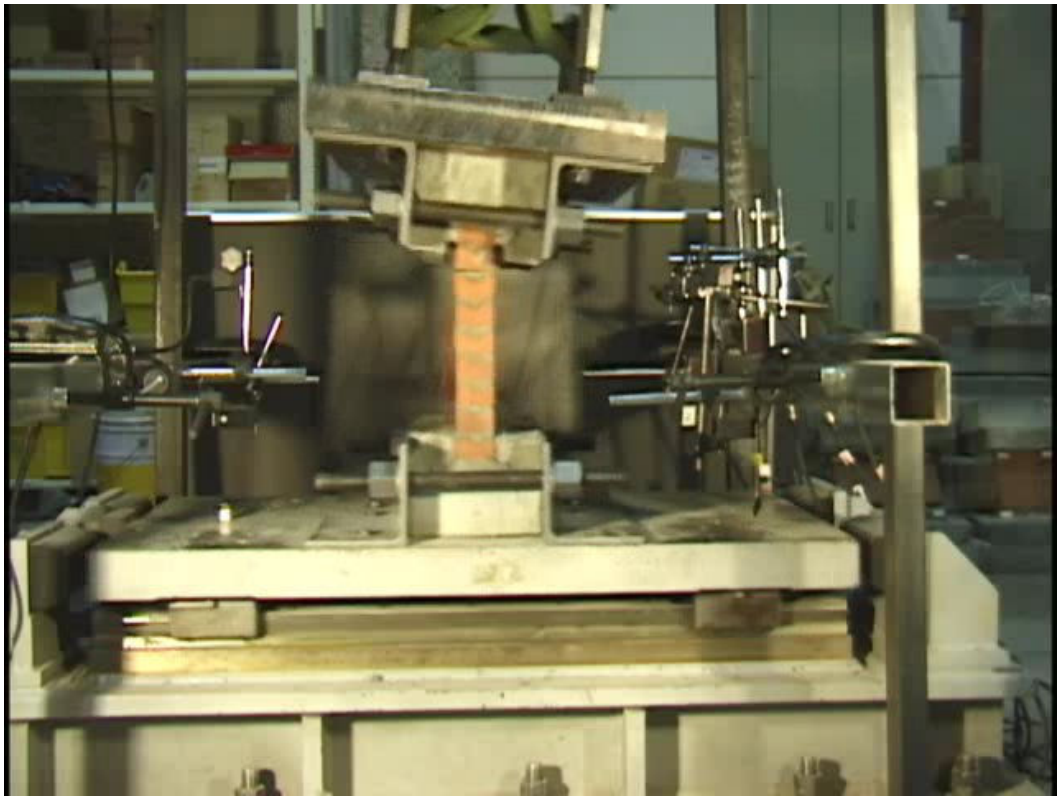

Figure 5.26: Deformed shape of SMA1 specimen showing strong rocking at the top of specimen.

5.5.3.2 Maximum and residual rotation plots

Fig. 5.27 shows maximum and residual rotation plots for all the specimens tested at different excitation levels. The value for the instability limit of the reinforced specimens has been assumed predicting a rigid body assumption given by Eqns. 5.4 and 5.5. The URM specimens experienced instability at the start of RUN3 at PGA around 0.58*g* due to static instability. For ST1 specimens, substantial amount of residual rotation was observed at the end of RUN5* which ultimately caused premature failure of the wall with the advent of high P-Delta effects with the commencement of RUN6. ST2 specimen did not collapse as ST1 but it was equally very unstable and showed large residual deformations at the end of RUN6*. For both the SMA-RM specimens, little residual rotation was observed up to RUN6 with very stable rocking response at such high level of base excitations. Very strong rocking of the top steel plate was visibly seen for SMA1 specimen at RUN6* which ultimately

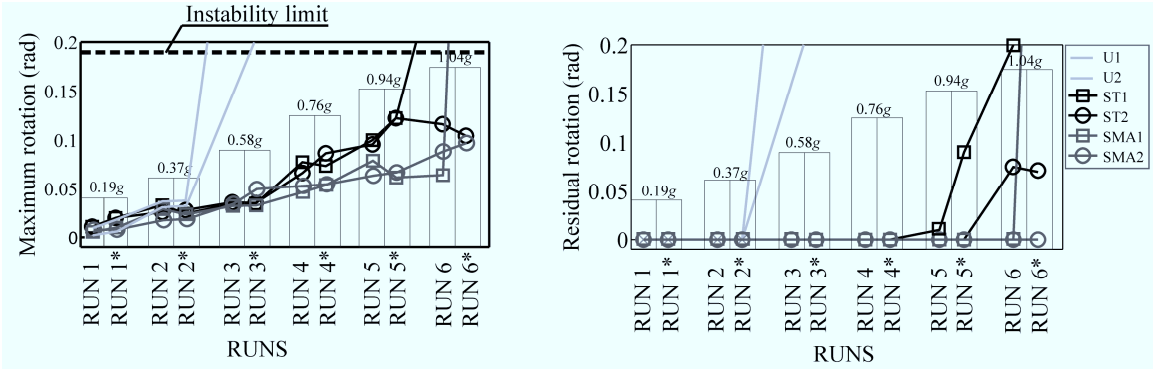

(a) (b)

Figure 5.27: Rotation plots at the end of corresponding earthquake excitation levels: (a) maximum rotation, (b) residual rotation.

resulted in its failure. SMA2 specimen showed no residual deformation and did not collapse even at maximum excitation level of shaking table RUN6*.

5.5.3.3 Acceleration-rotation relationships

Figs. 5.28-5.30 show the acceleration versus rotation plots for U1 (up to RUN2*), U2 (up to RUN2*), ST1 (up to RUN5*), ST2 (up to RUN6), SMA1 (up to RUN6), and SMA2 (up to RUN6) specimens. Here acceleration record measured at top of steel plate was taken. Results are also compared with theoretical assumption predicting a rigid body rotation with the wall cracked at the 1st mortar level from the bottom and is given by,

$$a_c = \frac{\left(\frac{t}{2} - h\theta\right)mg + F_p^R \times \frac{t}{2}}{m(h + t\theta)} \tag{5.7}$$

where a_c is the acceleration of the top portion, t is the wall thickness, h is the height of the position of the center of mass measured form the 1st mortar joint level, θ is the rotation angle of the wall, m is the total mass of the steel plate, the upper concrete block, and the steel angle member, g is the gravity acceleration, and F_p^R is the strength of the reinforcing bar. For both steel and SMA bars, the bar strength F_p^R is computed using yield stress of 300 MPa and diameter equal to 3 mm assuming

threaded potion of the bar. The dotted black lines and solid gray lines in Figs. 5.28 to 5.30 indicated the relationship defined by Eqn. 5.7.

For URM specimens plots have been made for excitation level up to RUN2* as shown in Fig. 5.28. With the initiation of next excitation RUN3, both the specimens collapsed. Good comparison was attained for experimental observation and theoretical prediction for both the specimens.

For ST-RM specimens, acceleration response was dominated by residual strains in steel reinforcing bars used. Both the ST-RM specimens showed signs of yielding at inertial acceleration around 0.25*g* which was intentionally performed during the design of reinforcing bars as discussed in Section 5.5.1. Fig. 5.29(a) shows a definite residual inclination of ST1 specimen towards the left direction mainly due to residual strains in the steel bars. This inclination in turn increased the P-Delta effects which caused the premature collapse of ST1 specimen. For ST2 specimen in Fig. 5.29(b), small residual inclination can be seen. Additionally, clear signs of pinching phenomenon can be observed which is a typical characteristic of such steel reinforced specimen [7,8,20,29]. This was more distinctly observed during the static tests performed by authors as reported in Section 5.4 and Ref.[20]. Fig. 5.30 shows the plot for SMA1 and SMA2 specimens, where both the specimens showed stable hysteretic response with small variation of stiffness around the initial position.

5.5.4 Detailed observations and comparison with finite element model

As shown in Table 5.1, the values obtained from the masonry prism tests showed large deviation in the mortar joint strength measured. To address this effect, sensitivity analysis of the FE models to mortar joint tensile strength was performed with ±50% variation of the mean tensile strength. Here FE models with tensile strength values $0.5f_t$, $0.75f_t$, f_t, $1.25f_t$, $1.5f_t$ where the mean value f_t of mortar tensile strength is 0.47 MPa.

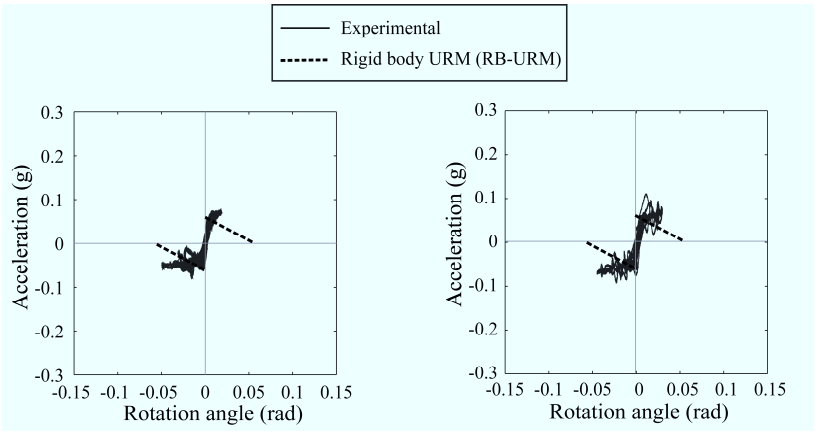

(a) (b)

Figure 5.28: Acceleration-rotation plots for URM specimens: (a) U1, (b) U2.

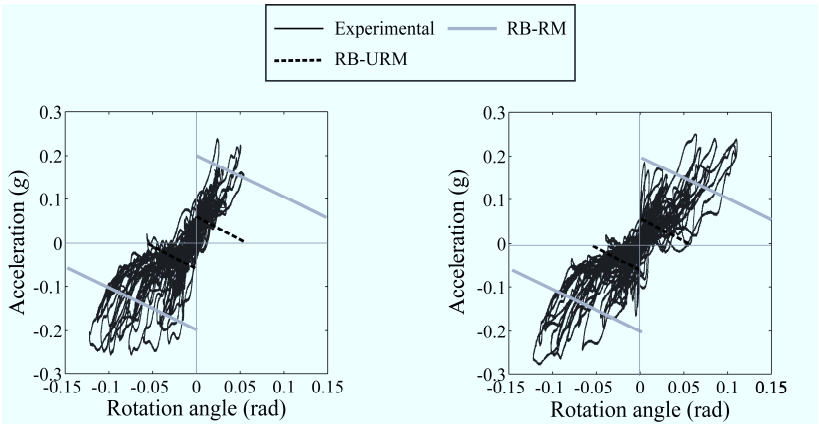

(a) (b)

Figure 5.29: Acceleration-rotation plots for ST-RM specimens: (a) ST1, (b) ST2.

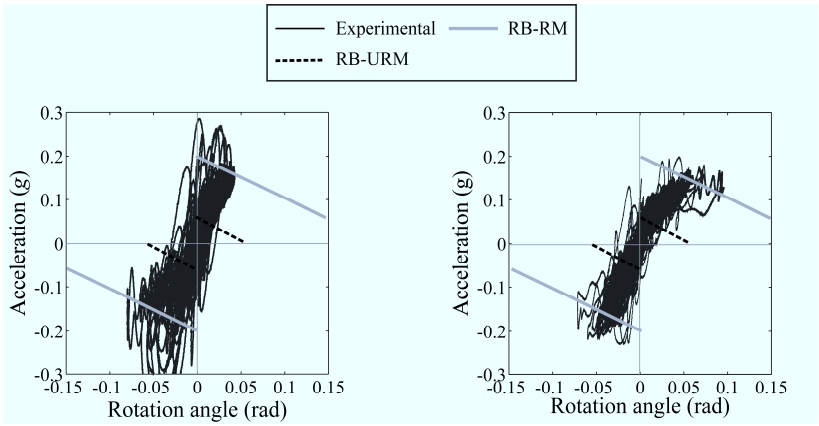

(a) (b)

Figure 5.30: Acceleration-rotation plots for SMA-RM specimens: (a) SMA1, (b) SMA2.

Experimental test set-up for the reinforced specimens involved placing of vertical reinforcing bar inside the specimen with the top and bottom of bars lightly tightened using bolts to the concrete block support. No additional bonding agent was inserted between rounded reinforcing bar and masonry elements apart from the presence of mortar at the locations of mortar joints. Hence, bond interface with extremely low bond strength of 0.1MPa along the length of reinforcing bar was assumed to simulate the experimental condition. Additionally suitable nut crack interface was used to represent the behavior of bolts at the bottom where, post the yielding of steel reinforcement bars the bolts at the bottom shifted down during unloading as reported in Section 5.4 and Ref.[20]. Two extreme scenarios were studied using the FE models – free and fix, one with very low tensile strength and the other with extremely high tensile strength values for nut crack interface. Free model with low tensile strength represented the lower bound response where discrete cracks appeared at the crack interface during unloading post yielding of steel reinforcing bar. Free model characterizes specimen with reinforcing bar free to deform at the bottom. Fix model is the upper bound model with relatively high tensile strength represented specimen with reinforcing bars fixed at the bottom of the wall which is practically more realistic model.

It should be noted that authors' main aim of FE model generation was to predict the overall mechanism of the specimens and not on its exact representation, therefore there exists some discrepancy between experimental and FE results. Additionally, the problem with masonry walls lies in its instability governed by the kinematics and not the strength of walls [30]. Hence, it should be noted that the aim of FE simulation is to predict maximum and residual displacements for the masonry walls and not dwell on exactness of measured quantity versus time exactly.

5.5.4.1 Dynamic characteristics

To determine the natural frequency of vibration and damping ratio for the uncracked

specimens, a 1mm amplitude sinusoidal wave was applied as stated in the preceding section. The approximate values for1st mode natural frequency of vibration calculated for uncracked specimens were as follows, 13.6 Hz for URM, 13.88 Hz for ST-RM and 9 Hz for SMA-RM specimens. The fundamental frequency for the specimens changed with the increase in the level of excitation due to initiation of cracks. Fig. 5.31 shows the change in fundamental frequency for URM, ST-RM and SMA-RM specimens with an increase in input PGA. Comparison has also been made between the results of the FE models. The uncracked FE specimen showed fundamental frequency of 9.18 Hz for FE-U, 10.06 Hz for FE-ST and 10.06 Hz for FE-SMA specimens in 1st mode of vibration.

Damping properties are sensitive to the instantaneous frequency of vibration mainly due to non-linear effects of masonry as reported by Ref.[31]. Hence, a standard procedure for measuring damping like the logarithmic decrement method was not applicable in this case. For this purpose, damping was measured for each individual response half-cycle. Fig. 5.32 shows the correlation of damping ratio (ζ) with frequency from the dynamic tests. In the FE model generation, this frequency dependent damping was approximated by the Rayleigh damping model, $C=\alpha_o M+\alpha_1 K$, with Rayleigh coefficients α_o=1.6 and α_1=2x10^{-5}. Fig. 5.32 shows the comparison of the adopted Rayleigh model and experimental observation for URM, ST-RM and SMA-RM specimens.

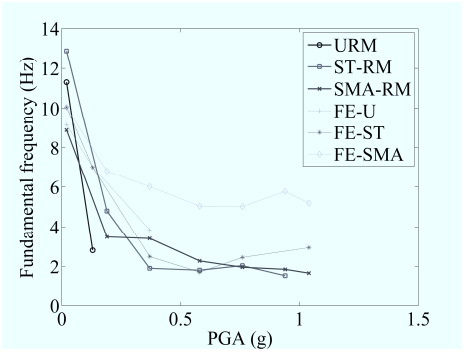

Figure 5.31: Comparison on variation of fundamental frequencies at different excitation levels.

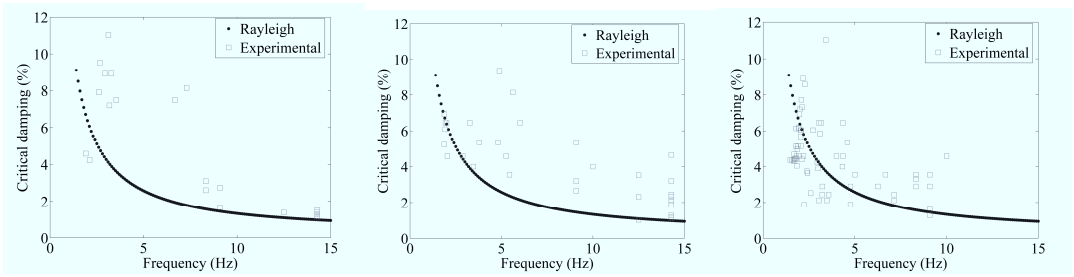

Figure 5.32: Comparison between adopted Rayleigh damping and experimentally observed critical damping at varying frequency: (a) URM, (b) ST-RM, (c) SMA-RM.

5.5.4.2 Deformation angle response at each RUN

ST-RM specimen

Figs. 5.33 and 5.34 show comparison of experimental and FE results plotted for maximum and residual rotation angle observed at different excitation levels for ST-RM specimens in comparison with two strategies adopted for FE model, one FE-ST^{FREE} and the other FE-ST^{FIX} model. Also an additional plot showing instability limit has been made beyond which the wall becomes unstable and collapses. The value for the instability limit of the specimen has been assumed predicting a rigid body assumption given by Eqn. 5.4.

For ST-RM, experimentally observed results were within the range of two extreme FE models as shown in Figs. 5.33 and 5.34 with FE-ST^{FIX} model's response closer to the experimental observations. Here for the comparison purpose, the FE results have been plotted for model with tensile strength of mortar joint interface, $0.5f_t$. Free (FE-ST^{FREE}) and fix (FE-ST^{FIX}) models showed characteristically contrasting behavior. The maximum and residual rotation angle observed for FE-ST^{FIX} model more closely represented the experimental observation with large residual deformation at the end of each excitation run. The fix model showed response which is closer to the realistic situation where the wall lost its stability due to excessive residual rotation. Free model FE-ST^{FREE} allowed the inelastic elongated reinforcing bar to deform freely at the

bottom of the specimen, hence causing stable rocking response of the model with no residual deformation during the loading history. Similar rocking resistance was also observed during the quasi-static cyclic loading as reported in Section 5.4.

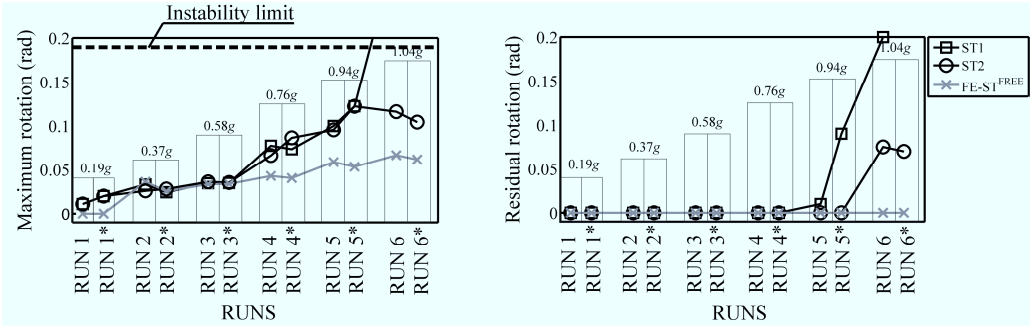

(a) (b)

Figure 5.33: Comparison of experimental and numerical ST-RM^{FREE} results for ST-RM specimens: (a) maximum, (b) residual rotation.

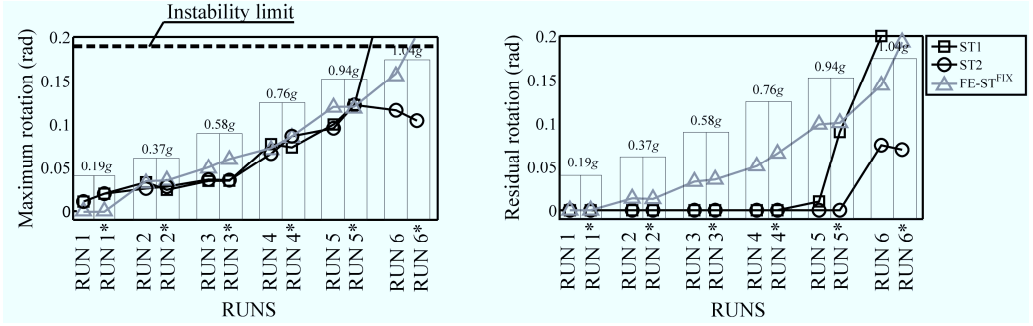

(a) (b)

Figure 5.34: Comparison of experimental and numerical ST-RM^{FIX} results for ST-RM specimens: (a) maximum, (b) residual rotation.

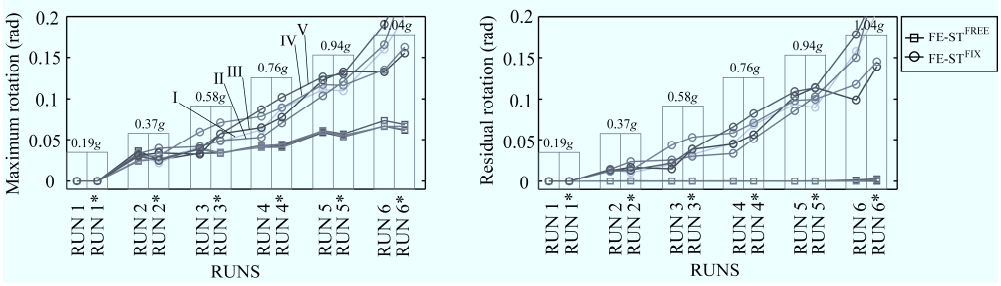

(a) (b)

Figure 5.35: Comparison of sensitivity analysis results for the ST-RM models: (a) maximum, (b) residual rotation.

To check the sensitivity of FE results to mortar mechanical properties, dynamic analysis for FE models with varying tensile strengths of mortar joint was performed as reported in previous section. Fig. 5.35 shows the sensitivity analysis results for FE-ST^{FREE} and FE-ST^{FIX} models. Here, I, II, III, IV and V represent results for FE models with mortar tensile strength values $0.5f_t$, $0.75f_t$, f_t, $1.25f_t$ and $1.5f_t$ respectively. In terms of both maximum and residual rotation angle, FE-ST^{FIX} model showed strong sensitivity in response with change in mortar tensile strength starting from RUN3. FE-ST^{FREE} model however showed very minimal changes in its response to the change in mortar tensile strength property.

SMA-RM specimen

Figs. 5.36 and 5.37 show the results for maximum and residual rotation angle observed at different excitation levels for SMA-RM specimens in comparison with the FE models with tensile strength of mortar joint interface, $0.5f_t$. For each run, the maximum rotation of the wall observed was closely represented by numerical simulation. More importantly, both FE-SMA^{FREE} and FE-SMA^{FIX} models showed characteristically similar response in contrast to what was observed in case of FE-ST models. Variation of support condition at the bottom for the SMA bars did not have any effect on the response of FE-SMA models. Similar observations were made for quasi-static cyclic loading case where both FE-SMA^{FREE} and FE-SMA^{FIX} models showed similar resisting force versus deformation cyclic characteristics.

Fig. 5.38 shows the comparison on sensitivity of FE-SMA models to change in mortar interface tensile strength. The range of variation in tensile strength is similar to the one adopted for FE-ST model. Clear observation can be seen of negligible sensitivity of SMA-RM models' responses to changes in mortar joint strength irrespective of the fixing condition up to RUN5*. However, with the initiation of RUN6, FE-SMA^{FIX} model showed sensitivity to variation in mortar tensile strength. FE-SMA^{FREE} model on the other hand showed no sensitivity through the whole loading

history. SMA bars with their superelasticity did not show residual deformation during the whole loading history which contributed to specimens showing stable rocking response irrespective of the fact that whether it was free or fix model.

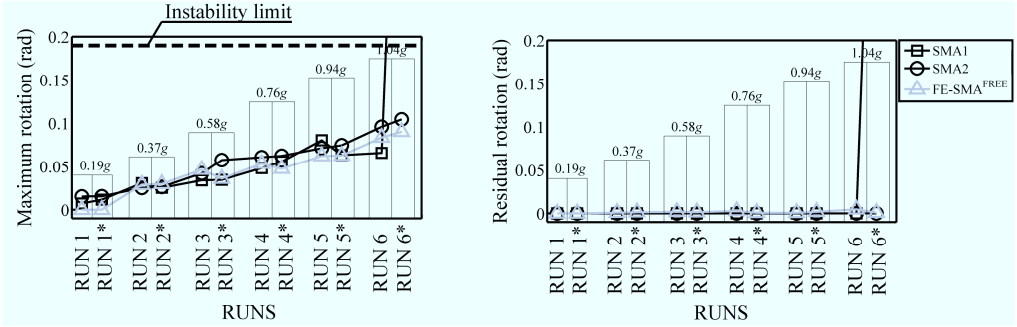

(a) (b)

Figure 5.36: Comparison of experimental and numerical SMA-RM^{FREE} results for SMA-RM specimens: (a) maximum, (b) residual rotation.

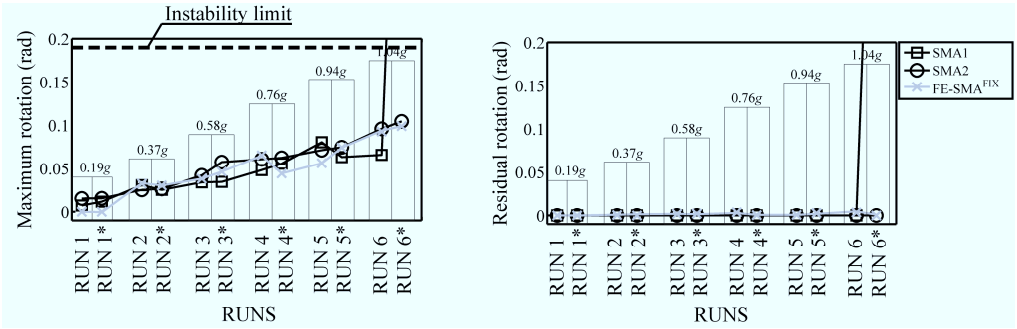

(a) (b)

Figure 5.37: Comparison of experimental and numerical SMA-RM^{FIX} results for SMA-RM specimens: (a) maximum, (b) residual rotation.

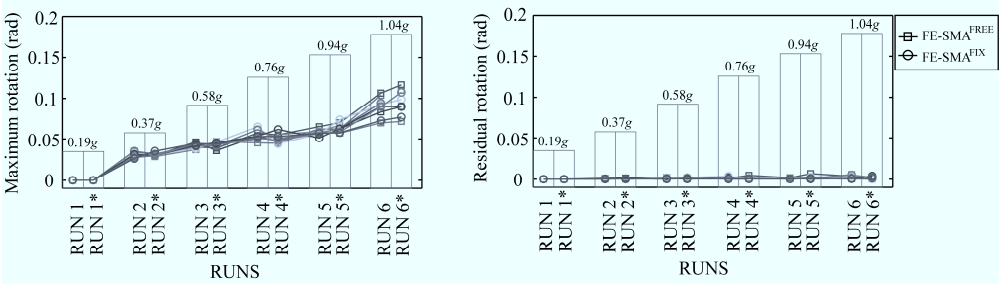

(a) (b)

Figure 5.38: Comparison of sensitivity analysis results for the SMA-RM models: (a) maximum, (b) residual rotation.

5.5.4.3 Deformation time history

Figs. 5.39-5.41 show the deformation time history for U2, ST1 and SMA2 compared with FE models FE-U, FE-ST^{FIX} and FE-SMA^{FIX} with tensile strength of mortar joint interface, 0.5f_t. Here, fix models have been chosen based on the fact that they more closely represented the experimental condition as well as practical setting.

FE-U model showed a sudden increment in rotation angle with the commencement of RUN3 as shown in Fig. 5.39. Geometric nonlinearity incorporated in the FE model assured that there is sudden increment in rotation angle once the instability limit is exceeded.

FE-ST model showed response comparable to experimental observation. Residual deformation at the end of excitation runs similar to experimental observation was predicted which kept on increasing with the increment in the ground excitation as shown in Fig. 5.40. The subsequent P-Delta effects observed experimentally was effectively simulated in the FE models. More importantly the instability of the ST-RM models due to residual strains in steel reinforcement used was successfully simulated.

FE-SMA model showed comparable response with stable rocking representative of SMA2 specimen as shown in Fig. 5.41. No residual deformation was observed even for maximum excitation level up to 1.04g. Absence of any residual strain in SMA reinforcing bar resulted in stable rocking response. Fig. 5.42 shows comparison on deformation time history sensitivity study on FE-SMA^{FIX} model. Sensitivity on the deformation time history was clear with variation in mortar tensile strength properties.

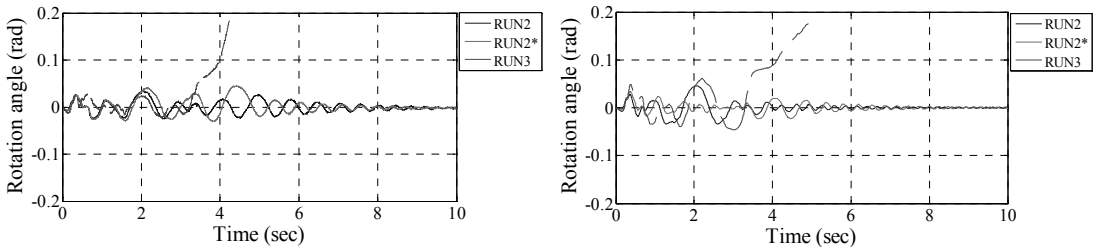

(a) (b)

Figure 5.39: Rotation angle versus time plot for U2 specimen and FE-U model: (a) U2 and (b) FE-U.

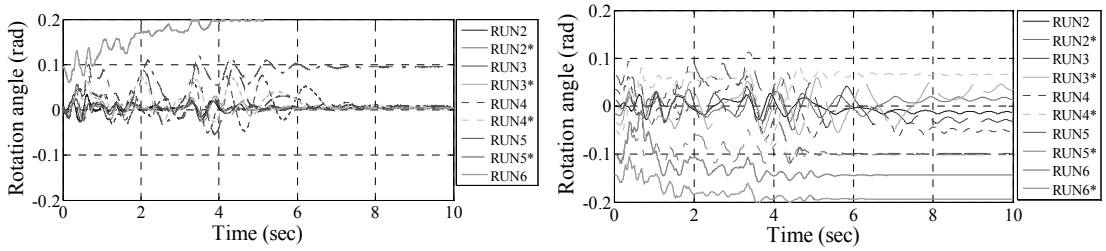

(a) (b)

Figure 5.40: Rotation angle versus time plot for ST1 specimen and FE-ST^{FIX} model: (a) ST1, (b) FE-ST^{FIX}.

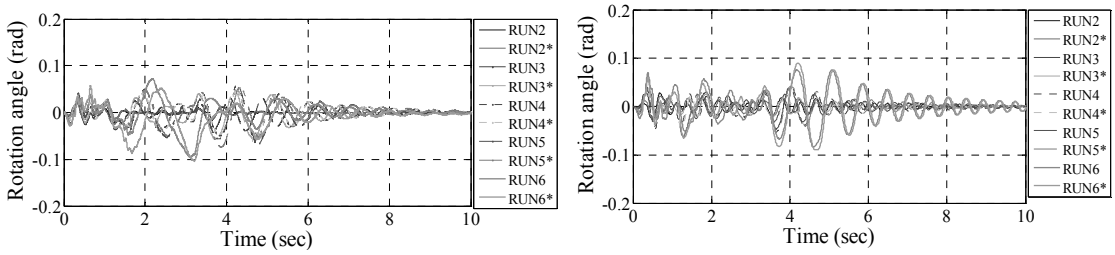

(a) (b)

Figure 5.41: Rotation angle versus time plot for SMA2 specimen and FE-SMA^{FIX} model: (a) SMA2, (b) FE-SMA^{FIX}.

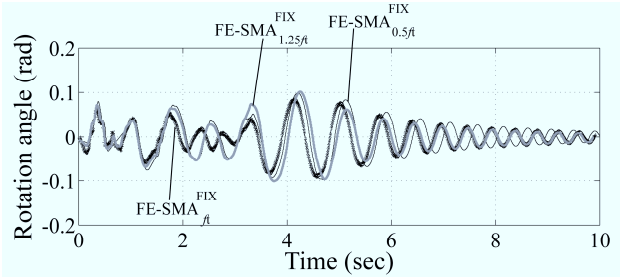

Figure 5.42: Comparison of deformation history plots for sensitivity analysis on FE-SMA^{FIX} models.

5.5.4.4 Discussions

As described in the preceding sections, responses shown by ST-RM and SMA-RM specimens have distinctive features mainly governed by residual strains experienced by steel bars in ST-RM and superelasticity shown by SMA bars in SMA-RM specimens. Nevertheless one of the SMA-RM specimens (SMA1) collapsed at RUN6* with PGA 1.04*g*. As a result, strength of SMA bars over steel bars may be argued. But it should be noted that failure of SMA1 specimen was mainly attributed to the set-up of experimentation consisting of relatively large mass at the top apparently causing strong rocking of top steel plate. Comparison on the vibration response of top steel plate of two SMA specimens, SMA1 and SMA2 are shown in Figs. 5.43 and 5.44. Large amplitude high frequency vibration can be clearly seen in case of SMA1 specimen. This type of rocking is normally not seen in real structures. Hence in authors' view point, failure of SMA1 was primarily due to the test set-up implemented which resulted in an undesirable effect in one of the specimens.

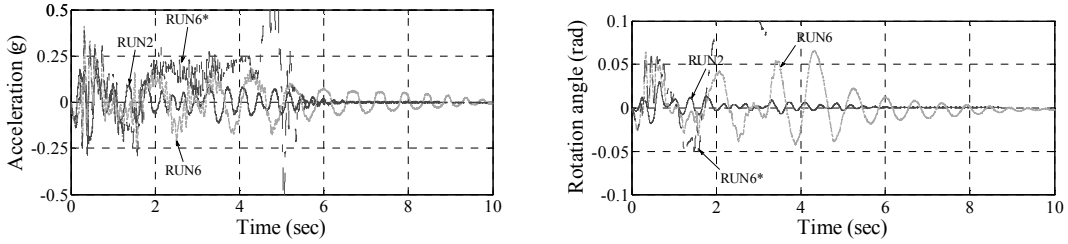

(a) (b)

Figure 5.43: Time-histories for SMA1 specimen for RUN2, RUN6 and RUN6*: (a) Acceleration of top steel plate, (b) Deformation time history.

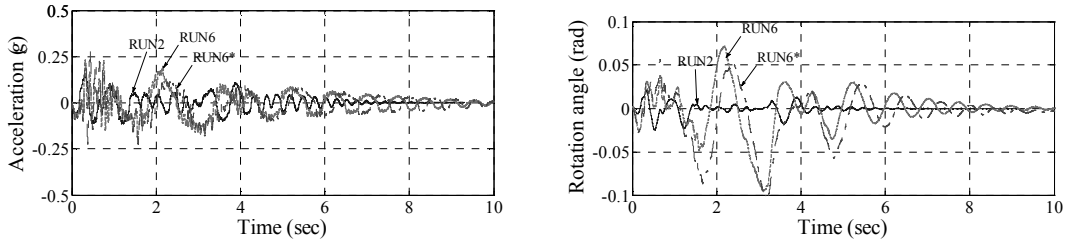

(a) (b)

Figure 5.44: Time-histories for SMA2 specimen for RUN2, RUN6 and RUN6*: (a) Acceleration of top steel plate, (b) Deformation time history

More importantly there was a distinctive characteristic shown by ST-RM and SMA-RM specimen regarding the pinching phenomenon. Fig. 5.45 shows difference in behavior of the two reinforced specimens where rotation history for ST2 and SMA2 specimens have been made for last two excitations RUN6 and 6*. SMA2 specimen showed no sign of pinching whereas for ST2 specimen, the tangent stiffness around the initial position becomes nearly zero showing strong evidence of pinching phenomenon. Additional plots have been made from the results of quasi-static cyclic loading reported in Section 5.4. The hysteresis curve from the static tests for FE-ST^{FIX} showed response very close to the one observed for ST-RM specimen with pronounced stiffness degradation for the post-yield cycles as shown in Fig. 5.45(a). ST-RM^{FREE} on the other hand restored its initial stiffness even for the post-yield cycles since it allows inelastically elongated reinforcing bar to move freely at the bottom of the specimen. On the other hand, in Fig. 5.45(b), SMA2 specimen along with the hysteresis plots for FE-SMA^{FREE} and FE-SMA^{FIX} showed no substantial stiffness degradation irrespective of the type of reinforcement placing. Both experimental and numerical results showed no sign of pinching and stable rocking behavior justifying the effectiveness of SMA bars over steel as reinforcing members. This unstable behavior shown by ST-RM specimens clearly makes SMA-RM specimens more superior in performance.

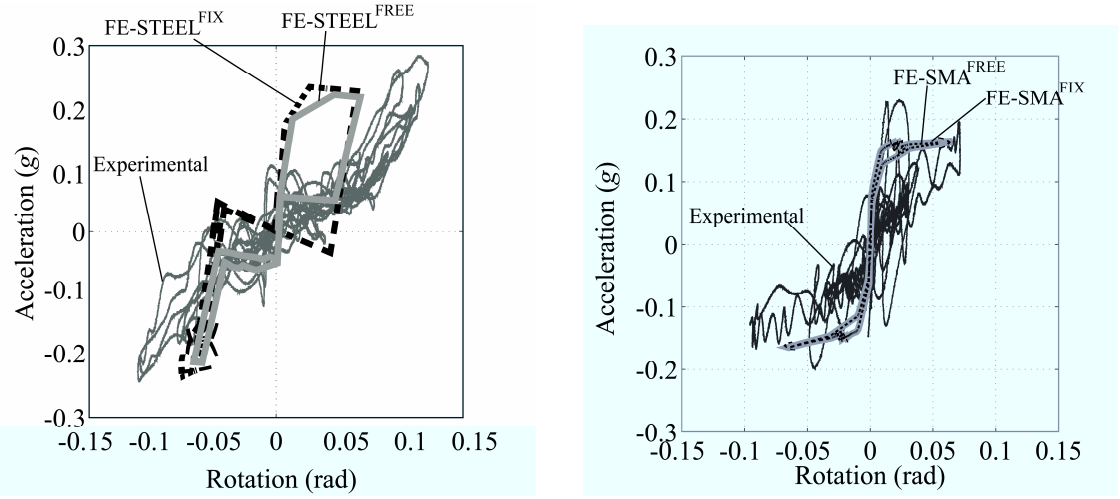

(a) (b)

Figure 5.45: Comparison of acceleration-rotation plots for ST2 and SMA2 specimens with results from quasi static loaded FE models: (a) ST-RM, (b) SMA-RM specimen.

5.6 CONCLUSION

Experimental and finite element study has been performed to investigate the applicability of newly developed Cu-Al-Mn SMA bars to retrofitting of URM walls subjected to out-of-plane quasi-static cyclic loading as well as dynamic base excitations. The tests were conducted on half-scaled single wythe unreinforced and reinforced wall specimens using scaled El-Centro earthquake base excitations of varying magnitude for dynamic loading. FE models were generated with simplified micro modeling strategy, where bricks, mortar joints, and reinforcing bars were represented by continuum elements, interface elements, and truss elements, respectively. Within the scope of the study, the following conclusion can be drawn:

Quasi-static cyclic tests:

(1) Both the ST-RM and SMA-RM specimens showed significant increment both in strength and ductility as compared to the URM specimen. The ST-RM specimen showed pinching phenomenon in the large deformation range while the SMA-RM specimen did not. These results demonstrate the applicability and superiority of the present Cu-Al-Mn SMA bars to retrofitting URM walls as a partial replacement of steel bars.

(2) FE models were developed and calibrated to simulate the experimental results. The developed FE models predicted reasonably well the complete history of all the specimens. Through the FE analysis of the ST-RM specimen, it was shown that the inelastic elongation of the steel bars was the main source of pinching. It was also shown that the superelastic property of the SMA bars was effective to avoid pinching.

(3) It was demonstrated that, if reinforcing bars are fixed at the bottom of the wall

specimen, the ST-RM model showed pinching phenomenon even in the small deformation range while the SMA-RM model did not. This result highlights the superiority of the retrofitting of URM walls by SMA bars in a more practical setting.

Dynamic tests:

(1) URM wall specimens showed brittle collapse, for moderate level excitations which is a typical characteristic of such constructions. For ST-RM specimens, ductility beyond initiation of the first cracking was observed but substantial residual deformation of the wall was also observed at the end of excitation confirming the instability caused by residual elongation of steel bars. This ultimately resulted in premature collapse at the exceedance of instability limit due to P-Delta effect. SMA-RM specimens exhibited stable rocking behavior without significant residual rotations even for base excitation exceeding 1.0*g*. The primary reason for maintaining this stable rocking response was attributed by the superelastic property of the SMA reinforcing bars which ensured that there was no residual strain during and after the loading history. These results demonstrate the applicability and superiority of the present Cu-Al-Mn bars to retrofitting URM walls as a partial replacement of steel bars.

(2) FE models developed effectively represented the dynamic behavior of the masonry specimens. The developed FE models predicted reasonably well the overall mechanism in the deformation time history with sudden brittle failure mechanism in URM, unstable response with large residual deformations in ST-RM and stable rocking response with minimal residual deformations in SMA-RM models.

REFERENCES

[1] ABRAMS D., SMITH T., LYNCH J., and FRANKLIN S. Effectiveness of rehabilitation on seismic behavior of masonry piers. *Journal of Structural*

Engineering, 133 (1): 32-43, 2007.

[2] WILLIS C.R., SERACINO R., and GRIFFITH M.C. Out-of-plane strength of brick masonry retrofitted with horizontal NSM CFRP strips. *Engineering Structures,* 32 (2): 547-555, 2010.

[3] KARANTONI F.V., and FARDIS M.N. Effectiveness of seismic strengthening techniques for masonry buildings. *Journal of Structural Engineering,* 118 (7): 1884-1902, 1992.

[4] EHSANI M.R., SAADATMANESH H., and VELAZQUEZ-DIMAS J.I. Behavior of retrofitted URM walls under simulated earthquake loading. *Journal of Composites for Construction,* 3 (3): 134-142, 1990.

[5] ELGAWADY M.A., LESTUZZI P., and BADOUX M. A review of conventional seismic retrofitting techniques for URM. *Proceeding of the 13th International Brick and Block Masonry conference*, Amsterdam, 2004. http://imacwww.epfl.ch/Publications/StructuralDynamics/ElGawady-Lestuzzi-Badoux-state_art-13IBMaC.pdf [10th April 2011].

[6] PLECNIK J., COUSINS T., and O'CONNER E. Strengthening of unreinforced masonry buildings. *Journal of Structural Engineering,* 112 (5): 1070-1087, 1986.

[7] BUTTON M.R., and MAYES R.L. Out-of-plane seismic response of reinforced masonry walls. *Journal of Structural Engineering,* 118 (9): 2495-2513, 1992.

[8] DRYSDALE R.G., HAMID A.A., and BAKER L.W. *Masonry Structures: Behavior and Design*. Prentice Hall: New Jersey, 1994.

[9] MAZZOLANI F.M., and MANDARA A. Modern trends in the use of special metals for the improvement of historical and monumental structures. *Engineering Structures*, 24 (7): 843-856, 2002.

[10] DESROCHES R., and SMITH B. Shape memory alloys in seismic resistant design and retrofit: A critical review of their potential and limitations. *Journal of Earthquake Engineering,* 8 (3): 415-429, 2004.

[11] SONG G., MA N., and LI H.N. Applications of shape memory alloys in civil structures. *Engineering Structures,* 28 (9): 1266-1274, 2006.

[12] INDIRLI M., CASTELLANO M., CLEMENTE P., and MARTELLI A. Demo-application of shape memory alloy devices: The rehabilitation of the S. Giorgio Church Bell-Tower. *Proceedings of SPIE,* 2001.

[13] PARET T.F., FREEMAN S.A., SEARER G.R., HACHEM M., and GILMARTIN U.M. Using traditional and innovative approaches in the seismic evaluation and strengthening of a historic unreinforced masonry synagogue. *Engineering Structures,* 30 (8): 2114-2126, 2008.

[14] CHRISTIS Z.C., ANDREAS S., THEMOS D., and KARIM H. Application of shape memory alloy prestressing devices on an ancient aqueduct. *Smart Structures and Systems, An Internation Journal,* 4 (2): 261-278, 2008.

[15] MARTELLI A. Recent progress of application of modern anti-seismic systems in Europe – part 2: energy dissipation systems, shape memory alloy devices and shock transmitters. *Proceedings of the 14th World Conference on Earthquake Engineering,* 2008, Beijing. http://www.iitk.ac.in/nicee/wcee/article/14_S05-02-018.PDF [10th April 2011].

[16] EL-BORGI S., NEIFAR M., BEN J.M., CHERIF D., and SMAOUI H. Use of copper shape memory alloys in retrofitting historical monuments. *Smart Structures and Systems, An International Journal,* 4 (2): 247-60, 2008.

[17] SUTOU Y., OMORI T., WANG J.J., KAINUMA R., and ISHIDA K. Effect of grain size and texture on superelasticity of Cu-Al-Mn-based shape memory alloys. *Journal de Physique IV,* 112: 511-514, 2003.

[18] SUTOU Y., OMORI T., YAMAUCHI K., ONO N., KAINUMA R., and ISHIDA K. Effect of grain size and texture on pseudoelasticity in Cu-Al-Mn-based shape memory wire. *Acta Materialia,* 53 (15): 4121-4133, 2005.

[19] ARAKI Y., ENDO T., OMORI T., SUTOU Y., KOETAKA Y., KAINUMA R., and ISHIDA K. Potential of superelastic Cu-Al-Mn alloy bars for seismic applications. *Earthquake Engineering and Structural Dynamics,* 40 (1): 107-115, 2011.

[20] SHRESTHA K.C., ARAKI Y., NAGAE T., OMORI T., SUTOU Y., KAINUMA R., and ISHIDA K. Applicability of Cu-Al-Mn shape memory alloy bars to retrofitting of historical masonry constructions. *Earthquakes and Structures, An International Journal,* 2011, In Press.

[21] Eurocode 8: *Design of structures for earthquake resistance - Part 1: General rules, seismic actions and rules for buildings EN 1998-1:2004*. European Committee for Standardization: Brussels, 2004.

[22] RILEM: *RILEM Technical recommendations for the testing and use of construction materials*. Taylor and Francis: New York, 1994.

[23] *Annual Book of ASTM Standards. Section Four, Construction, Volume 04.05, Chemical-Resistant Nonmetallic Materials; Vitrified Clay Pipe; Concrete Pipe; Fiber-Reinforced Cement Products; Mortars and Grouts; Masonry; Precast Concrete*. ASTM International: West Conshohocken, PA, 2007.

[24] LOURENCO P.B., and ROTS J.G. Multisurface interface model for analysis of masonry structures. *Journal of Engineering Mechanics*, 123 (7): 660-668, 1997.

[25] DIANA: *DIANA User's Manual Release 9.3*. TNO DIANA BV: Delft, 2008.

[26] OLIVEIRA D.V., LOURENCO P.B., and ROCA P. Cyclic behaviour of stone and brick masonry under uniaxial compressive loading. *Materials and Structures* 39(2):247-257, 2006.

[27] GRIFFITH M.C., LAM N.T.K., WILSON J.L., and DOHERTY K. Experimental investigation of unreinforced brick masonry walls in flexure. *Journal of Structural Engineering*, 130(3):423-432, 2004.

[28] TOMAZEVIC M., *Earthquake-resistant design of masonry buildings*, Imperial College Press, London, 1999.

[29] SHRESTHA K.C, NAGAE T., and ARAKI Y. Finite element modeling of out-of-plane response of masonry walls retrofitted by inserting inclined stainless steel bars, *Journal of Disaster Research,* 6 (1): 36-43, 2011.

[30] DAFNIS A., KOLSCH H., and REIMERDES H. Arching in masonry walls subjected to earthquake motions. *Journal of Structural Engineering,* 128 (2):153-9, 2002.

[31] LAM N.T.K, GRIFFITH M., WILSON J., and DOHERTY K. Time-history analysis of URM walls in out-of-plane flexure. *Engineering Structures,* 25 (6):743-754, 2003.

6

SUMMARY AND CONCLUSIONS

With seismic rehabilitation of masonry structures as a main purpose, several goals were set and attainment of those goals meant there were three important aspects of the work involved during this doctoral research work. First goal of the work involved finite element modeling of pinning retrofitted masonry walls [1,2], whose experimental works were previously reported by Takiyama [3], for effective prediction of experimental observations through numerical computations. The finite element tool developed is believed to serve as an important tool for verification as well as check for design specification to the pinning retrofitted walls, whose experimental works cost substantial amount of money and time. Second phase involved an extensive study on the use of polymer cement paste (PCP) [4,5] as bonding agent in pinning retrofitted masonry walls in place of epoxy. Epoxy resin, due to its high cost and low fire resistance, requires replacement and PCP with good workability and low cost is always a better option to move to. The third and the most important part of the research involved application of super elastic materials [6] on masonry retrofitting [7,8]. Some of the important conclusions that can be made from the works have been listed as below divided into corresponding sections based on goal perspective:

Finite element modeling of pinning retrofitted masonry walls

i. Proposal of an equivalent vertical bar model was proposed. The concept of equivalent vertical bar allows simple theoretical prediction of wall strengths and makes a 2D FE modeling possible for the particular retrofitting technique. Additionally, the proposed equivalent vertical bar model provided better convergence under cyclic loading at expense of lesser computational time as compared to inclined bar model.

ii. An evaluation of numerical result sensitivity to modeling parameters using the simplified FE model showed almost no sensitivity to variations in masonry material constants in reinforced specimens, demonstrating the robustness of pinning retrofitting technique under cyclic loading conditions and the stability of the proposed simplified FE modeling.

Applicability of polymer cement pastes (PCPs) as bonding agents for pinning retrofit of masonry

i. Results of workability tests showed PCPs are highly workable even at adverse working conditions, specifically for untreated specimens of SBR1 and SBR2 PCPs workable even at the open time of 10 minutes. The workability test also showed the importance of pre-treatment agents or impregnants, as water penetration barrier system, to increase the workability of PCP, effectively avoiding the loss of water from PCP.
ii. From the pull-out test results, ACL1 and PAE2 have least bond strength as compared to EVA2, SBR1 and SBR2 PCPs. Observed bond strengths of EVA2, SBR1 and SBR2 PCPs were in the range of 5 MPa or more, which represents extremely superior bond strength.
iii. Both compression and shear tests showed notable difference in response between unreinforced and reinforced specimens with the later showing substantial increment in ductility.

iv. One-point bending tests performed also showed significant difference in unreinforced and reinforced specimens. ACL and PAE bonded specimens showed relatively lower resistance due to premature bond slip of the reinforcing bars. SBR PCP bonded specimen showed better resistance. Proposed theoretical and FE prediction also showed response comparable to the experimental observations.

v. The best combination of PCP and pretreatment agent, showing strong bond with minimum strength variation at different open times and also better resistance when tested as masonry assemblage, was attained for SBR PCPs with BPA impregnant as pretreatment agent.

Applicability of Cu-Al-Mn shape memory alloy (SMA) bars to retrofitting of masonry walls

Quasi-static cyclic tests:

i. Both the ST-RM and SMA-RM specimens showed significant increment both in strength and ductility as compared to the URM specimen. The ST-RM specimen showed pinching phenomenon in the large deformation range while the SMA-RM specimen did not. These results demonstrate the applicability and superiority of the present Cu-Al-Mn SMA bars to retrofitting URM walls as a partial replacement of steel bars.

ii. The developed FE models predicted reasonably well the complete history of all the specimens. Through the FE analysis of the ST-RM specimen, it was shown that the inelastic elongation of the steel bars was the main source of pinching. It was also shown that the superelastic property of the SMA bars was effective to avoid pinching.

iii. It was demonstrated that, if reinforcing bars are fixed at the bottom of the wall specimen, the ST-RM model showed pinching phenomenon even in the small deformation range while the SMA-RM model did not. This result highlights the

superiority of the retrofitting of URM walls by SMA bars in a more practical setting.

Dynamic tests:

i. URM wall specimens showed brittle collapse, for moderate level excitations which is a typical characteristic of such constructions.
ii. For ST-RM specimens, ductility beyond initiation of the first cracking was observed but substantial residual deformation of the wall was also observed at the end of excitation confirming the instability caused by residual elongation of steel bars. This ultimately resulted in premature collapse at the exceedance of instability limit due to P-Delta effect.
iii. SMA-RM specimens exhibited stable rocking behavior without significant residual rotations even for base excitation exceeding 1.0*g*. The primary reason for maintaining this stable rocking response was attributed by the superelastic property of the SMA reinforcing bars which ensured that there was no residual strain during and after the loading history. These results demonstrate the applicability and superiority of the present Cu-Al-Mn bars to retrofitting URM walls as a partial replacement of steel bars.
iv. FE models developed effectively represented the dynamic behavior of the masonry specimens. The developed FE models predicted reasonably well the overall mechanism in the deformation time history with sudden brittle failure mechanism in URM, unstable response with large residual deformations in ST-RM and stable rocking response with minimal residual deformations in SMA-RM models.

Future research recommendations:

i. Half scaled masonry walls adopted in the study was governed by the availability of size of SMA bar during the research work. Slight differences in the global response of a half scaled and a real scaled specimen is inevitable. If larger sized SMA bars are available, as an extension to present research, a full scale study of the present retrofitting technique, in a more facilitated shaking

table, would be an interesting future work possibility.

ii. Keeping in mind low cost and high workability of Cu-Al-Mn SMA bars used in this study, future study on application of these highly superior SMA bars in other seismic applications like reinforced concrete structures, steel bracings, etc. can be thought out.

REFERENCES

[1] SHRESTHA K. C., NAGAE T. and ARAKI Y. Finite element modeling of cyclic out-of-plane response of masonry walls retrofitted by inserting inclined stainless steel bars. *Journal of Disaster Research*, 6(1):36-43, 2011.

[2] SHRESTHA K.C., NAGAE T. and ARAKI Y., Finite element study on pinning retrofitting technique of masonry walls with opening subjected to in-plane shear load. *Proceedings of 7th International Conference Analytical Models and New Concepts in Concrete and Masonry Structures*, Krakow, 2011.

[3] TAKIYAMA N. Experimental study on seismic retrofitting of historical masonry structures with emphasis on preservation of original appearance. *PhD Thesis*, Kyoto University, 2009. (In Japanese)

[4] SHRESTHA K. C., PAREEK S., ARAKI Y., Use of polymer-cement pastes as bonding agents for pinning retrofitting of masonry construction, *Proceedings of JCI*, Vol. 33, 2011 (Accepted for publication).

[5] SHRESTHA K. C., PAREEK S., ARAKI Y., Bending tests on pinning-retrofitted masonry beams with use of polymer cement pastes as binding agents, *Proceedings of Architectural Institute of Japan*, 2011 (Submitted for publication).

[6] ARAKI Y., ENDO T., OMORI T., SUTOU Y., KOETAKA Y., KAINUMA R. and ISHIDA K. Potential of superelastic Cu-Al-Mn alloy bars for seismic applications. *Earthquake Engineering and Structural Dynamics*, 40(1): 107-115, 2011.

[7] SHRESTHA K. C., ARAKI Y., NAGAE T., OMORI T., SUTOU Y., KAINUMA R. and ISHIDA K. Applicability of Cu-Al-Mn shape memory alloy rods to retrofitting of historical masonry constructions, *Earthquakes and Structures, An International Journal*, 2011. (In press)

[8] SHRESTHA K. C., IBARADA I., NAGAE T., OMORI T., SUTOU Y. and

ARAKI Y. Shaking table tests on half-scaled masonry walls retrofitted by Cu-Al-Mn SMA rods subjected to out-of-plane flexure, *Proceedings of the 5th World Conference on Structural Control and Monitoring*, Paper No. 243, Tokyo, 2010.